Title
Climate Change at Annual Timescales

Author
Stine, Alexander Robin

Publication Date
2010

Climate Change at Annual Timescales

by

Alexander Robin Stine

A dissertation submitted in partial satisfaction
of the requirements for the degree of

Doctor of Philosophy
in

Earth and Planetary Science

in the

Graduate Division

of the

University of California, Berkeley

Committee in charge:

Professor Inez Y. Fung, Chair
Professor John C. H. Chiang
Professor William D. Collins

Spring 2010

Climate Change at Annual Timescales

Abstract

Climate Change at Annual Timescales

by

Alexander Robin Stine

Doctor of Philosophy in Earth and Planetary Science

University of California, Berkeley

Professor Inez Y. Fung, Chair

The annual cycle is the dominant mode of climate variability for most aspects of climate that humans engage with. Trends in the amplitude and timing of the annual cycle have been observed in both the surface temperature record and the atmospheric carbon dioxide record, but causes and significances of these changes remain poorly understood – in part because we lack an understanding of the character and mechanisms of natural variability.

Here we show that the phase of the annual cycle of surface temperature over extratropical land shifted towards earlier seasons by 1.7 days between 1954-2007, and that this change is highly anomalous with respect to earlier variations, which we take as indicative of the natural range. Significant changes in the amplitude of the annual cycle are also observed between 1954-2007. The observed land phase trends are explained by the cumulative effects of orbital changes, aliasing of the tropical year by sampling of temperature on the Gregorian calendar and changes in atmospheric circulation described by the Northern Annular Mode and the Pacific North America Pattern. These effects also appear to explain the contemporaneous amplitude gain trends, though this is less unambiguous. Ocean trends, in contrast, appear more significant after taking into account natural sources of variability.

The annual cycle of atmospheric carbon dioxide is controlled by variability in the carbon cycling of the terrestrial biosphere. Trends in the annual amplitude, timing of annual carbon draw-down (t_{drop}) and timing of annual carbon rise (t_{rise}) have thus been used to argue for a more photosynthetically active terrestrial biosphere, earlier initiation of biological spring, and increased terrestrial respiration in autumn respectively. We show that changes in amplitude are significant, anomalous when compared against a model of natural variability, spatially coherent over broad latitude bands and related to climate variability. Changes in t_{drop} are neither significant, nor anomalous, and are coherent over only limited spatial scales, indicating t_{drop} is a poor metric for diagnosing large-scale changes in the terrestrial biosphere. The utility of t_{rise} variability for diagnosing changes in the terrestrial biosphere is more ambiguous.

Contents

List of Figures

List of Tables

Acknowledgements

Inez has been a wonderful guide over the last five years. I want to thank Inez, for her generosity with her time and with her intellectual energy, and for the sense of community she creates in her research group. Inez has pushed me to be fearless in exploring new ideas and at the same time rigorous about tearing them down. I could not have asked for a better mentor.

Working in Inez's group is a collaborative enterprise, and I want to thank the members of the Fung Group with whom I have shared so many discussions and meals over the last five years. Thanks to Abby Swann, Charlie Koven, Jung-Eun Lee, Phoebe Lam, Nir Krakauer, Chelsea Chandler, Aparna Bamzai, Junjie Lui, Percy Link, Kate Barton, Wolfgang Buermann, Ben Lintner and Zhonghua Yang. I hope we find many excuses to collaborate in the future. Abby Swann, in particular, has been a real partner in this process of becoming a scientist. Thanks also to John Chiang for his guidance, and to the members of the Chiang group.

I have been lucky with the mentors I have had in life. Mr. Connor, Jan Tullis, Terry Tullis and Karen Fischer each contributed in unique ways to my scientific upbringing.

Peter Huybers has been a dear friend and intellectual companion. It was the pleasure of walking in the mountains and talking about modern and ice-age climate with Pete that kept turning me back to climate science when other forces in my life were pulling me away.

There is a point in one's studies where physics stops being something that happens on the blackboard, and starts being something you see around you, in the sheets of water flowing down the street in a rainstorm. It is a magical time, and I want to thank the classmates who shared that experience with me, and helped bring it alive. Thanks, in particular, to Alison Walker, Baylor Fox-Kemper, Heather Deese, Jake Gebbie, Donnan Steele, Peter Huybers, Kerim Nisancioglu, and Anthony Aguirre.

My brother Nick is seven years younger than me, and it has been a pleasant surprise to see him become a teacher and role model to me. I admire him for the battles he chooses, and in watching him I have learned much about how to be effective.

My Grama Joyce showed me at a young age that the world is full of wonder, which started me on a path that eventually led me to the natural sciences.

My parents have always encouraged and supported me in everything I have done, except for a couple of obviously bad ideas in high school. Their constant support has always been a source of strength in my life.

Chapter 1

Introduction: The Dominance of the Annual Cycle in the Natural World

1.1 The Importance of the Annual Cycle

The annual cycle is the dominant mode of climate variability for most aspects of climate that humans engage with. Much attention has been given to changes in annual mean temperature because it is the simplest metric of global change, but it is difficult to find aspects of the human or the natural world that are, in fact, sensitive to the annual mean temperature. Glacial melt responds to first order to the integral of temperature over those days where temperature is above zero (*Huybers*, 2006). Ocean bottom temperature is controlled by the temperature of the densest water to form at high latitudes in midwinter. The Earth's annual mean energy budget is dominated by summer processes. Biological systems are intricately affected by the details of the timing and magnitude of seasonal transitions in temperature, water and solar energy availability.

The dominance of the annual cycle in surface temperature is obvious in the instrumental record. When we discuss, changes in spatially averaged Northern Hemisphere surface temperature, for example, we often start with a record of annual mean temperatures (shown in Fig. 1.1a). Such a record shows clearly the 20^{th} century warming which has received much attention (*Trenberth et al.*, 2007). However, a comparison of this annual mean warming trend with the same record plotted at monthly resolution (Fig. 1.1b) shows that this warming trend is only a small component of the total variance in the record. In fact the 1/year sinusoidal component explains on average 96% of the variance in monthly mean surface temperatures for extratropical land surfaces, and 90% for extratropical sea surface temperatures

(SSTs). Another indication of the dominance of the annual cycle in climate variability can be seen by comparing the seasonal variation in surface temperature to the glacial/interglacial temperature range (Fig. 1.2). The Last Glacial Maximum (LGM) represented a time when much of North America was under kilometers of ice, a drastically different climate state, and yet over most of the oceans, the temperature difference associated with the transition from summer to winter is larger than this glacial/interglacial transition (*CLIMAP Project Members*, 1984). In fact, these large differences between glacial and interglacial states are apparently themselves due to changes in the seasonality of solar isolation, rather than to changes in the annual mean isolation (*Huybers and Wunsch*, 2005; *Huybers and Tziperman*, 2008).

In Chapters 2 and 3 we consider how the structure of this annual cycle in surface temperature is changing over the period when the annual mean temperature has increased.

The annual cycle (as represented by the 1/year sinusoidal component and its harmonics) also dominates pre-industrial atmospheric CO_2 variability over much of the Earth. However, in contrast to the situation with surface temperature, the anthropogenic trend in atmospheric CO_2 has grown sufficiently large that it dominates the variance in all records we possess (*e.g.* Fig. 1.3). Surface carbon fluxes (from terrestrial, ocean, and anthropogenic processes), which represent mechanistic control, are still dominated by natural processes, and this is likely to continue for the foreseeable future. In Chapter 4 we consider changes in the annual cycle of atmospheric CO_2 over the instrumental record.

This dissertation addresses changes in the annual cycle of both CO_2 and surface temperature, which represent, in their annual mean, the canonical forcing and response of Anthropocene climate change (*Crutzen and Steffen*, 2003). Because the character and the variability of the annual cycle of surface temperature and atmospheric CO_2 are quite different, we take somewhat different approaches in each case.

1.1.1 Conceptual Framework for Seasonal Timing in the Thermometer Record

Discussions of changes in timing of the seasons are sometimes complicated by ambiguity in what we mean by the seasons. Here we illustrate two different definitions of timing of the seasons that have been applied to understanding changes in the thermometer record. The first framework for looking at timing of the seasons is the threshold-based definition. In this framework, a season begins when a fixed threshold temperature is passed. This is a useful framework for thinking about seasons from a biological perspective (*Schwartz et al.*, 2006; *Myneni et al.*, 1997; *Magnuson et al.*, 2000; *Sparks and Menzel*, 2002) since organisms are, in most cases, more sensitive to the absolute temperature than to the temperature relative to the annual mean. The second framework is the one used in Chapters 2 and 3 of this work:

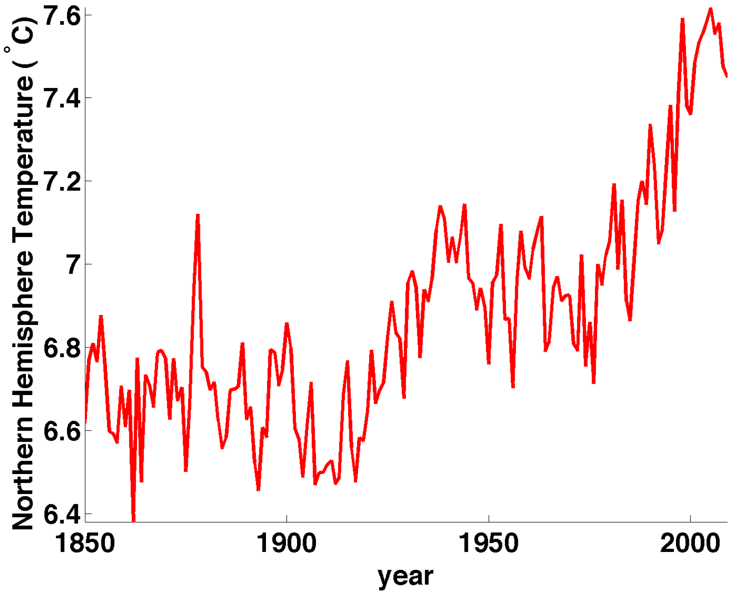

(a) Annual mean Northern Hemisphere temperature

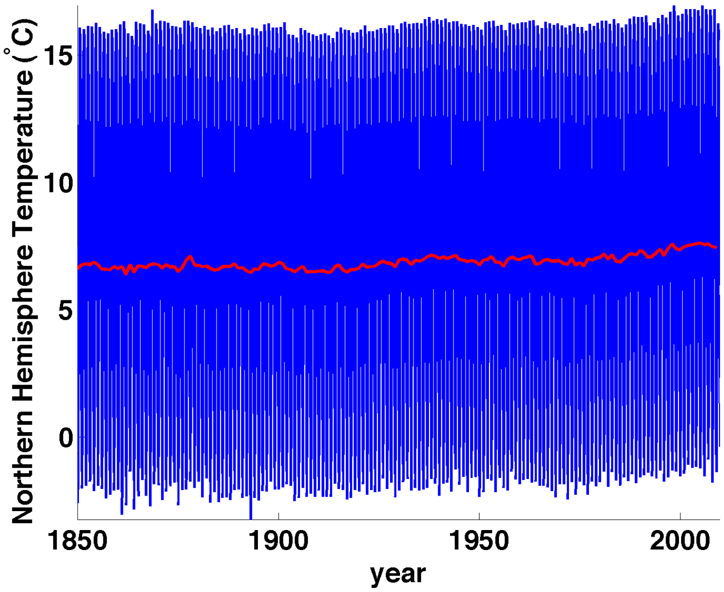

(b) Monthly and annual mean Northern Hemisphere temperature

Figure 1.1. **Northern Hemisphere average temperature:** shown from 1850-2009. **(a)** Northern Hemisphere average temperature plotted as annual averages (red line). Data is from the University of East Anglia's Climate Research Unit (*Jones et al.*, 1999). **(b)** Same, but plotted at both annual (red line) and monthly (blue line) resolution. The annual cycle has been re-introduced into the deseasonalized monthly record of *Jones et al.* (1999), using the climatological annual cycle of *New et al.* (1999).

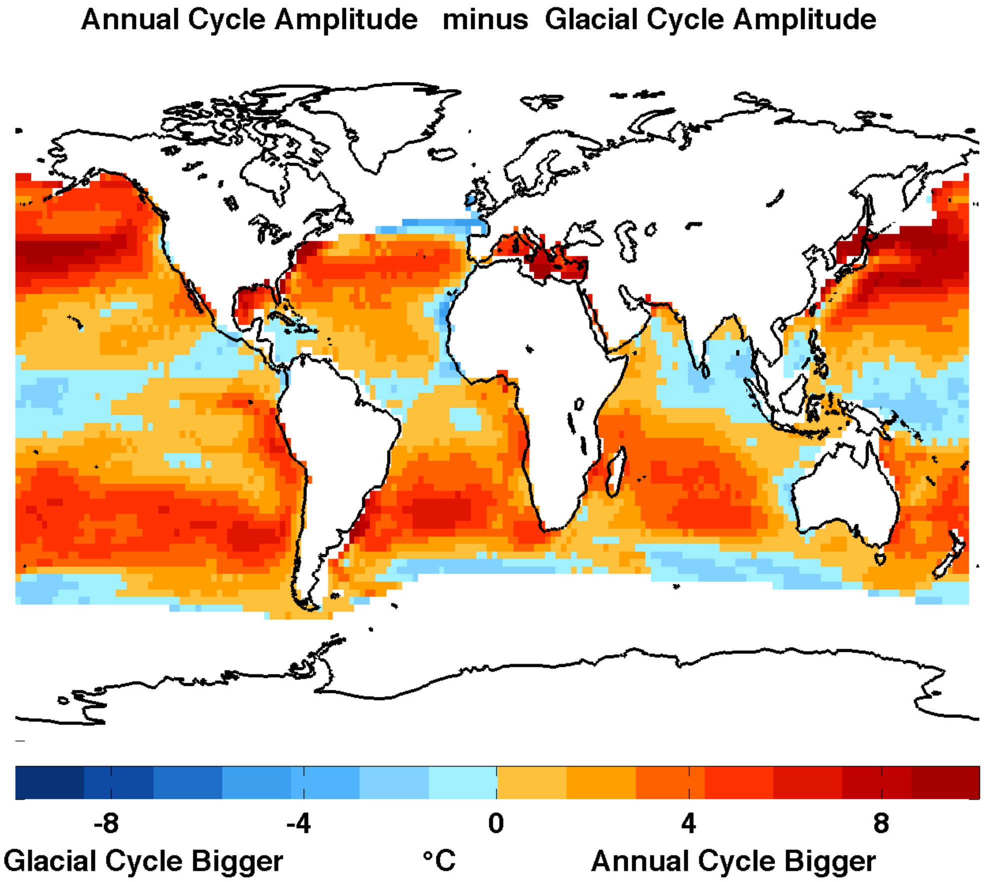

Figure 1.2. **Annual ocean temperature range minus glacial/interglacial temperature range:** Comparison of the magnitude of the annual temperature range to the glacial/interglacial temperature range based on the CLIMAP results (*CLIMAP Project Members*, 1976). Red tones indicate where the annual cycle is larger than the CLIMAP glacial/interglacial temperature range. Blue tones indicate where the glacial/interglacial range is larger than the annual range. The annual temperature range is calculated as the (absolute value of the) difference between August and February sea surface temperature. The glacial/interglacial temperature range is calculated as the difference between the modern annual mean surface temperature and the CLIMAP Last Glacial Maximum annual mean sea surface temperature estimate (*CLIMAP Project Members*, 1981). The CLIMAP project produced surface temperature estimates over the ocean only.

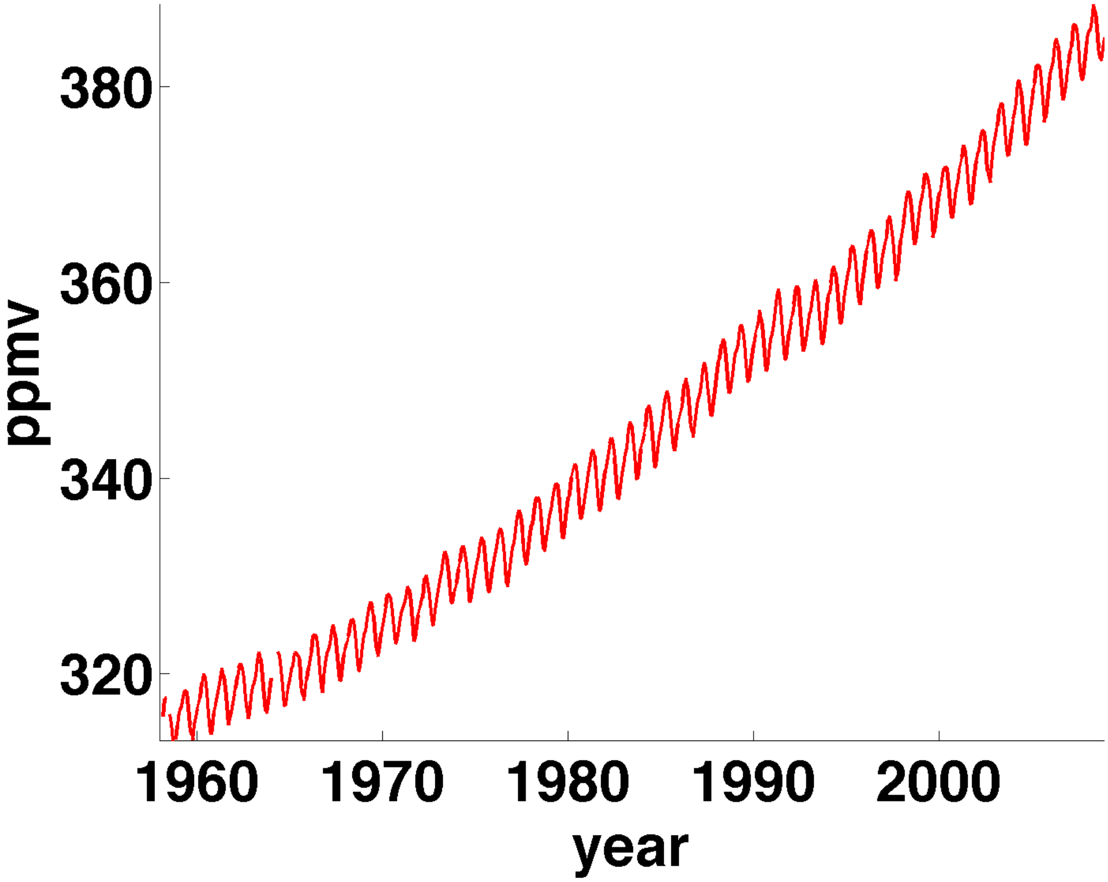

Figure 1.3. **Mauna Loa CO_2:** Monthly atmospheric CO_2 concentration at Mauna Loa Observatory, Hawaii from 1958-2009, from *Keeling et al.* (2001).

the phase of the yearly period sinusoidal (Fourier) component. This is a useful framework for understanding the physical response of a system to forcing.

Suppose the annual cycle in surface temperature at a given location is described by a mean temperature plus a sinusoid $T(t) = \overline{T} + A\cos(2\pi t - \theta)$. Fig. 1.4a shows such an annual cycle where $A = 20$°C, $\theta = 210$ days, and $\overline{T} = 0°C$.

In our threshold-based definition of the annual cycle, we will define the time when the temperature is above zero degrees Celsius as the "warm season", and the time when the temperature is below zero degrees Celsius as the "cold season." We will define "threshold-based-spring" as the day of the year when the the temperature rises above zero, and "threshold-based-fall" as the day of the year when the temperature drops below zero.

In our base-case (Fig. 1.4a, blue line), the warm season starts on 01 April, the cold season starts on 01 October, and the warm and cold seasons are of equal length (182.5 days).

Now consider what happens if the temperature increases, such that every day is warmer by the same amount. Fig. 1.4b shows the case where the phase (θ) and amplitude (A) have not changed, but the mean temperature ($\overline{T}$) has increased by 6°C. In the threshold-based framework, "spring" now comes 18 days earlier and "fall" comes 18 days later and the warm season is now 71 days longer than the cold season. But from a sinusoidal perspective, nothing about the timing has changed. The date of the peak temperature has not changed, the date of the minimum temperature has not changed, and the dates of most rapid transition have not changed. Only the mean has changed.

Next consider the case where there is a shift in the timing of the seasons, but no change in the mean temperature. Fig. 1.4c shows the case where the annual mean temperature ($\overline{T}$) and amplitude (A) have not changed, but the phase has shifted earlier by 20 days. Only in this case will the two frameworks for timing of the seasons give the same result. In both frameworks the timing of spring has shifted earlier by 20 days, and the timing of fall has also shifted earlier by 20 days. In the threshold framework, the lengths of the warm and cold seasons are equal.

Finally, we can consider the case where both the mean and the phase are changing at the same time. Fig. 1.4d shows the case where the annual mean temperature ($\overline{T}$) has increased to 6°C and the phase has shifted earlier by 20 days. In the threshold framework we would say that spring has shifted earlier by 38 days and fall has shifted earlier by 3 days, lengthening the warm season at the expense of the cold season. In the sinusoidal (Fourier) perspective used in Chapters 2 and 3, we would say that the annual cycle has shifted earlier by 20 days, and the mean temperature has increased.

What makes the results presented in Chapter 2 interesting is that there is no *a priori* reason to suppose that a change in the mean temperature would directly force changes in seasonal timing as described by the sinusoidal framework. That is, the case of annual mean warming only (Fig. 1.4b) describes a change in seasonal timing in the threshold framework, but not in the sinusoidal framework.

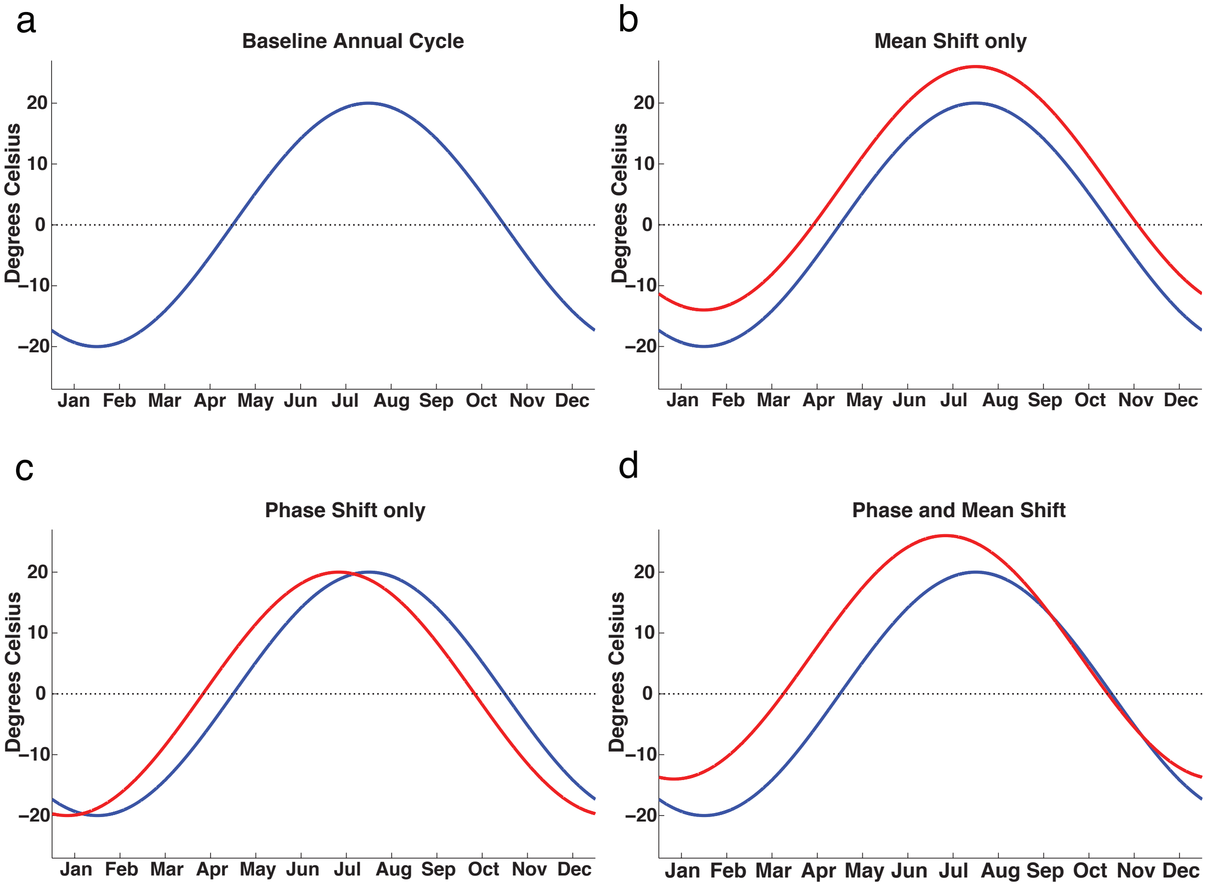

Figure 1.4. **Cartoon of 2 different frameworks for changes in timing of seasons. (a)** Baseline annual cycle (blue in all subpanels). **(b)** Annual mean warming with no phase shift (red line). **(c)** Phase shift with no change in mean (red line). **(d)** Phase shift and change in annual mean temperature (red line).

1.1.2 Conceptual Framework for Seasonal Cycle in the Atmospheric CO_2 Record

The annual cycle in atmospheric CO_2 is produced by a competition between the surface processes that add and remove carbon from the atmosphere. On annual timescales carbon is removed from the atmosphere by photosynthesis on land and by dissolution in the ocean. Carbon is introduced to the atmosphere by respiration of organic matter, by ocean outgassing, and by industrial activities (*Andres et al.*, 1996; *Boden et al.*, 2009).

The dominant source of annual variability is exchange of carbon between the atmosphere and the land surface. Photosynthesis by terrestrial plants removes $\sim 100 \times 10^{15}$ grams of carbon (Pg C) from the atmosphere each year (*Leith*, 1975). These same plants then respire about half of this carbon back to the atmosphere as they access energy to run their internal metabolic processes. The other ~50 Pg C/year of photosynthesized carbon is returned to the atmosphere by decomposers, respiring the carbon from the dead plant tissue they consume. Both photosynthesis and respiration are strongly seasonal. Photosynthesis requires light, and is more efficient in warm, well-watered plants. Respiration requires organic material to break down, and proceeds more rapidly with increasing temperature. Fig. 1.5b illustrates how the competition between terrestrial photosynthesis and respiration produces the annual cycle in atmospheric CO_2. Both photosynthesis (green line) and respiration (red line) are concentrated in the warm months. Photosynthesis wins over respiration in summer, and respiration wins out during the rest of the year. The net land flux (brown line) is thus the residual of much larger gross fluxes.

The ocean also exchanges ~100 Pg C/year with the atmosphere; however, the seasonal variability is small relative to that seen on land (See Fig. 1.5a for comparison of magnitudes in a model). The ocean takes up carbon at high northern latitudes where the surface waters are cold, which drives dissolution. Surface ocean photosynthesis removes carbon from the surface water, and when this carbon is incorporated into particles heavy enough to sink, this carbon is exported to depth. Upwelling water in the tropics is carbon-rich because of the remineralized biogenic carbon it has accumulated while at depth. This, combined with the rapid warming that this water experiences when it is brought from depth to the tropical surface, produces a tropical ocean source of carbon to the atmosphere. For a broad overview of the carbon cycle see *Prentice et al.* (2001) and *Denman et al.* (2007).

1.2 Structure of Dissertation

In Chapter 2, we demonstrate the existence of large-scale shifts in the strength and the timing of the seasonal cycle in surface temperature from 1954-2007. We demonstrate that these changes are large-scale, significant, and anomalous when compared to variability in the earlier instrumental record. We also show that the observed changes in the phase of the

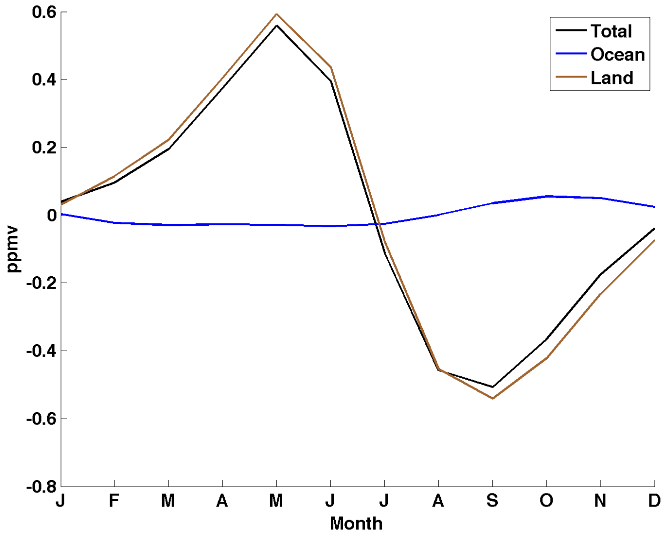

(a) Annual cycles in atmospheric CO_2 due to land and ocean fluxes

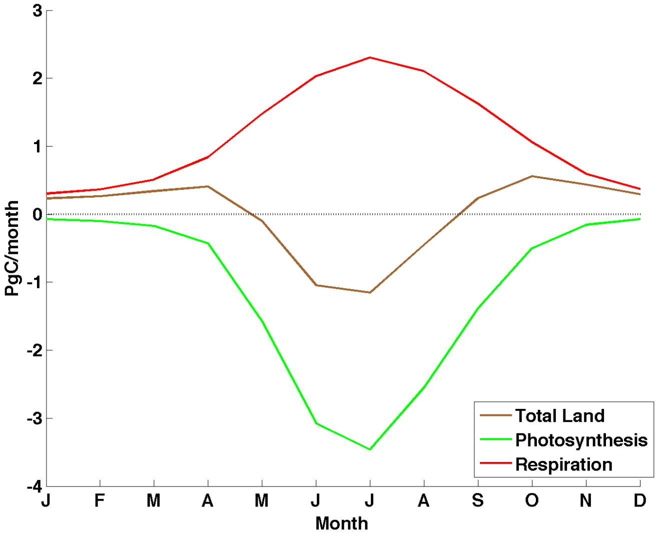

(b) Annual cycle in terrestrial surface carbon fluxes

Figure 1.5. **Carbon cycle annual climatology:** Modelled annual cycles from the general circulation model carbon simulations of *Doney et al.* (2006). **(a)** Annual cycle in atmospheric CO_2 averaged over all latitudes north of 30°N, and pressures from 250 mb to the surface. The total annual cycle (black line) is dominantly controlled by terrestrial processes (brown line). Ocean processes (blue line) produce a weak annual cycle that partially cancels the annual cycle from terrestrial carbon fluxes. **(b)** Annual cycle in terrestrial carbon fluxes (brown line), decomposed into carbon removal from the atmosphere by photosynthesis (green line), and carbon introduction to the atmosphere by respiration (red line).

annual cycle of surface temperature are predicted by none of the model simulations of the Earth's climate response to 20^{th} century forcing undertaken as part of the World Climate Research Program's Coupled Model Intercomparison Project Phase 3 (*Meehl et al.*, 2005, 2007b). We propose a number of mechanisms that might produce the observed trend and estimate how large these effects would need to be to explain the observed trend. This chapter was previously published as:
A. Stine, P. Huybers, and I. Fung. "Changes in the phase of the annual cycle of surface temperature." *Nature*, 457(7228):435-440, 2009.

In Chapter 3, we show that the observed trend in the phase of the annual cycle in surface temperature is affected by (*i*) orbital drift of the phase of the annual cycle in solar insolation relative to the tropical year, (*ii*) aliasing of the tropical year by sampling on the Gregorian calendar, and (*iii*) variability in the circulation of the Earth's atmosphere. We show that the observed trend in phase of the annual cycle in surface temperature can be explained by simultaneously taking into account these three processes. These effects also appear to explain the contemporaneous amplitude gain trends, though the effect here is less unambiguous. Ocean trends, in contrast, appear more significant after taking into account natural sources of variability.

In Chapter 4, we turn to the annual cycle in atmospheric CO_2 and its variability. Using the relatively long atmospheric CO_2 records from Mauna Loa, Hawaii, and Barrow, Alaska, as our focus, we investigate changes in the amplitude of the annual cycle (A), changes in the timing of spring carbon removal from the atmosphere (ϕ_{drop}), and changes in the timing of the return of carbon to the atmosphere in the autumn (ϕ_{rise}). These represent the three metrics for changes in the variability of the annual cycle in atmospheric CO_2 that have been used to argue for changes in the carbon cycling of the terrestrial biosphere (*Keeling et al.*, 1996; *Piao et al.*, 2008). For each metric at each station, we compare the observed trend to "natural variability" as represented by a 1000-year control simulation of a fully coupled carbon-land-ocean-atmosphere general circulation model (*Doney et al.*, 2006). We then use both the numerical model and the wider network of atmospheric CO_2 observations to evaluate the spatial representativeness of the observed trends. We find that the observed amplitude trends are significant, anomalous when compared to the model, and representative of the background air over broad latitudinal swaths. Observed trends in ϕ_{drop}, in contrast, are neither significant, anomalous, nor representative over large distances. The significance and anomalousness of ϕ_{rise} trends are station-dependent.

Chapter 2

Changes in the Phase of the Annual Cycle of Surface Temperature

The annual cycle in surface temperature is massive, comparable in magnitude to that of the glacial-interglacial cycles at most places on Earth. Trends in the phase and the amplitude of the annual cycle in surface temperature have been observed, but the causes and significance of these changes remain poorly understood — in part, because we lack an understanding of the natural variability. Here we show that the phase of the annual cycle of surface temperature over extratropical land shifted towards earlier seasons by 1.7 days between 1954-2007, and that this change is highly anomalous with respect to earlier variations, which we take as indicative of the natural range. Significant changes in the amplitude of the annual cycle are also observed between 1954-2007. These shifts in the annual cycles appear to be related, in part, to variations in the Northern Annular Mode, though the land phase shift is significantly larger than predicted by trends in the Northern Annular Mode alone. Few IPCC models reproduce the observed decrease in amplitude and none reproduce the shift toward earlier seasons.

2.1 Introduction

Climate change is often described by trends in annual mean temperature, but large seasonal temperature changes exist independent of changes in the annual mean. A small literature exists concerning the variability in the phase of the annual cycle. *Thomson* (1995) examined the Central England thermometer time series (CET, 1659-1990) and identified a trend in the phase of the annual cycle toward later seasons beginning around 1950 that is anomalously large in the context of the preceding several hundred year record. He argued that this excursion is associated with increases in atmospheric CO_2 concentration. *Thomson* (1995) also presented evidence of trends in the phase of the annual cycle over larger spatial scales and an increase in the spatial variance of the trends. *Mann and Park* (1996) and *Wallace and Osborn* (2002) demonstrated that the hemispheric averaged observations contain an amplitude and phase trend. The amplitude trend is negative and is related to the observation that winter is, on average, warming more quickly than summer (*Wallace et al.*, 1995; *Balling et al.*, 1998; *Trenberth et al.*, 2007). The hemispheric phase trend, however, is towards earlier seasons, the opposite direction of what *Thomson* finds for Central England.

The importance of these observed amplitude and phase trends is hard to judge because we lack a good model for natural variability. *Wallace and Osborn* (2002) used two criteria to evaluate whether the observed trends are unusual: (*i*) a statistical test for the presence of a trend and (*ii*) a comparison of trends with natural variability as represented in a general circulation model (GCM). Neither of these approaches is altogether satisfactory. We expect low-frequency variability to always be present, so the presence of a trend in and of itself is not surprising (*Wunsch*, 1999). Furthermore, GCMs may not give us an accurate picture of low-frequency variability, particularly in phase, because of two shortcomings. First, the models that have been used to evaluate phase and amplitude variability (*Manabe et al.*, 1991; *Oglesby and Saltzman*, 1992; *Johns et al.*, 1997) have used seasonal heat and freshwater flux adjustments in order to match the mean annual cycle, which may artificially stabilize the modeled annual cycle. Second, and more troubling, Northern Hemispheric phase trends predicted by models forced with 20^{th} century anthropogenic forcing are in the *opposite* direction than the observed trend (*Mann and Park*, 1996; *Wallace and Osborn*, 2002). Modeled Northern Hemisphere amplitude trends also disagree with observations when compared using a temporally fixed network (*Wallace and Osborn*, 2002). Models that are unable to replicate observed trends are clearly not ideal for constraining the range of natural variability. Instead, we appeal to the early observational record to estimate the natural spatial and temporal variability in the seasonal cycle and ask if the trends observed in the recent record are anomalous in nature.

2.2 The Basic State of the Annual Cycle

Two distinct temperature-based methods for discussing the timing of the seasons have been used in the literature. Most common is a threshold-based model wherein seasonal transitions are defined as the time of year when the temperature rises above or drops below some specific value. In this framework, the ‘spring’ threshold will be reached earlier if temperature increases uniformly through the year. This type of change is of first order importance for explaining changes in seasonality observed both in biological systems (e.g. flowering dates (*Schwartz et al.*, 2006; *Sparks and Menzel*, 2002), bird migration timing (*Schwartz et al.*, 2006; *Sparks and Menzel*, 2002), and terrestrial surface carbon uptake (*Myneni et al.*, 1997)) and in components of climate that exhibit threshold responses (e.g. the freezing and melting of ice (*Magnuson et al.*, 2000)). However, threshold-based definitions conflate changes in the phase of the annual cycle with changes in the annual mean (see discussion in Supplementary Information). We instead describe the seasonal cycle by the amplitude and phase of the 1/yr sinusoidal component in surface temperature, a measure of seasonality distinct from changes in the annual mean (*White and Wallace*, 1978; *Thompson*, 1994; *Hsu and Wallace*, 1976; *van Loon*, 1972; *Eliseev et al.*, 2006), and reference it to the 1/yr sinusoidal component in local solar insolation. The difference between the temperature and local insolation phases ($\lambda = \phi_T - \phi_{sun}$) is the *lag* (*Prescott and Collins*, 1951), and the ratio between the amplitudes ($\mathsf{G} = \frac{A_T}{A_{sun}}$) is the *gain* (see Methods Summary). We examine gridded 5°×5° temperature records from the University of East Anglia's Climate Research Unit (*Brohan et al.*, 2006; *Jones et al.*, 1999) and analyze long-term mean, detrended variability, and trend fields for land (λ_{land}, G_{land}) and ocean (λ_{ocean}, $\mathsf{G}_{\text{ocean}}$).

The spatial patterns of λ and G (Fig. 1a,b) are dominated by the contrast between land and ocean. The larger ocean thermal mass causes it to respond more sluggishly to oscillatory forcing than land, which yields a smaller and later oceanic response. Ocean points have a mean G of 28 $^\circ\text{C}/\frac{\text{kW}}{\text{m}^2}$ ($\sigma = 15\ ^\circ\text{C}/\frac{\text{kW}}{\text{m}^2}$) and a mean λ of 56 days ($\sigma = 11$ days) compared to the more rapidly adjusting land, which has a mean G of 74 $^\circ\text{C}/\frac{\text{kW}}{\text{m}^2}$ ($\sigma = 23\ ^\circ\text{C}/\frac{\text{kW}}{\text{m}^2}$) and a mean λ of 29 days ($\sigma = 6$ days).

Superimposed on the dominant land-ocean contrast is an east-west gradient in G and λ. As we move from west to east (following the prevailing winds) across the midlatitude continents, there is a tendency towards a more rapid response (large G_{land}, small λ_{land}). This cross-continent gradient in G_{land} is quite strong, while the gradient in λ_{land} is relatively weak (λ_{land} adjusts rapidly to interior values along the western continental margin (*Thomson*, 1995; *Mann and Park*, 1996)). Conversely, as we move from west to east across the midlatitude ocean basins, there is a tendency towards a more sluggish (small $\mathsf{G}_{\text{ocean}}$, large λ_{ocean}) response, and the relative strengths of the $\mathsf{G}_{\text{ocean}}$ and λ_{ocean} gradients is reversed from that of the land ($\mathsf{G}_{\text{ocean}}$ adjusts rapidly to interior values along the western margin of ocean basins).

The role of land-sea contrast in setting the climatological distribution of the annual cycle is not a new observation (*Prescott and Collins*, 1951; *Ward*, 1906; *Kendrew*, 1961; *Jain et al.*, 1999), but its dominance is particularly obvious when considering the relationship between G and λ. Pairs of G and λ fall along an arc (Fig. 2a). We define a 'seasonal response index' to represent a point's position in this lag/gain space as $\text{SRI} = \frac{\mathsf{G}-\min(\mathsf{G})}{\max(\mathsf{G})-\min(\mathsf{G})} - \frac{\lambda-\min(\lambda)}{\max(\lambda)-\min(\lambda)}$ and find that 75% of the variance in SRI is explained by the distance that one must travel to the west from a grid point before reaching the coast, where distance is taken as positive for land and negative for ocean (see Supplementary Information for more discussion on the structure of variability). The relationship between SRI and distance from the coast holds best in Eurasia, where southern mountains constrain the transport to be zonal and isolate the interior from tropical moisture. Deviations from this general east-west pattern are found in regions where transport is less zonal, such as the southeastern North American Monsoonal

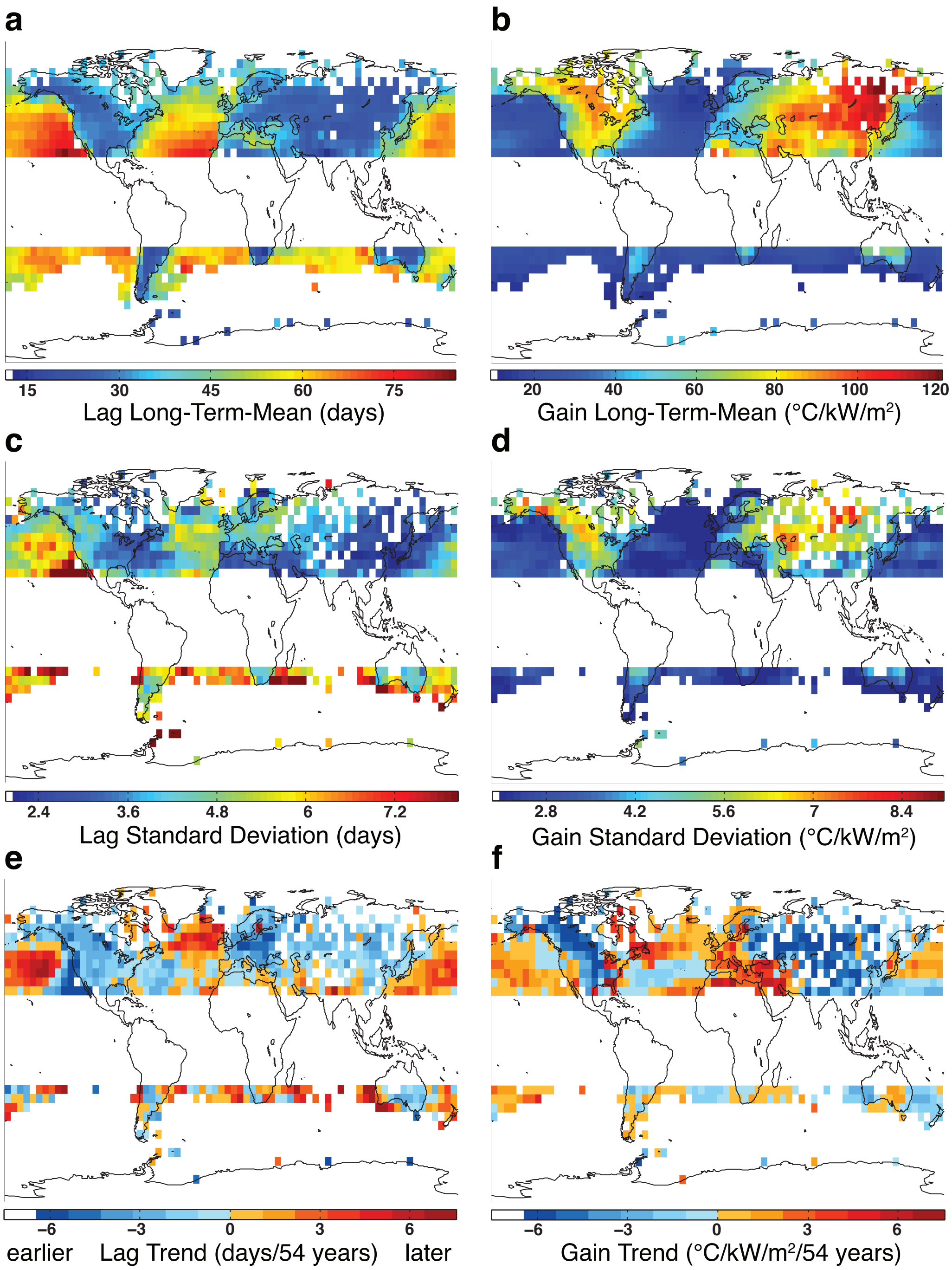

Figure 2.1. **Lag and gain fields:** Left column panels are Phase Lag (λ); Right column panels are Amplitude Gain (G); Top Row gives long-term-mean values; Middle Row gives temporal standard deviation of the detrended time series of λ and G; Bottom Row gives trends in days/(54 years) and $°C/\frac{kW}{m^2}/(54 \text{ years})$. Both variability and trend maps are plotted on the 'dense network' (1954-2007), without land and ocean masks applied. Results have been excluded in the tropics, where data availability is poor, and where less than 85% of the varience in an average year is explained by the 1/yr component.

region, where there is strong poleward moisture transport onto land, and in the western United States, where the north-south alignment of the Rocky Mountains effectively blocks oceanic influence from the Pacific.

The observed arc in the relationship between G and λ is a ubiquitous feature of seasonally driven models that contain interacting land and ocean regions, and can be understood as the natural consequence of interacting sinusoids. Consider two sine waves with different phases and amplitudes, $S_1 = A \sin(\phi)$ and $S_2 = \frac{A}{r} \sin(\phi + \Delta\phi)$. Weighted averages of the two sine waves, $wS_1 + (1-w)S_2$, yield sine waves with amplitude $A_w = \frac{A}{r}\sqrt{w^2r^2 + 2rw(1-w)\cos\Delta\phi + (1-w)^2}$ and phase $\phi_w = \phi + \cos^{-1}\left(\frac{A}{A_w}\left(w - \frac{1}{r}(1-w)\cos\Delta\phi\right)\right)$, where $0<w<1$. A mixing line using this equation (Fig. 2a) is consistent with the general form of the observed arc. Apparently, the spatial structure associated with the seasonal cycle can be understood, to first-order, as the result of variable mixing between continental and marine influence.

Variability in G (Fig. 1d) tends to be largest where the climatological G is large (R=0.83), and is about twice as large on land ($\overline{\sigma} = 5.2$ °C/$\frac{\text{kW}}{\text{m}^2}$) as over the ocean ($\overline{\sigma} = 2.5$ °C/$\frac{\text{kW}}{\text{m}^2}$). Conversely, temporal variability in λ (Fig. 1c) is correlated with G^{-1} (R=0.62) and is larger over the ocean ($\overline{\sigma} = 5.0$ days) than over land ($\overline{\sigma} = 4.0$ days). The inverse relationship and larger λ_{ocean} variability arises because finite perturbations more readily alter the phase of a smaller amplitude sinusoid (see Supplementary Information discussion on natural variability). We thus expect that it will be more difficult to detect the presence of any true phase trend over the ocean.

2.3 Trends in the Phase and Gain of the Annual Cycle

The 1954-2007 λ_{land} trends (Fig. 1e) are predominantly towards earlier seasons, with a mean decrease of 1.7 days (i.e. 6%) over the last 54 years. The λ_{ocean} trends are large but regionally disparate. For example, the interior of the North Pacific, and the Atlantic north of 50°N exhibit trends towards *later* seasons, while along the eastern edge of the North Pacific, and in the North Atlantic south of 50°N, trends are primarily towards *earlier* seasons. The mean λ_{ocean} shift is towards later seasons by 1.0 days over the last 54 years.

A comparison of trend and variability maps (Figs. 1c,d vs e,f) reveals that the trends are large where the detrended variability is large. This suggests the obvious null hypothesis that the trends are merely a manifestation of natural variability. One test for whether the trends observed in the recent record are consistent with natural variability is to compare them to trends observed in earlier periods. We consider the distribution of pointwise trends (Fig. 2b) for the 1900-1953 and 1954-2007 intervals using those records which have good temporal coverage during both intervals (see Methods — this is the default distribution of records which we use below unless specifically stated otherwise). Land and ocean are considered separately because the character of their annual cycles are so different.

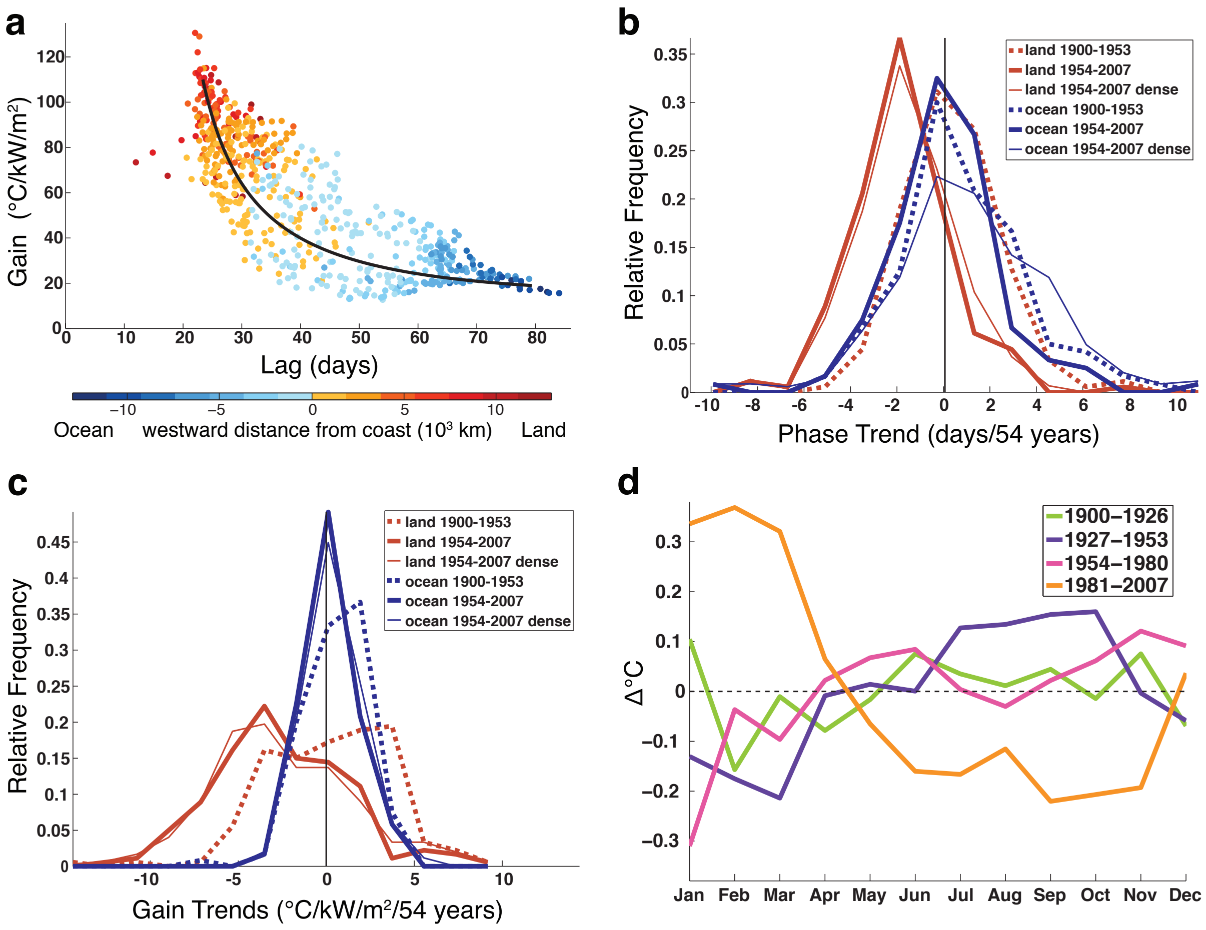

Figure 2.2. **Distribution and character of trends in annual cycle.** **(a)** Observed relationships between local gain (G) and lag (λ) for Northern Hemisphere Extratropical locations. Color represents distance one must travel to the west from the grid point to reach the coast (positive for land, negative for ocean). Outliers with $\lambda<20$ days are from the Indian Subcontinent and presumably reflect monsoon dynamics. The black line shows the non-linear relationship between amplitude and phase for weighted averages of two endmember sine waves (see Supplementary Information). **(b)** Normalized histograms of pointwise λ trends (in days/(54 years)). Red lines represent land. Blue lines represent ocean. The thick dotted lines give the distributions for the control period (1900-1953) on the 'comparison network'. The thick solid line gives the distribution for the same spatial network for 1954-2007. The thin solid line is for the 'dense network' (1954-2007) (see Methods for network description). **(c)** same as (b), but for G trends (in $°\mathrm{C}/\frac{\mathrm{kW}}{\mathrm{m}^2}/(54\ \mathrm{years})$). **(d)** Anomalies in composite land annual cycle shape for 27-year periods, relative to 108-year composite. Southern Hemisphere grid boxes have been shifted by 6-months before averaging.

We adopt a null hypothesis that the mean of each distribution of trends is zero. Testing this null hypothesis requires a knowledge of the effective spatial degrees of freedom (*Jones et al.*, 1997; *Madden et al.*, 1993), and we use estimates obtained from the moment-matching method of *Bretherton et al.* (1999) (see Methods). Of the four distributions of λ trends which we consider, only those over land during the 1954-2007 interval have a mean which differs significantly from zero (Table 1), and here the significance is marked (-1.9 ± 1.0 days/(54 years), p<0.001). Repeating the tests for the latter interval using the larger spatial network available for 1954-2007 (the 'dense network', see Methods), supports the significance of the λ_{land} trend (-1.7 ± 0.8 days/(54 years), p<0.001). We also detect a significant 1954-2007 λ_{ocean} trend towards later seasons (1.0 ± 0.9 days/(54 years), p=0.02) which is only detectable in the more extensive 'dense network'.

The dominant signal in the 1954-2007 G trend (Fig. 1f) is a decrease in the amplitude of the annual cycle over land, averaging -2.5 $°\text{C}/\frac{\text{kW}}{\text{m}^2}$ over the last 54 years on the 'dense network', a 3% drop. This is the well-known amplification of winter warming (*Parker et al.*, 1994; *Balling et al.*, 1998; *Wallace et al.*, 1995), which is strongest in the interior of Eurasia and in the boreal forests of Western Canada. Note, however, that large regions exist where the amplitude has increased. In Western Europe and the Middle East, the observed increase in G is associated with greater warming in summer than in winter. In the central North Pacific and the southeastern United States, increased G results from winter cooling. In Quebec, the summer warming and winter cooling trends are of comparable magnitudes, leaving little trend in mean temperature but a measurable increase in G. Ocean G trends are almost everywhere small and show a mean increase of 0.4 $°\text{C}/\frac{\text{kW}}{\text{m}^2}$ over the last 54 years.

We apply tests to the G trends similar to those made on the λ trends (Fig. 2c). Of the four distributions of G trends, only those over land during the latter interval have a mean which differs significantly from zero ($-2.6 \pm 2.4° C/\frac{\text{kW}}{\text{m}^2}/$(54 years), p<0.03) (Table 1). If the 'dense network' is used instead for the later period, the G_{land} trends remain significant (p=0.05), and the $\mathsf{G}_{\text{ocean}}$ trends emerge as marginally significant (p=0.07). It is noteworthy that the well-reported changes in the amplitude of the seasonal cycle (*Jones et al.*, 1999; *Wallace et al.*, 1996) are less significant than the less-reported land phase trend. This can be understood as related to natural variability in wintertime temperature. Winter warming is considerably stronger than summer warming over land in the recent period, but the variance of winter land temperatures is also about four times that in summer, making the winter trend less significant and making detection of changes in amplitude difficult (*Wigley and Jones*, 1981). In fact, we are unable to detect a significant difference between summer and winter warming when temperature trends are analyzed as the difference between 3-month seasonal averages (Table 1).

We focus on the λ_{land} trends because their significance is markedly higher than any other observed trend. Furthermore, G trends are more easily discussed in the seasonal average temperature framework than λ and have received more attention elsewhere (*Trenberth et al.*, 2007; *Wallace et al.*, 1996; *Balling et al.*, 1998).

There are two parts to establishing the presence of an anomalous trend. First is the establishment of a trend which is statistically distinguishable from zero, which we demonstrated for the 1954-2007 λ_{land} observations. Second, is establishing that this trend is different in character from what we would expect in the naturally varying system, which is more difficult given the finite length of the instrumental temperature records. We are particularly concerned about low-frequency variability being misinterpreted as an anomalous trend (*Wunsch*, 1999). The absence of a significant λ_{land} trend for the 1900-1953 test period indicates the later trend is anomalous. By restricting ourselves to a smaller set of locations, we can also extend our analysis back to 1850. We construct an average λ_{land} time series by averaging the phase time series from all of the land grid boxes with perfect temporal coverage from 1850-2007 and adopt a null hypothesis that the late period trends result from natural low-frequency variability as represented in the 1850-1953 record. We build a distribution for this null hypothesis by calculating the trend of many synthetic time series having the spectral amplitude structure of the 1850-1953 record, but with randomized phases (*Schreiber and Schmitz*, 2000) (see Supplementary Methods), and are able to reject it with very high confidence (p=0.006). The phase trend over the last 54 years is not consistent with the structure of natural variability found in the earlier record. Furthermore, there is no 54-year period in the 1850-1953 control period which would allow rejection of this null hypothesis. (Note that we are unable to meaningfully compare the trends in λ_{ocean} to the 1850-1953 period because instrumental coverage over the ocean during these early times is poor.)

Finally, it is reasonable to ask if the observed variability is really best thought of as a shift in the 1/yr sinusoidal component, or if it would be better described by changes in individual months. A change in a single month's temperature will map into a shift in the annual cycle, though the 1/yr frequency component is a poor description of such an anomaly. We calculate the mean annual cycles for four 27-year periods, using land grid boxes with good temporal coverage between 1900-2007 (see Supplementary Methods), and consider their anomalies from the 108-yr mean annual cycle (Fig. 2d). (Consideration of the means in these four periods gives insight into the origins of the trends in the 1900-1953 and 1954-2007 intervals.) The most recent anomaly time series (1981-2007) exhibits the largest departures from the long-term mean, and 80% of its variance is at the 1/yr component. The more recent period has more variability at the annual period than the total variability during all preceding periods, highlighting both that these shifts are well described by a 1/yr sinusoidal component and the anomalous nature of the recent changes (see Table S2).

2.4 Origins of the Changes in the Annual Cycle

To explore the origins of the shifts in $\mathsf{G}_{\mathrm{land}}$ and λ_{land}, we first turn to the global climate model results summarized in the 4^{th} Assessment Report (AR4) of the Intergovernmental Panel on Climate Change (IPCC) (*Meehl et al.*, 2007a). In particular, we analyze the 72 simulations of twentieth century climate using observed forcings conducted for the World Climate Research Program's (WCRP) Coupled Model Intercomparision Project phase 3 (CMIP3) (*Meehl et al.*, 2007b). The distribution of mean trends in $\mathsf{G}_{\mathrm{land}}$ and λ_{land} found in the models easily encompass the observed trends during the 1900-1953 interval. But

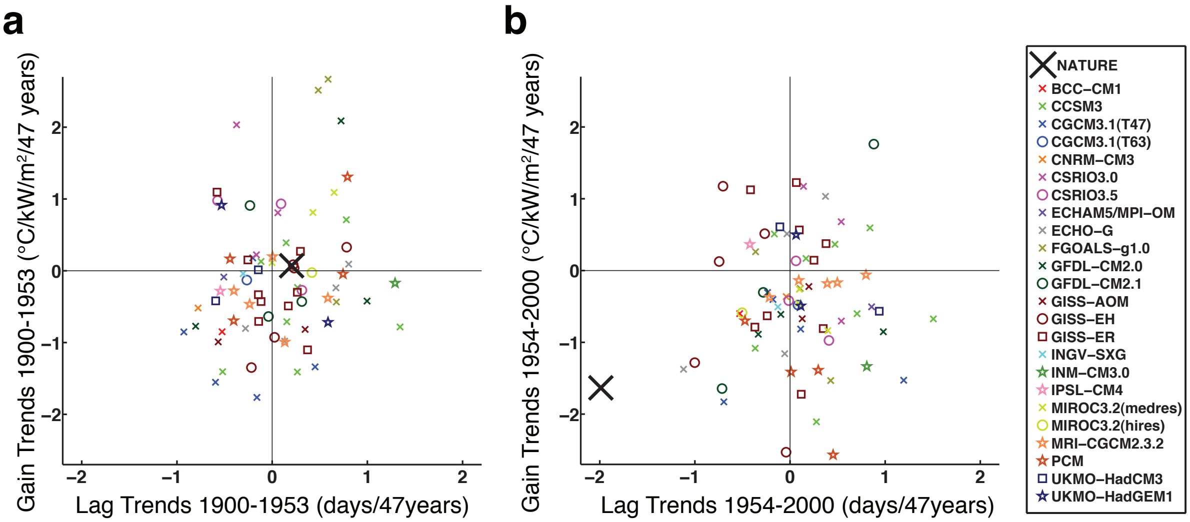

Figure 2.3. **Modelled and observed mean land trends:** **(a)** Observed 1900-1953 land lag (λ_{land}) and gain (G_{land}) trends and those from WCRP "Climate of the Twentieth Century" simulations, sampled at the same locations. Marks with same color and shape indicate multiple runs with the same model. The black X indicates the actual observed trends. **(b)** Same but for 1954-2000. The comparison ends at 2000 because IPCC runs generally stop at end of century. Individual model descriptions are given in *Randall et al.* (2007) and citations therein.

during the 1954-2000 interval (the simulations stop at the end of the century), the observed decrease in G_{land} has a larger magnitude than all but six of the model simulations, and no model reproduces the observed shift toward earlier seasons (Fig. 3). The mean of the model λ_{land} trends for 1954-2000 is towards later, not earlier seasons. Furthermore, 25 atmospheric model runs forced with observed sea surface temperatures for the 1978-2000 period (the Atmospheric Model Intercomparison Project or AMIP2 models (*Gates*, 1992)) do no better at replicating the observed λ_{land} trends (see Supplementary Methods and discussion).

The IPCC model results do not appear to give us an explanation of the observed trends, except to suggest that the answer involves something that the models do not capture. We thus retreat to a simple, conceptual model to explore how local processes may cause variability in λ and G consistent with the observations. Our goal here is to explore some obvious candidates and roughly estimate the size of the perturbation needed to explain the observation. We use a 1-box energy balance model based on *Goody* (1995, chap. 5), forced with sinusoidally varying shortwave radiation, with atmospheric shortwave optical properties calculated following *Shell and Somerville* (2005) (see Methods).

Many of the mechanisms invoked to explain variability in annual mean temperature are unlikely to be directly responsible for the observed shift in phase. Doubling the atmospheric longwave optical depth to simulate the radiative effect of a very large increase in greenhouse gases has essentially no effect on seasonal timing ($\Delta\lambda = 0.1$ days, $\Delta\mathsf{G} = -0.6\ ^\circ\text{C}/\frac{\text{kW}}{\text{m}^2}$).

Increasing solar luminosity by a fixed percent increases the amplitude of the temperature response by the same percent and has a negligible effect on phase (*Thomson*, 1995; *Karl et al.*, 1996). Decreases in sea ice (not represented in our model) present the atmosphere with a larger thermal mass, implying a delayed seasonal response (though threshold responses at the time of spring melt may work in the opposite direction). Consistent with this intuition, the (incorrect) phase delays found in the model results of *Mann and Park* (1996) were attributed to decreases in sea-ice cover.

But there exist numerous mechanisms which may move the seasonal cycle in the observed direction. A decrease of thermal mass on land of 8±4% is sufficient to produce the observed 1.7±0.8 day offset in phase. Thermal mass on land is largely modulated by soil moisture. Compare, for example, the effective thermal mass of a dry desert sand (1.9 $J/m^3/K$) with that of a saturated loam soil (3.2 $J/m^3/K$). For a typical soil, the observed phase shift would require a 13±7% decrease in soil moisture. IPCC AR4 model runs disagree with each other on the sign of recent soil moisture trends and show little skill at explaining the (sparse) observations (*Li et al.*, 2007). The few available long-term measurements suggest increased soil moisture over the latter part of the twentieth century (*Robock et al.*, 2000; *Vinnikov and Yeserkepova*, 1991), which is inconsistent with the thermal mass hypothesis, though we observe that drought reconstructions (*Dai et al.*, 2004) indicate these observations may not be representative of continental-scale variations. The paucity of records with more than 40 years of data prohibit a more detailed comparison. We consider large-scale decreases in soil moisture to be a viable candidate for having caused the observed shift toward earlier seasons.

Perturbations to atmospheric shortwave optical properties are also effective at modifying the annual cycle, and it appears that shortwave absorptivity has been changing, perhaps due to aerosols (*Wild et al.*, 2005; *Liepert*, 2002; *Stanhill and Cohen*, 2001). The Earth's shortwave optical properties are not constant throughout the year, and their potential range of variability is not captured by this simple model. Nonetheless, the model indicates that variability in atmospheric annual mean reflectivity, absorptivity or transmissivity on the order of 10% will change λ_{land} by the observed amount. Note that *Wallace and Osborn* (2002) were unable to replicate the observed hemispheric phase shifts with a general circulation model, but the inclusion of aerosol forcing did decrease the modeled (incorrect) shift towards later seasons. We see no indication of shifts in mean λ_{land} after any of the major volcanic eruptions of the past century, though the effects of stratospheric and tropospheric aerosols on phase are likely to be quite different.

Thomson (1995) also made the intriguing, though difficult to evaluate, proposal that decreases in phase are due to an increased local sensitivity to anomalistic year forcing (associated with the annual cycle in Earth-Sun distance) relative to tropical year forcing (due to the annual cycle in the orientation of the Earth's rotation axis relative to the Sun).

The above mentioned changes in albedo, soil moisture, and shortwave forcing have all been implicated to also change modes of atmospheric circulation (*Cohen and Entekhabi*, 1999; *Yeh et al.*, 1984; *Lohmann and Feichter*, 2005). This raises the further possibility that shifts in atmospheric circulation participate in the modulation of the annual cycle. We focus on the Northern Annular Mode (NAM) and the Pacific North American pattern (PNA) as these have been shown to represent the bulk of the variability in standard atmospheric climate indices (*Quadrelli and Wallace*, 2004). The NAM shows significant cross-correlations with time-series of 1950-2007 spatially averaged λ_{land} ($R=-0.5$, $p<0.001$) and $\mathsf{G}_{\mathrm{land}}$ ($R=0.42$, $p=0.007$), while the PNA has significant correlation with $\mathsf{G}_{\mathrm{ocean}}$ ($R=0.3$, $p=0.04$). Apparently, atmospheric dynamical processes respond to similar forcing mechanisms as λ_{land} or themselves participate in altering λ_{land} through the advection of heat and moisture or other indirect processes. Northern Hemisphere snow cover, for example, is known to interact with the NAM (*Cohen and Entekhabi*, 1999; *Saito and Cohen*, 2003), and wind driven changes in mixed layer depth effect the thermal mass that the ocean presents to the atmosphere (*Kara et al.*, 2003).

The AMIP2 simulations have been found to capture the spatial pattern, but not the temporal pattern of NAM variability (*Cohen et al.*, 2005), just as we find that the models fail to capture the long-term trends in phase. However, the recent phase excursion is not entirely explained by the late 20^{th} century excursion in the NAM. A regression of the spatial average λ_{land} time series against the NAM index from 1950-2007 removes 25% of the variance and 40% of the trend in the λ_{land} time series, but still leaves a significant trend ($p<0.02$) of -1.0 days/(57 years) (see Supplementary Information).

The statistics of the distribution of λ_{land} trends are well described as natural variability from 1900-1953, but then the distribution shifts in 1954-2007 – the period in which anthropogenic interference with the mean becomes apparent. If we extend our natural control period back to 1850, the recent trends appear yet more anomalous. Numerous climate factors can influence the phase of the annual cycle, and it appears that some portion of the trend in the annual cycle is associated with changes in the NAM during the late 20^{th} century. We expect that a complete explanation for long-term shifts in atmospheric circulation will also encompass an explanation of the variability in the phase of the annual cycle. Though the mechanism is still uncertain, the tests we apply to the 1954-2007 trends in land phase indicate that they are inconsistent with natural variability, and thus appear to be due to anthropogenic influence.

2.5 Methods Summary

For each year of data, we calculate the 1/yr sinusoidal component using the Fourier transform as, $Y_x = \frac{2}{12}\sum_{t=0.5}^{11.5}(e^{2\pi i t/12} \cdot x(t+t_0))$, where $x(t+t_0)$ is 12 monthly values of either the demeaned monthly temperature or demeaned monthly insolation and t is time in months. The 2 is to account for both positive and negative frequencies. Phase is given by $\phi_x = \tan^{-1}\frac{Im(Y_x)}{Re(Y_x)}$. In order to discuss both hemispheres in a common framework, we referenced the temperature phase to that of local solar insolation. The difference between these two phases ($\lambda = \phi_T - \phi_{sun}$) is the *lag* (*Prescott and Collins*, 1951).

Amplitude is given by $A_x = |Y_x|$. For the purpose of understanding the response of Earth's temperature to forcing, we examine the *gain*, which is defined as the ratio of the amplitudes of the annual cycles in temperature and insolation, ($\mathsf{G} = \frac{A_T}{A_{sun}}$). Unlike insolation or temperature alone, G has very little latitude dependence.

If any of the 12 monthly temperature values is missing in the dataset at a given location, then no estimate of the annual cycle is made at that location for that year. Analysis using longer record pieces and more advanced filter techniques (3-year Hamming window, 5-year frequency modulated model) do not change our conclusions regarding the significance of phase and amplitude changes.

2.6 Methods

Data sets: When plotting full spatial fields (Fig. 1 and Fig. 2a), we use the HadCRUT3 blended land and ocean 5°×5° gridded surface temperature anomalies (*Brohan et al.*, 2006) plus gridded climatology (*Jones et al.*, 1999) from the Climate Research Unit at the University of East Anglia. For comparison with IPCC model archive output (Fig. 3), we also use the HadCRUT3 dataset (because models do not calculate separate land and ocean surface temperatures), but restrict ourselves to grid points which are more than 50% land. When land and ocean are considered separately (all other calculations), we substitute the CRUTEM3 (for land) and HadSST2 (for ocean) datasets so that the land and ocean signals are more cleanly separated. Dominantly land and ocean boxes are identified using the Clark US Navy Fleet Numerical Oceanographic Center Land/Ocean Mask (*Cuming and Hawkins*, 1981). Because a grid box with only a few percent land cover is not as representative of land as a continental interior box, only CRU grid points which are more than 50% land in the Navy mask are used in land calculations. Those with less than 50% land are considered ocean.

Data mask: We desire a high signal (annual amplitude) to noise (errors in observations and high frequency temperature variability) ratio such that we can isolate variability that is associated with changes in the annual cycle. In fact, the 1/yr sinusoidal component dominates the extratropical records; it explains an average of 96% and 90% of the within-year variance in monthly temperatures for land and ocean grid boxes respectively. With the time series of yearly G and λ at each gridbox, we estimated the long-term means, the long-term trends, as well as the standard deviations of the departures from the long-term trend. To do so, we excluded from analysis (*i*) those extratropical grid boxes where less then 85% of the average within-year variance is explained by the 1/yr sinusoidal component (primarily the Southern Ocean); and (*ii*) all tropical grid boxes (23.5S to 23.5N), because the 2/yr harmonic in forcing and response is strong in this region. For calculating long-term mean λ and G, we excluded grid boxes with fewer than 10 yearly estimates over the entire record. For calculating 54-year trends and detrended standard deviation in the G and λ, we excluded grid boxes with fewer than 40 yearly estimates. Trends were calculated using a least-squares fit. For comparing 1900-1953 and 1954-2007 trends, we used a ‘comparison network’ of grid boxes that meet this data-density criteria for both periods (180 land points, 120 ocean grid points). We also used a ‘dense network’ of all of the grid boxes that meet the data inclusion criteria for 1954-2007, in order to obtain a best estimate for the most recent period (299 land points, 345 ocean points). The ‘dense network’ has good spatial coverage between 25N and 60N (with some missing values in the interior of Eurasia and at higher latitudes) and more sporadic coverage between 25S and 40S. For the ‘comparison network’ all of the Southern Ocean, most of the Pacific Ocean, and much of Asia are excluded.

Trend distribution testing: Tests for the deviation of distribution means from zero were done using the t-test (2-tailed) and confidence intervals are t-intervals. The standard deviation for the t-test was calculated from the observed distribution and the degrees of freedom were estimated as the effective spatial degrees of freedom (ESDOF) of the time-varying field using the moment matching method of *Bretherton et al.* (1999), which they describe as appropriate when testing for the difference of a realization from the mean. This method estimates 21 (λ_{land}), 19 (λ_{ocean}), 12 (G_{land}) and 20 ($\mathsf{G}_{\text{ocean}}$) ESDOF for λ and G variability. For the late 'dense network', the estimates are 29 (λ_{land}), 58 (λ_{ocean}), 12 (G_{land}) and 47 ($\mathsf{G}_{\text{ocean}}$) ESDOF. For 'summer' temperature field variability we used 15 (land) and 9 (ocean) ESDOF for the 'comparison network' and 17 (land) and 30 (ocean) ESDOF for the 'dense network'. For 'winter' temperature field variability we used 8 (land) and 9 (ocean) ESDOF for the 'comparison network' and 6 (land) and 31 (ocean) ESDOF for the 'dense network'. For seasonal difference (summer-minus-winter temperature) hypothesis testing we used ESDOF values calculated from fields of annual mean temperature and we used values of 10 (land) and 9 (ocean) ESDOF for the 'comparison network' and 12 (land) and 22 (ocean) ESDOF for the 'dense network'. Recovered ESDOF estimates are comparable to the observation-based estimates of *Jones et al.* (1997) and are notably smaller than the model-based estimate of *Madden et al.* (1993). For testing the average summer and average winter trend distributions, summer was defined as June, July and August (JJA) in the Northern Hemisphere and as December, January and February (DJF) in the Southern Hemisphere. Winter was defined as DJF in the Northern Hemisphere and JJA in the Southern Hemisphere.

Energy balance model: The 1-box conceptual model is a 1-atmospheric-layer energy balance model, with a blackbody surface and a blackbody atmosphere, forced with sinusoidally varying shortwave radiation ($S = S_0 \cos 2\pi t$) characteristic of the annual cycle in radiation at 40°N. We added two complications: (*i*) To consider sensitivity to atmospheric optical properties, we specified atmospheric shortwave absorptivity ($\mathcal{A} = 0.15$), transmissivity ($\mathcal{T} = 0.6$), and reflectivity ($\mathcal{R} = 0.25$) and calculated the effects of multiple reflections following *Shell and Somerville* (2005); (*ii*) To consider the effects of increasing longwave optical depth (τ), we calculated a different atmospheric upward radiating temperature ($T_{up} = T_a - \Gamma H(\ln \frac{3\tau}{2} - 1)$) and downward radiating temperature ($T_{down} = T_a + \Gamma H$), which were related by the atmospheric height (H) and lapse rate (Γ), following *Goody* (1995, chap. 5). Surface temperature tendency is a function of the sum of energy fluxes divided by the thermal mass of the surface (c_s). On land, the depth of soil that contributes to the thermal inertia was estimated as the square root of the soil diffusivity times the timescale in question, and for annual timescales we used a depth of 4.7 meters in calculating c_s.

The surface energy budget is then

$$c_s \frac{\partial T_s}{\partial t} = S\left(\frac{\mathcal{T}(1-\alpha_s)}{1-\alpha_s\mathcal{R}}\right) + \sigma T_{down}^4 - \sigma T_s^4,$$

and the atmospheric budget is

$$c_a \frac{\partial T_a}{\partial t} = S\left(\mathcal{A} + \frac{\mathcal{A}\mathcal{T}\alpha_s}{1-\alpha_s\mathcal{R}}\right) + \sigma T_s^4 - \sigma T_{up}^4 - \sigma T_{down}^4,$$

where α_s is the surface albedo. The model was run for parameter values typical for land, and we then perturbed these values to estimate sensitivity.

Thermal mass changes are equated with soil moisture changes assuming a soil consisting of 10% inorganic matter, 45% organic matter, 5% unfilled airspace and with a soil water content of 40%. A 13% drop in soil moisture then implies that the soil water content drops to 35%.

Table 2.1. **Means of trend distributions:** Phase lag (λ) trends are in days/(54 years). Amplitude gain (G) trends are in $^\circ\mathrm{C}/\frac{\mathrm{kW}}{\mathrm{m}^2}$/(54 years). Temperature trends are in °C/(54 years). 2-tailed p-values are given in parenthesis. Significant values, judged using 95% confidence intervals, are in bold.

	comparison network		dense network
	1900-1953	1954-2007	1954-2007
λ_{land}	0.31±0.95 (p=0.5)	**-1.88±0.95 (p<0.001)**	**-1.66±0.81 (p<0.001)**
λ_{ocean}	0.72±1.24 (p=0.2)	0.00±1.23 (p=1)	**1.02±0.87 (p=0.02)**
$\mathsf{G}_{\mathrm{land}}$	0.23±2.21 (p=0.8)	**-2.62±2.40 (p=0.03)**	**-2.54±2.54 (p=0.05)**
$\mathsf{G}_{\mathrm{ocean}}$	0.44±0.82 (p=0.3)	0.27±0.69 (p=0.4)	0.43±0.47 (p=0.07)
Summer land	**0.54±0.37 (p=0.007)**	**0.86±0.38 (p<0.001)**	**0.96±0.35 (p<0.001)**
Summer ocean	**0.79±0.28 (p<0.001)**	**0.60±0.26 (p<0.001)**	**0.48±0.18 (p<0.001)**
Winter land	0.60±0.96 (p=0.2)	**1.66±1.00 (p=0.005)**	**1.77±1.40 (p=0.02)**
Winter ocean	**0.72±0.33 (p<0.001)**	**0.46±0.29 (p=0.005)**	**0.41±0.19 (p<0.001)**
Summer-Winter land	-0.06±0.83 (p=0.9)	-0.80±0.95 (p=0.09)	-0.81±0.94 (p=0.08)
Summer-Winter ocean	0.07±0.32 (p=0.6)	0.14±0.28 (p=0.3)	0.07±0.21 (p=0.5)

Chapter 3

Circulation and Orbital Modulation of the Annual Cycle of Surface Temperature

The observed 1954-2007 trends in the phase of the annual cycle of surface temperature on land are explained by the cumulative effects of orbital changes, aliases of the tropical year due to sampling of temperature on the Gregorian calendar, and changes in atmospheric circulation described by the Northern Annular Mode and the Pacific North America Pattern. These effects also appear to explain the contemporaneous amplitude gain trends, though this is less unambiguous. Ocean trends, in contrast, appear more significant after taking into account natural sources of variability.

3.1 Introduction

Much attention is given to changes in the annual mean temperature, but it is the annual cycle of temperature variability that dominates all instrumental surface temperature records. Systematic changes have been observed in the structure of the annual cycle in surface temperature in the late 20^{th} century (*Thomson*, 1995; *Mann and Park*, 1996; *Wallace and Osborn*, 2002; *Stine et al.*, 2009). However, the cause of observed phase and amplitude changes has not been determined (*Stine et al.*, 2009).

In previous work, we considered extratropical temperature records from both hemispheres and found large-scale shifts in the phase and amplitude of the annual cycle from 1954 to 2007 (*Stine et al.*, 2009). Land phase trends are towards earlier seasons (-1.66±0.81 days/54 years), are highly significant ($P<0.001$), and are anomalous when compared with the 1850-1953 variability. Ocean phase trends are, in contrast, towards later seasonality, (1.02±0.87 days/54 years, $P=0.02$). The oceanic temperature record before World War II is poor, and we are thus unable to evaluate whether the modern trend is anomalous compared to the earlier record. The significance of observed 1954-2007 amplitude trends is more marginal. Land amplitude decreased ($P=0.05$), and this decrease appears anomalous when compared with the 1900-1953 record. Ocean amplitude increased ($P=0.07$), but here too the absence of early data prevents us from assessing whether this trend is anomalous in the context of ocean variability.

The modern phase trend towards earlier seasons on land stands in contrast to the long-term phase trend at Central England, identified by *Thomson* (1995). The Central England Timeseries (*Manley et al.*, 1953; *Manley*, 1953; *Parker et al.*, 1992) extends at monthly resolution from 1659-present and is the longest surface thermometer time series we possess. Surprisingly, the phase of the annual cycle in surface temperature in this record (as interpreted by *Thomson* (1995)) shows a steady trend towards later seasons from 1659-1950 (a ∼4 day phase excursion over ∼280 years). This trend was interpreted as orbitally forced by *Thomson* (1995), a response to nonlinear interaction between the tropical and anomalistic years forced by precession of the Earth's equinoxes. After 1950, *Thomson* (1995) observed a much more rapid phase excursion towards later seasons (a ∼4 day phase excursion over ∼30 years), which he interpreted as a response to greenhouse forcing. Thomson also proposed the hypothesis that the mechanism for annual cycle phase response to greenhouse gas forcing involved changes in the interaction between the tropical and anomalistic year in solar insolation (*Thomson*, 1995), though this is a different mechanism than the one he proposed to explain the century-scale trends at Central England.

Modelling studies have consistently failed to explain the observed 20^{th} century phase shift as a response to either direct CO_2 forcing alone (*Mann and Park*, 1996), to combined greenhouse gas and aerosol forcing (*Wallace and Osborn*, 2002), or to the complete 20^{th} century forcing history (*Stine et al.*, 2009).

In this chapter we will systematically examine hypotheses (some old and some new) to explain the observed phase and amplitude trends, and then use these hypotheses to attempt to explain observed Northern Hemisphere phase and amplitude trends.

3.2 Calculation of Amplitude and Phase of the Annual Cycle

We calculate amplitude and phase of the annual cycle as the 1/year frequency component using the Fourier transform:

$$Y = \frac{2}{12} \sum_{t=0.5}^{11.5} 2\pi e^{2\pi i t/12} \cdot X(t) \tag{3.1}$$

where $X(t)$ represents 12 monthly values of surface temperature or solar insolation. From the Fourier transform we recover the amplitude:

$$A = |Y| \tag{3.2}$$

and phase

$$\phi = \tan^{-1} \frac{Im(Y)}{Re(Y)} \tag{3.3}$$

We use this formalism to calculate yearly estimates of ϕ and A.

3.3 Factors Influencing Amplitude and Phase of the Annual Cycle of Surface Temperature

3.3.1 Latitude

The annual cycle in surface temperature arises because of the annual cycle in solar insolation, which is a strong function of latitude. Solar insolation increases with distance from the Equator, and switches phase by ~180 degrees between the hemispheres.

Previous work on changes in the seasonality of surface temperature has focused on high latitudes, in part because that is where the annual cycle is largest (*Mann and Park*, 1996; *Wallace and Osborn*, 2002). We are interested in studying changes throughout the extratropics and are interested in changes in the physical response to forcing. We thus reference the annual cycle in surface temperature to the annual cycle in solar insolation.

Following *Stine et al.* (2009), we define the *gain* (G) as:

$$\mathsf{G} = \frac{A_{\text{temperature}}}{A_{\text{sun}}} \tag{3.4}$$

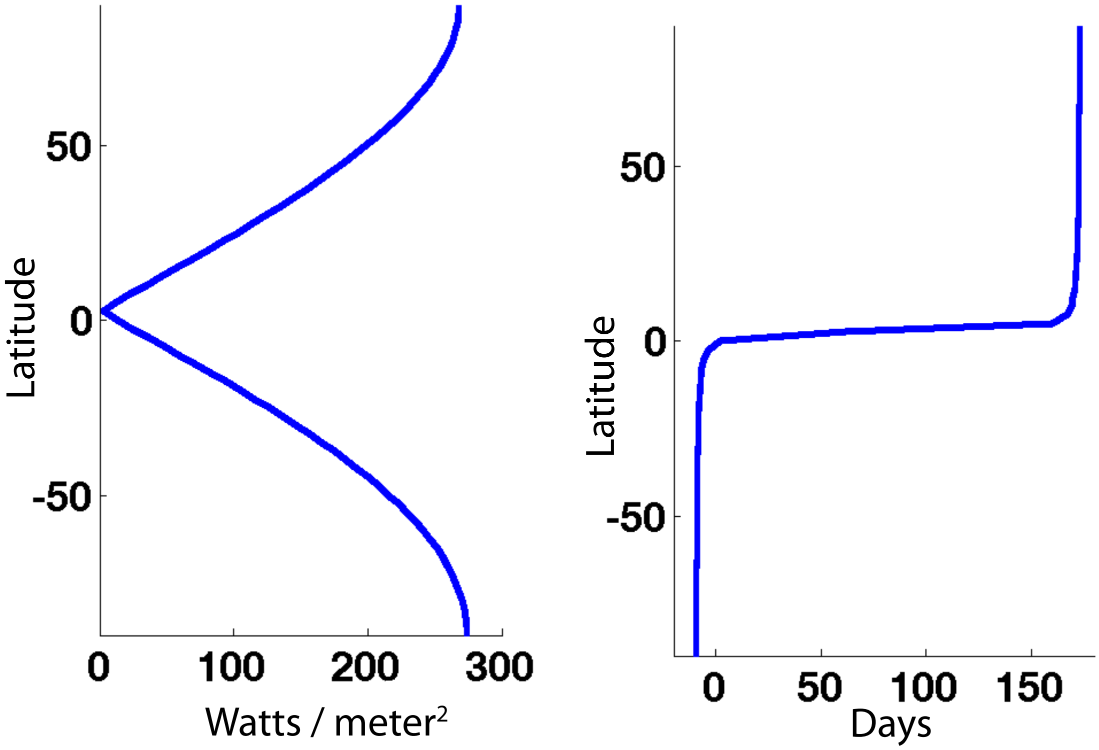

(a) Amplitude of solar insolation (b) Phase of solar insolation (expressed in days)

Figure 3.1. **Seasonality of solar insolation**. Amplitude and phase of 1/yr component of solar insolation vs. latitude, derived for the year 2000 CE from insolation tables of *Berger* (1991). **(Left panel):** Amplitude **(Right panel):** Phase.

and the *lag* (λ) as

$$\lambda = \phi_{\text{temperature}} - \phi_{\text{sun}} \tag{3.5}$$

where $A_{\text{temperature}}$ and $\phi_{\text{temperature}}$ are the amplitude and phase of the local annual cycle in temperature, and A_{sun} and ϕ_{sun} are the amplitude and phase of the annual cycle in local solar insolation. To first order, A_{sun} and ϕ_{sun} are simple functions of latitude (Fig. 3.1). In *Stine et al.* (2009) we defined both A_{sun} and ϕ_{sun} as functions of latitude, taking into account the elliptical nature Earth's orbit, which introduces an asymmetry between the hemispheres. In this chapter we extend the definition of A_{sun} and ϕ_{sun} to include time variability of both quantities due to orbital and calendrical effects.

3.3.2 Direct Orbital Effects

Referencing the annual cycle in surface temperature to the annual cycle in solar insolation is complicated by the fact that there are two distinct years in solar insolation. The mechanism for the origin of the seasons that we think of most often is the tropical year, which arises due to the tilt of the Earth's rotation axis relative to the plane of the Earth's orbit around the Sun (Fig. 3.2a). The anomalistic year in solar insolation, in contrast, arises due to the fact that the Earth rotates about the Sun in an ellipse, rather than in a circle (Fig. 3.2b). At perihelion, the point of the Earth's orbit when it is closest to the Sun, the intensity of solar insolation at the top of the Earth's atmosphere in the plane perpendicular to the Sun's rays is stronger than it is at other points on the Earth's orbit. This gives rise to a second annual cycle in solar insolation on the surface of the Earth, the anomalistic year.

The amplitude of the tropical year in solar insolation is zero at the Equator, increases as you move away from the Equator in either direction, and switches phase by 180 degrees between the hemispheres. The tropical year, however, has essentially[1] no effect on globally integrated insolation. In contrast, the anomalistic year in solar insolation is maximum at the Equator, decreases in amplitude as you move towards the poles, has the same phase at all points on Earth, and represents modulation of the total solar insolation incident at the top of Earth's atmosphere.

Due to slow changes in the Earth's orbit, the frequency of the tropical and anomalistic years are different. The frequency of anomalistic year forcing is determined by the time from perihelion to perihelion ($f_{\text{anomalistic}} = 1/365.259644\frac{1}{\text{days}}$). The tropical year is measured as the time interval from when the Earth's rotation axis has a particular inclination relative to the Sun, to when it returns to that same inclination angle the following year (for example, the time from vernal equinox to the following vernal equinox). Due to slow changes in the Earth's orbit, this time interval varies slightly depending on the reference position in the Earth's orbit that is chosen. We adopt a definition of the tropical year based on the average across all orbital positions (the "mean tropical year") which gives a frequency of $f_{\text{tropical}} = 1/365.242194\frac{1}{\text{days}}$. The difference between the frequencies of these two years in forcing arises due to precession of the Earth's rotation axis (relative to the constellations of distant stars), which is caused by gravitational forces acting on the Earth's equatorial bulge.

The once-per-year sinusoidal component of solar insolation is thus a result of the combination of these two years in solar insolation. Because these two "years" have slightly different frequencies, the phase relationship between the two years in forcing changes slowly over time, completing a full revolution every ~21,000 years. Earth's perihelion currently occurs around January 3^{rd}. The two years in insolation are thus nearly perfectly out-of-phase in the Northern Hemisphere, leading to dampening of the annual cycle, and near perfectly in-phase in the Southern Hemisphere leading to amplification of the annual cycle. In 1659 CE (at the start of the Central England Timeseries (*Manley*, 1953)) perihelion would have occurred 6 days earlier (around December 28^{th} on a calendar which perfectly tracked the tropical year).

One interesting consequence of the presence of two years in solar forcing is that maximum solar insolation does not occur at the summer solstice. In the Northern Hemisphere, the sum of tropical and anomalistic year forcing causes the maximum insolation to occur slightly

---

[1] "essentially" because the cross sectional area of the Earth that is presented to the Sun has a small seasonal cycle modulated by the tropical year due to the Earth's equatorial bulge.

before the summer solstice. In Roman times, the opposite was true; the maximum solar insolation occurred slightly after the summer solstice (in the Northern Hemisphere).

The implication for us is that even on a calendar that perfectly tracks the tropical year (the goal of most, if not all, solar calendars), the phase and amplitude of solar insolation vary with time. The phase and amplitude of the annual temperature response are expected to respond to these changes in forcing. Thus our definition of A_{sun} and ϕ_{sun} in Eqns. 3.4 and 3.5 should account for changes in the seasonality of insolation relative to the tropical year. We estimate the time variability of A_{sun} and ϕ_{sun} using the orbital calculations of *Berger* (1978, 1991) as implemented by *Huybers and Eisenman* (2006). The calculations of *Berger* (1991) give the solar insolation as a function of year, latitude and day of the (tropical) year. We generate time series of insolation for each desired calendar year. We then average these insolation time series to produce monthly solar insolation averaged, and calculate the phase and amplitude of solar insolation from these time series, using Eqn. 3.1, for each calendar year and and at each latitude. Changes in forcing from 1850-2010 give an indication of the importance of orbital changes in forcing over the nominal length of the instrumental record. Trends in daily insolation during this period exceed 1 Watt/meter^2 (comparable to the magnitude of annual mean anthropogenic forcing (*Forster and Ramaswamy*, 2007)), and are particularly strong in Northern Hemisphere autumn and Southern Hemisphere spring (Fig. 3.3).

Orbitally induced phase trends over the length of the instrumental record are towards earlier seasonal forcing in the Northern Hemisphere and towards later seasonal forcing in the Southern Hemisphere (Fig. 3.4a). Trends are strongest closer to the Equator, and decrease in magnitude as we approach the poles. Orbitally induced Northern Hemisphere extratropical phase trends range from 0.25 days per hundred years at the edge of the tropics to 0.07 days per hundred years at the North Pole. Orbitally induced amplitude trends have a somewhat more complicated structure (Figs. 3.4b and 3.4c). In the Southern Hemisphere, orbital trends currently decrease the amplitude of solar insolation by about 0.2 W/m^2 per hundred years, a value which is relatively uniform with latitude, though it represents a larger fractional change as one moves towards the Equator (Fig. 3.4b). In the Northern Hemisphere, orbital trends are decreasing the amplitude of solar insolation north of $\sim$40° N (by up to 0.1 W/m^2 per hundred years), and increasing the amplitude of solar insolation south of $\sim$40° N.

Accounting for these temporal changes in the Earth's orbit in Eqn. 3.5 thus leads to estimates of λ trends that are more positive, weakening the phase lag trend over land, and strengthening the phase lag trend over the ocean.

3.3.3 Calendrical Effects

Temperature observations are recorded relative to time and date on some calendar, not relative to the position of the Earth in its orbit or relative to the seasonal pattern of solar forcing. Humans express a strong preference for calendar years that contain an integer number of days, which necessitates some mismatch between the length of the calendar year,

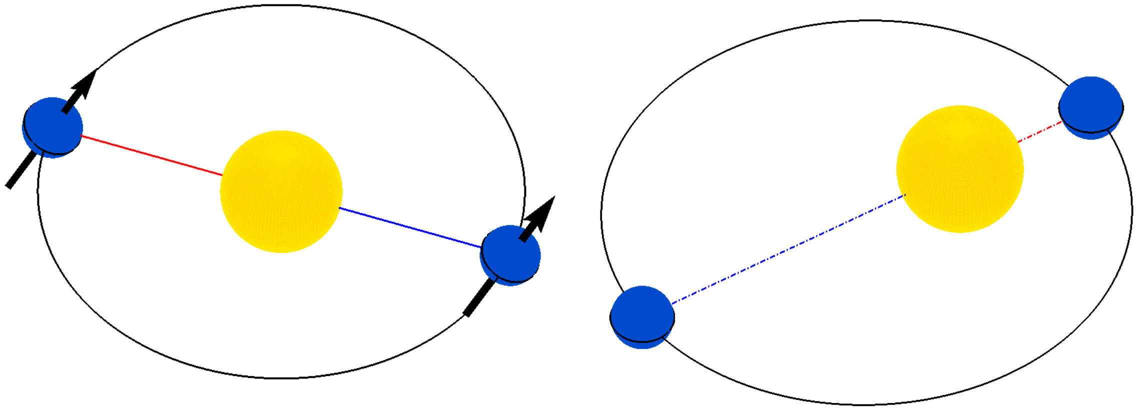

(a) Tropical Year

(b) Anomalistic Year

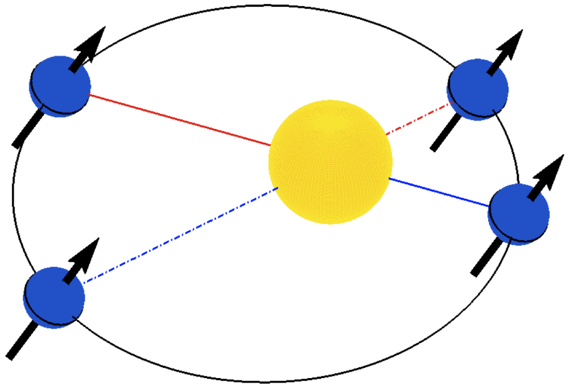

(c) Both

Figure 3.2. **Cartoon illustrating orbital geometry giving rise to tropical and anomalistic years in solar in insolation**. **(a)** Hypothetical orbital geometry which would produce only tropical year solar forcing. The orbit is circular when viewed from perpendicular to the plane of the Earth's orbit around the Sun. Annual period forcing arises due to inclination of the planet's rotation axis alone. Maximum Northern Hemisphere tropical year forcing occurs when the Northern Hemisphere is tilted towards the Sun (solid red line). **(b)** Hypothetical orbital geometry producing anomalistic year forcing. The orbit is elliptical, with one of the foci inside the Sun. Maximum anomalistic year forcing occurs when planet is at perihelion, its closest approach to the Sun (dotted red line). **(c)** Orbital geometry producing both years of insolation forcing. Maximum tropical year forcing position is indicated by solid red line. Maximum anomalistic year forcing is indicated by dotted red line. Slow procession of the equinoxes will change the distance in the orbit between these two events.

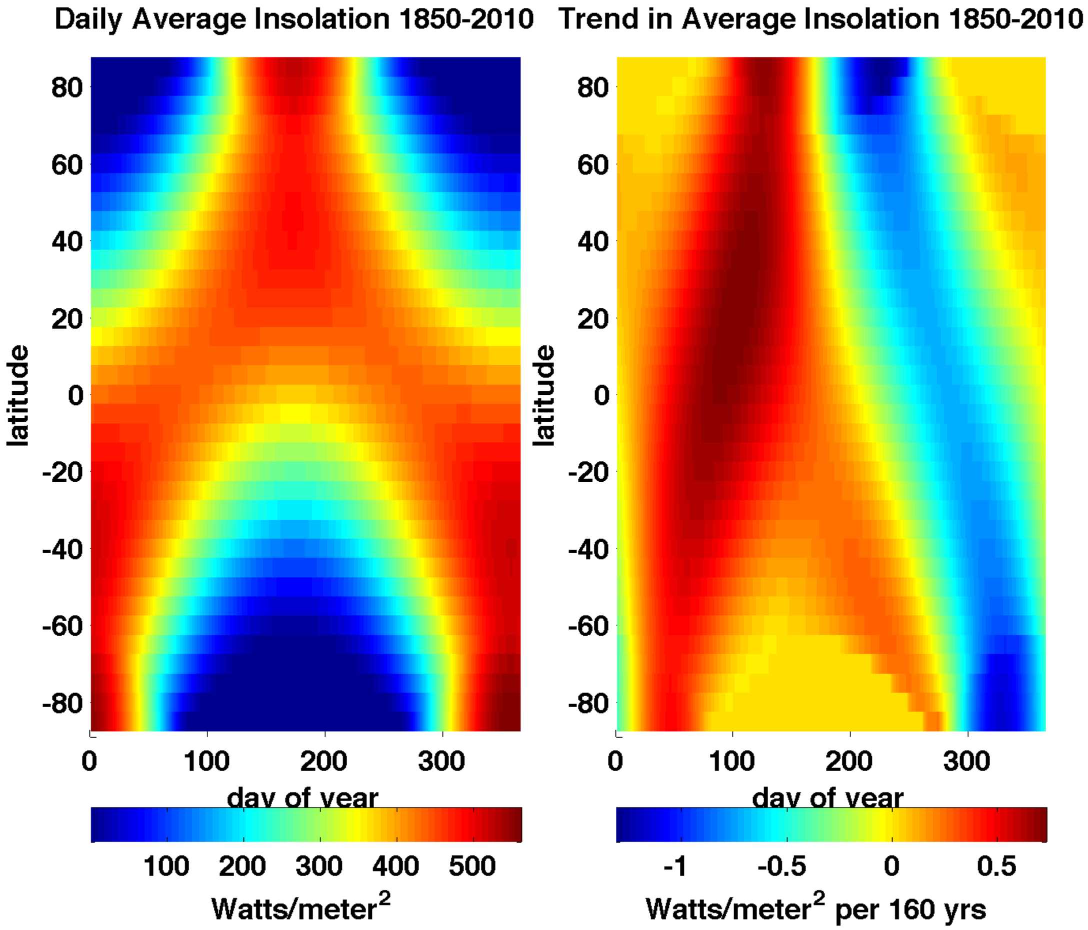

Figure 3.3. **Changes in seasonality of solar insolation associated with orbital changes, relative to the tropical year**. **(Left panel):** daily insolation (W/m^2) as a function of latitude and day of the (tropical) year, averaged over the period 1850-2007. **(Right panel:)** linear trend in solar insolation as a function of day of year (W/m^2/160 years). Day of year is fixed relative to the vernal equinox, a measure of the tropical year, so that linear trends represent trends relative to a calendar that follows the tropical year – these trends thus exist before introduction of calendrical drift and jitter when the year is forced to fit into the Gregorian (or some other integer-day-length) calendar. Insolation calculated using method of *Berger* (1978, 1991) as implemented by *Huybers and Eisenman* (2006).

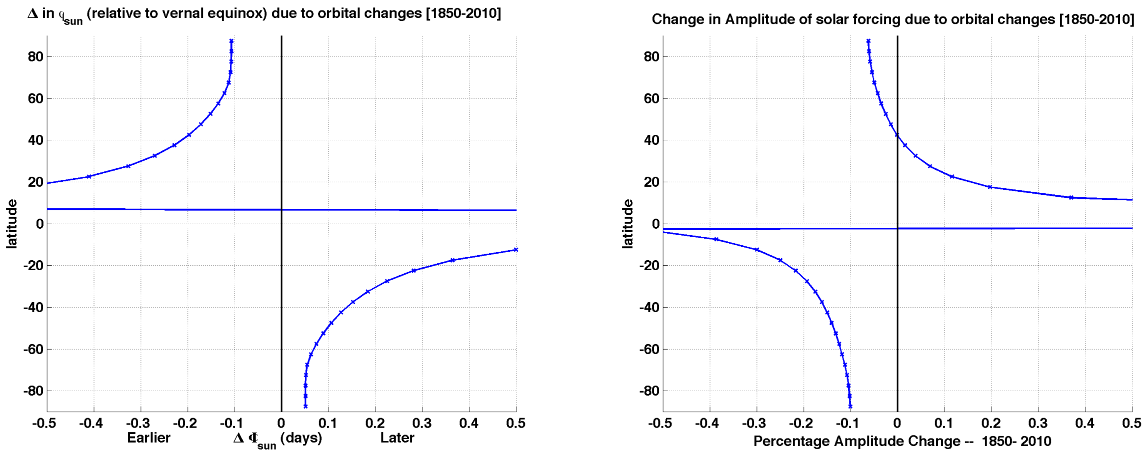

(a) Orbital change in insolation phase (b) [Orbital change in insolation amplitude (%)

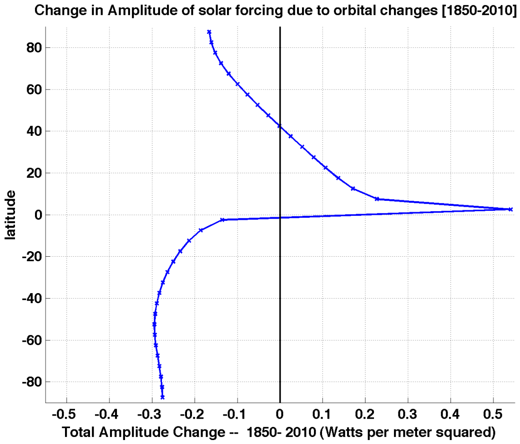

(c) Orbital change in insolation amplitude (W/m^2)

Figure 3.4. **Changes in the phase and amplitude of the 1/yr sinusoidal component of solar insolation forcing arising due to orbital changes from 1850 to 2010 vs. latitude. (a)** Changes in the phase of solar insolation relative to a calendar that tracks the tropical year (in days per 160 years). **(b)** Changes in the amplitude of solar insolation over the same period expressed as a percentage **(c)** Changes in the amplitude of solar insolation over the same period expressed as watts per meter squared.

and the length of the mean tropical year (365.242194 days). The Gregorian calendar damps long-term phase drift between the calendar and solar insolation by introducing leap years. One extra day is added to the year (February 29th) every fourth year; this leap year is skipped on years that are divisible by 100 (1700 CE, 1800 CE, 1900 CE), except for those that are also divisible by 400 (1600 CE, 2000 CE, 2400 CE). This gives a long-term frequency, over the entire 400 year cycle of 1/365.2425 days. This is closely enough matched to the frequency of the mean tropical year that the long-term drift of the Gregorian calendar year relative to the tropical year is only $\sim$1 day per 3268 years. However, the effective frequency of the Gregorian calendar on shorter timescales follows the tropical year less closely. We are concerned here with the implications of this calendrical misfit on the phase of the annual cycle of solar insolation as measured on the Gregorian calendar.

We estimate the phase of solar insolation by first creating a time series of daily solar insolation meant to represent the tropical year.

$$F_{sun}(t_{\text{days}}) = \cos\left(2\pi f_{\text{tropical}} \cdot t_{\text{days}} + \psi_{\text{tropical}}\right) \tag{3.6}$$

where F_{sun} is the (normalized) force of solar insolation for a location with sinusoidal tropical year insolation, f_{tropical} is the frequency of the tropical year $(\frac{1}{365.242194 \text{ days}})$, t_{days}=1,2,3, ... , is a day counter and ψ_{tropical} is the initial phase of tropical year insolation as sampled on the Gregorian calendar (which effects the phase itself, but not the phase trends).

We then sample this daily record using the rules of the Gregorian calendar. Starting with a particular calendar year in mind (1954 in the case of Fig. 3.5a and 1650 in the case of Fig. 3.5b), we average the first 31 days of the synthetic record to give an averaged January insolation for the first year, and then average the next 28 or 29 days (depending on whether or not the starting calendar year is a leap year on the Gregorian calendar) as February insolation of the first year. We continue this process for as many years as desired to recover a synthetic monthly tropical year insolation record as sampled on the Gregorian calendar. We then calculate the phase of this insolation for each calendar year using the Fourier transform (Eqn. 3.1).

The effect of leap years is to introduce a jitter in the phase of tropical year insolation as sampled on the Gregorian calendar (Fig. 3.5), which occurs on 4-year, 100-year, and 400-year timescales. Over the 3-year period in which no leap year occurs, the calendar year has a frequency of 1/(365 days), and the phase of the tropical year drifts rapidly towards later seasonality. The once-per-four-years leap day corrects for this phase drift, producing a saw-toothed jitter in the phase of insolation forcing as sampled by the Gregorian calendar with amplitude 0.75 days (Fig. 3.5a). However, this is a slight over-correction which leads to a weaker drift of the tropical year on the Gregorian calendar towards earlier seasons over the four-year leap-year cycle that we have effectively been following since 1900 (the long-term drift in Fig. 3.5a). Over this four-year leap-year cycle, the effective frequency of the Gregorian year is 1/(365.25 days). Expanding our time window once again, the skipped leap years in 1700 CE, 1800 CE and 1900 CE correct for the drift of the 4-year cycle. This is also a slight over-correction, producing a sawtooth jitter of amplitude 0.99 days on 100-year timescales, and a slow drift towards later tropical year insolation as measured on the

Gregorian calendar (Fig. 3.5b). Over this 100-year leap-year cycle, the effective frequency of the Gregorian year is 1/(365.24 days). Finally, note that, unlike 1700 CE, 1800 CE and 1900 CE, there was in fact a leap day in 2000 CE (Fig. 3.5b), the final correction in the Gregorian calendar sequence, which brings the long term frequency to 1/365.2425 days.

3.3.4 Continentality

The land-sea contrast plays a dominant role in controlling the climatological annual cycle pattern (*Prescott and Collins*, 1951; *Ward*, 1906; *Jain et al.*, 1999; *Jones et al.*, 1997). The ocean surface simply has much larger thermal inertia and its temperature response to seasonally-variable solar insolation is much slower than that of land. Water is so important for controlling the thermal inertia of the surface that even on land the dominant control of thermal inertia is the amount of water present in the surface layer (*Bonan*, 2002), which led us to speculate that the signal of time-variable changes in soil moisture on land might be detectable by monitoring variability of phase and amplitude of the annual cycle (*Stine et al.*, 2009). The strength of this relationship is particularly clear when viewed in terms of lag (λ) and gain (G) (e.g. after we have accounted for the variable insolation forcing with latitude).

Figure 3.6a shows long-term-mean λ plotted against G for Northern Hemisphere extra-tropical grid boxes. The grid points fall on an arc typical of what is seen anytime two sinusoids of different amplitudes interact. At one end of the arc (high G, small λ) are continental points that are very isolated from the ocean. By "very isolated" we mean that one has to go a long way to the west (counter to the prevailing wind direction in midlatitudes) before one encounters any ocean. At the other end of the arc (low G, large λ), are oceanic points that are far from land in the sense that one has to go a long way to the west before one encounters a continent. The position of an individual grid box along this continuum (SRI) is well predicted by the distance between a grid point and the coast to its west (R=0.88; Fig. 3.7). "Westward distance from the coast," however, is itself an imperfect metric for continentality. Consideration of the spatial pattern of continentality and westward distance from the coast indicates that the seasonal response index (SRI) of *Stine et al.* (2009) is, in fact, a better metric of continentality than "westward distance."

The curvature of the mixing line between the land and ocean is a robust feature of any seasonally driven model that contains interacting land and ocean regions and can be understood as the natural consequence of interacting sinusoids. We present an analytical relationship for the nonlinear interaction between amplitude and phase in *Stine et al.* (2009). Some intuition into this relationship can be gained by looking at the shape of weighted averages of two sine waves. Fig. 3.8a presents visually the effect of averaging two sine waves of different amplitude and phase. Here the apexes of each sine wave (red dots) indicate the amplitude and phase of the sinusoid and trace out the shape of the nonlinear relationship between amplitude and phase. The result is that when weighted averages of a large and small sine wave of different phases are taken, the large amplitude sine wave is more stable

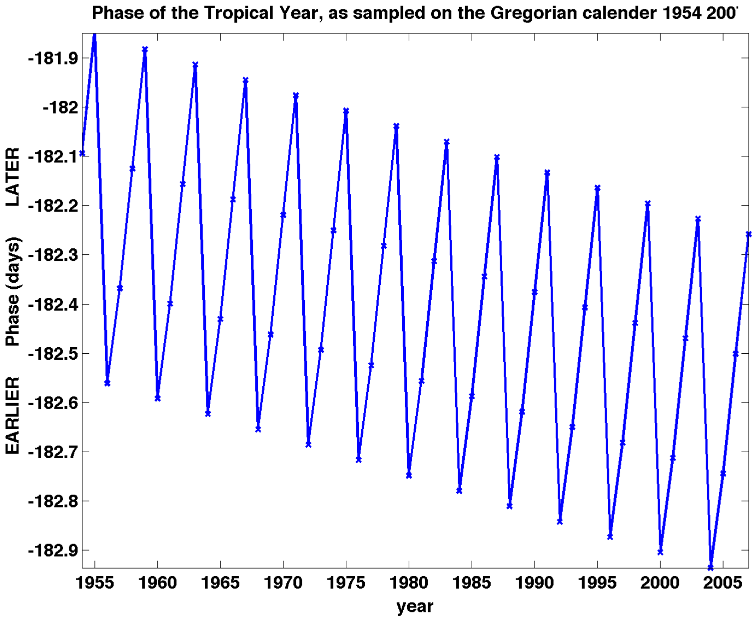

(a) 1954-2007

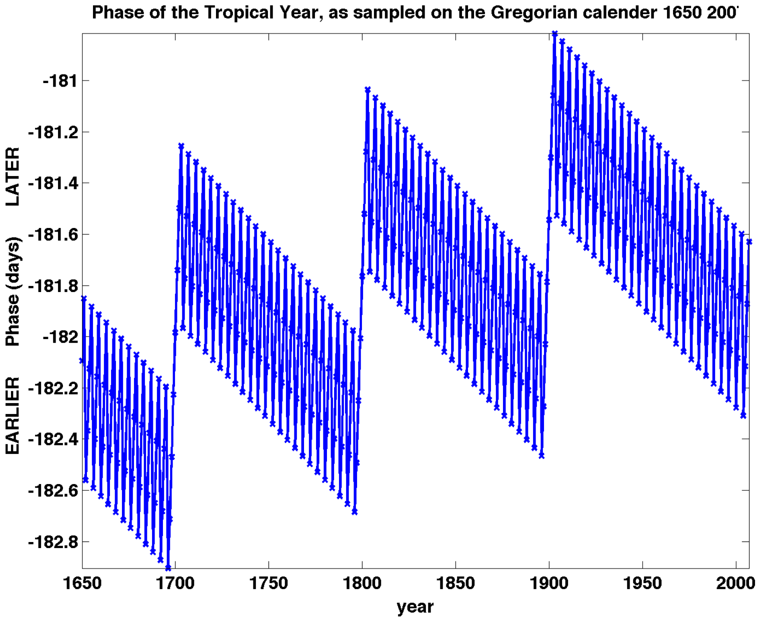

(b) 1650-2007

Figure 3.5. **Phase variability arising due to aliasing of the tropical year by sampling on the Gregorian calendar**. The introduction of leap years leads to jitter in the phase time series with a 4-year periodicity (upper panel), 100-year periodicity (lower panel) and 400-year periodicity.

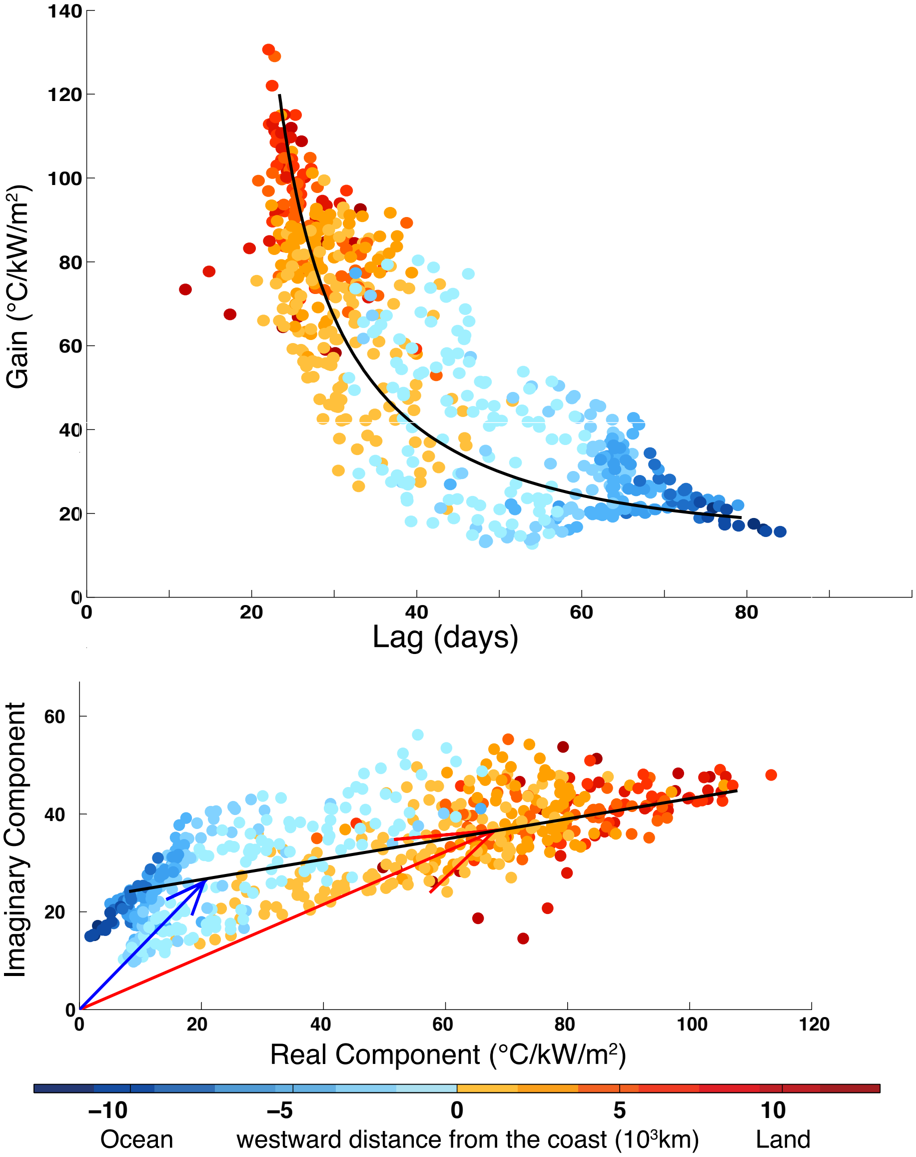

Figure 3.6. **Extratropical Northern Hemisphere relationship between seasonal parameters:** a **Upper Panel:** Observed relationships between local gain (G) and lag (λ) for Northern Hemisphere extratropical locations. Points represent long term mean λ and G for an individual grid box. Color represents distance one must travel to the west from the grid point to reach the coast (positive for land, negative for ocean). Outliers with λ<20 days are from Indian Subcontinent and presumably reflect monsoon dynamics. Black line shows nonlinear relationship between amplitude and phase for weighted averages of two end-member sine waves. **Bottom Panel:** Same, but plotted in the complex plane ($\mathsf{G}(\cos\lambda + i\sin\lambda)$). Red arrow shows the complex-plane vector represented by a typical land grid box. Blue arrow shows the complex-plane vector represented by a typical ocean grid box.

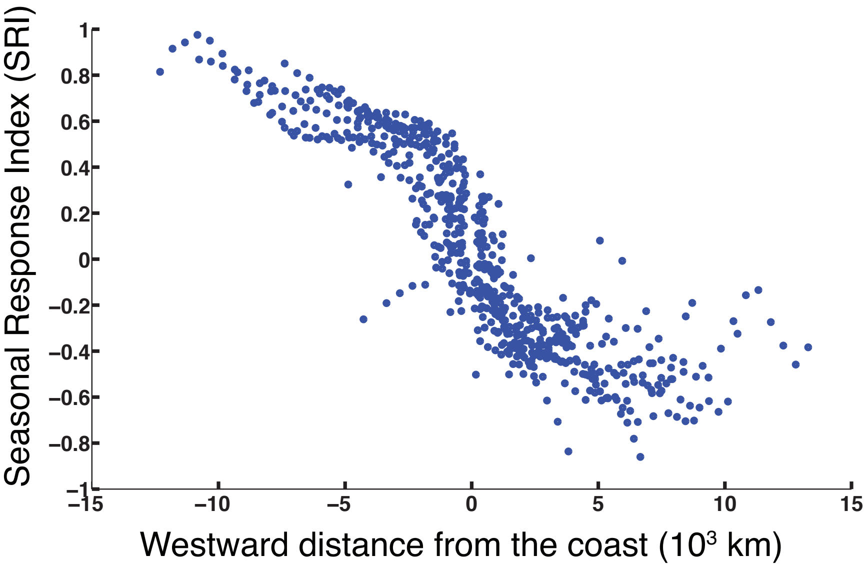

Figure 3.7. **Seasonal Response Index (SRI) vs westward distance from the coast:** Seasonal Response Index (SRI) versus westward distance from the coast for extratropical Northern Hemisphere grid boxes (R=0.88). Westward distance is defined as the distance one must travel due west from the grid box before encountering a grid box of the opposite surface cover type, and is positive for land grid points and negative for ocean grid points.

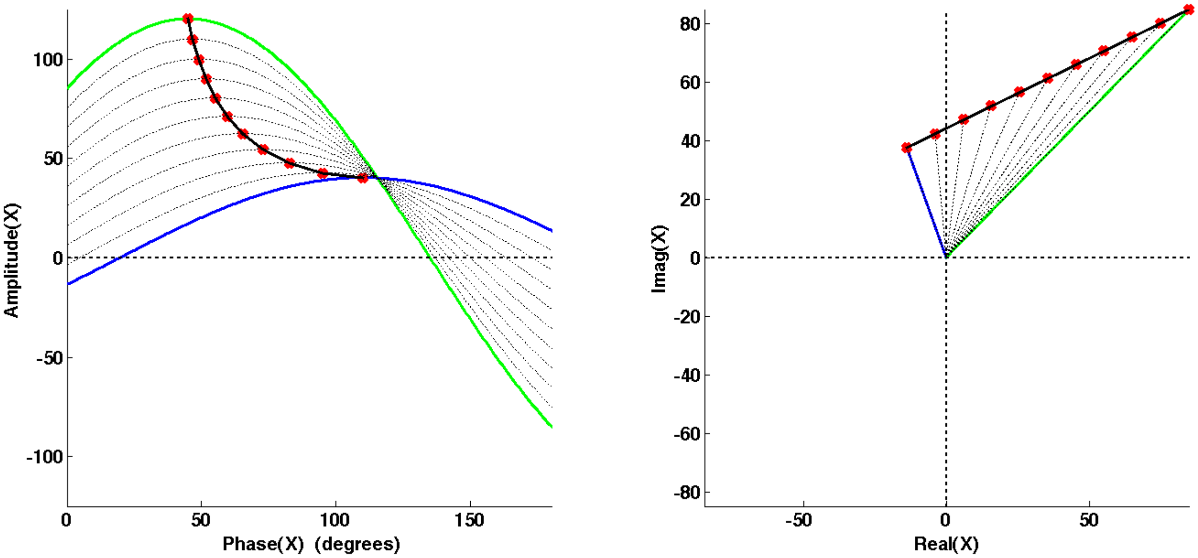

Figure 3.8. **Conceptual model for understanding relationship between seasonality parameters and continentality**. Effect of taking weighted averages of two sin waves, meant to illustrate the origin of the observed mixing line between land and ocean seasonality shown in Fig. 3.6. The green curves are meant to represent a continental end-member. The blue curves are meant to represent an ocean end-member. Dotted black lines represent weighted averages of land and ocean end-members. Red dots represent in the left panel give the apex of individual weighted averages which also gives amplitude and phase of the sine wave in phase/amplitude space. Red dots in the right panel represent the same weighted averages as vectors in the complex plane. Solid black lines represent continuous mixing line between land and ocean end-members, analogous to the solid black lines in Fig. 3.6. **(Left panel):** shown in time domain. **(Right panel):** shown in complex plane.

against perturbations in phase, and the small amplitude sine wave is more stable against perturbations in amplitude. The physical basis for this is readily apparent by considering the line that is formed by weighted averages of the same two sine waves when represented as vectors on the complex plane (Fig. 3.8b). The observed relationship between λ and G (Fig. 3.6) has the same form as predicted by this simple conceptual model.

This nonlinear relationship between amplitude and phase also gives insight into the differences in temporal variability seen at different locations. The pointwise relationship between climatological λ and G and their variability can be visualized as covariance ellipses. In figure 3.9a, each ellipse represents the long-term-mean and the variability at a single Northern Hemisphere extratropical grid box. Each ellipse is centered at the long-term-mean λ and G for the particular grid box. The semi-major axis of the covariance ellipse represents the first eigenvector (scaled by the first eigenvalue) of the pointwise covariance matrix between λ and G. Likewise, the semi-minor axis represents the second eigenvector (scaled by the second eigenvalue) of the same covariance matrix. Color represents westward distance from the coast as given in figure 3.6, where positive values (red tones) represent land, and negative values (blue tones) represent ocean. Ellipses are thus elongated in proportion to their variability in a particular direction. If the semi-major and semi-minor axes are parallel to the x- and y-axis, then λ and G variability are independent (their covariance matrix is diagonal), and the length of the semi-major and semi-minor axes represent the standard deviation of λ and G in each direction (times a constant of 1.178, which arises because these are bivariate covariance ellipses). The black line represents the nonlinear relationship between λ and G.

Temporal G variability is greatest on land and correlates strongly with long-term-mean G (R=0.83). We thus expect to observe larger amplitude trends where the amplitude is large due to natural variability alone. Conversely, temporal variability in λ is largest on the ocean, and is correlated with the inverse of G (R=0.62). This structure can be understood as related to the fact that a random perturbation of some finite size will more readily alter the phase of a small amplitude sinusoid than a large sinusoid. We can think of the ocean phase as being less stable due to the simple fact that the annual cycle is not as big over the ocean.

The addition of randomly-phased noise with the same magnitude everywhere produces λ variability $\sim\mathsf{G}^{-1}$. This can be understood by viewing variability in the complex plane, where perturbations are represented by a radial component and an azimuthal component (Fig. 3.9b). The radial component of the noise alters the gain ($\Delta\mathsf{G}$). The azimuthal component (ΔAz) of the noise alters the phase, but the observed change in phase is also a function of G ($\Delta\lambda = \frac{\Delta Az}{\mathsf{G}}$). The observed azimuthal component of temporal variability scales with the long-term-mean G (R=0.83). Note that this is the same scaling relationship we find between G variability and long-term-mean G. Thus, despite the fact that the variance in phase ($(\Delta\lambda)^2$) is larger on the ocean, the variance in the temperature perturbations associated with this variability ($(\Delta Az)^2$) is larger on land because the phase perturbations are acting on a larger amplitude sinusoid. The variability appears to have a simple, understandable (and surprisingly linear) structure if viewed in the proper framework. An argument could be made that we should be studying variability in azimuthal excursion, not variability in λ, because it is the energetically relevant quantity. However, the same conclusions are reached if the trend analysis is done using azimuthal excursion, rather than λ.

If the pointwise variability is of random phase, the ratio of radial to azimuthal perturbations should be 1. In fact the average ratio is 1.14 ($\sigma = 0.17$) over land and 1.15 ($\sigma = 0.18$) over the ocean. The component of noise that maps onto amplitude variability of the annual cycle is ~15% stronger than the component that maps onto phase variability, perhaps because wintertime variability is larger than in any other season.

3.3.5 Circulation

We test a number of climate indices against time series of the spatial average land and ocean lag (λ) and gain (G) using the definition of λ and G used in Chapter 2. (See section 3.6 of *Trenberth et al.* (2007) for definition and discussion of each index.) We find a number of cross-correlations significant, the most significant being the relationship between λ_{land}

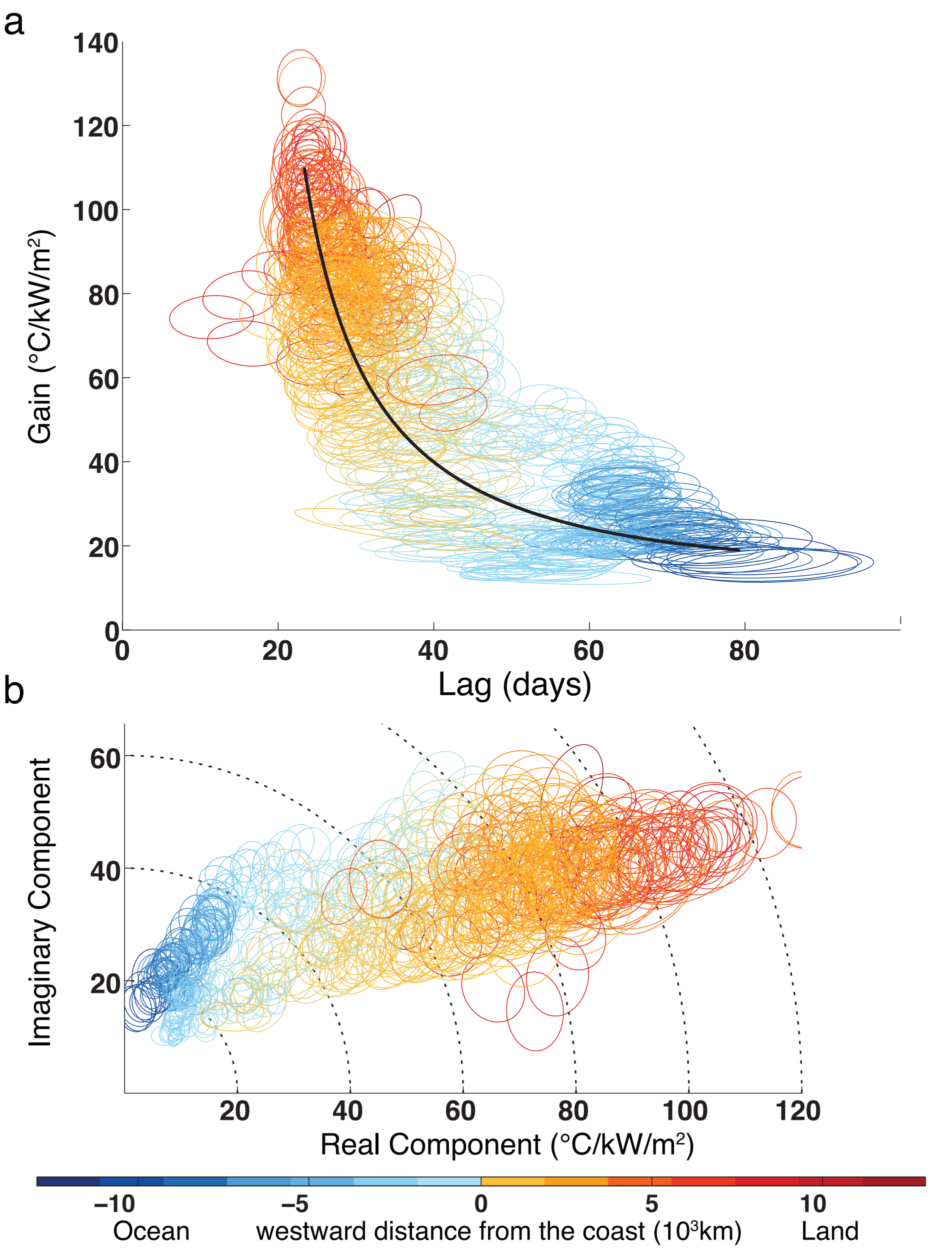

Figure 3.9. **Extratropical Northern Hemisphere relationship between seasonal parameters: Upper Panel:** Observed relationships between local gain (G) and lag (λ) for Northern Hemisphere extratropical locations. Center of ellipse represents long-term mean λ and G for individual grid box. Ellipses represent variability in each direction; the semi-major and semi-minor axes are the eigenvectors (scaled by their eigenvalues) of the local λ/G temporal covariance matrix. Alternatively, they can be thought of as level curves of the bivariate probability density functions. Color represents distance one must travel to the west from the grid point to reach the coast (positive for land, negative for ocean). Outliers with $\lambda<20$ days are from the Indian Subcontinent and presumably reflect monsoon dynamics. The black line shows the nonlinear relationship between amplitude and phase for weighted averages of two end-member sine waves **Bottom Panel:** Same, but parameters are plotted in the complex plane ($\mathsf{G}(\cos\lambda + i\sin\lambda)$)

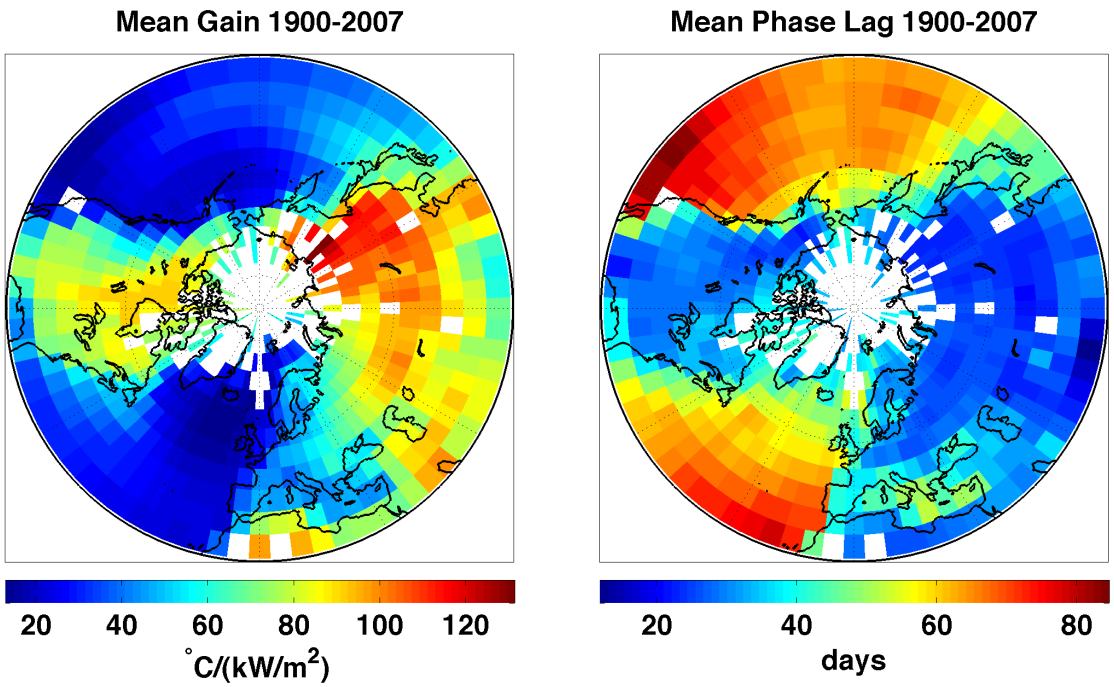

(a) Gain Climatology

(b) Lag Climatology

Figure 3.10. **Climatological λ and G** obtained by averaging annual values for λ and G at each grid point from 1900-2007. Shown for grid boxes north of 25° N. Grid boxes where less than 10 estimates were possible are left blank (white boxes).

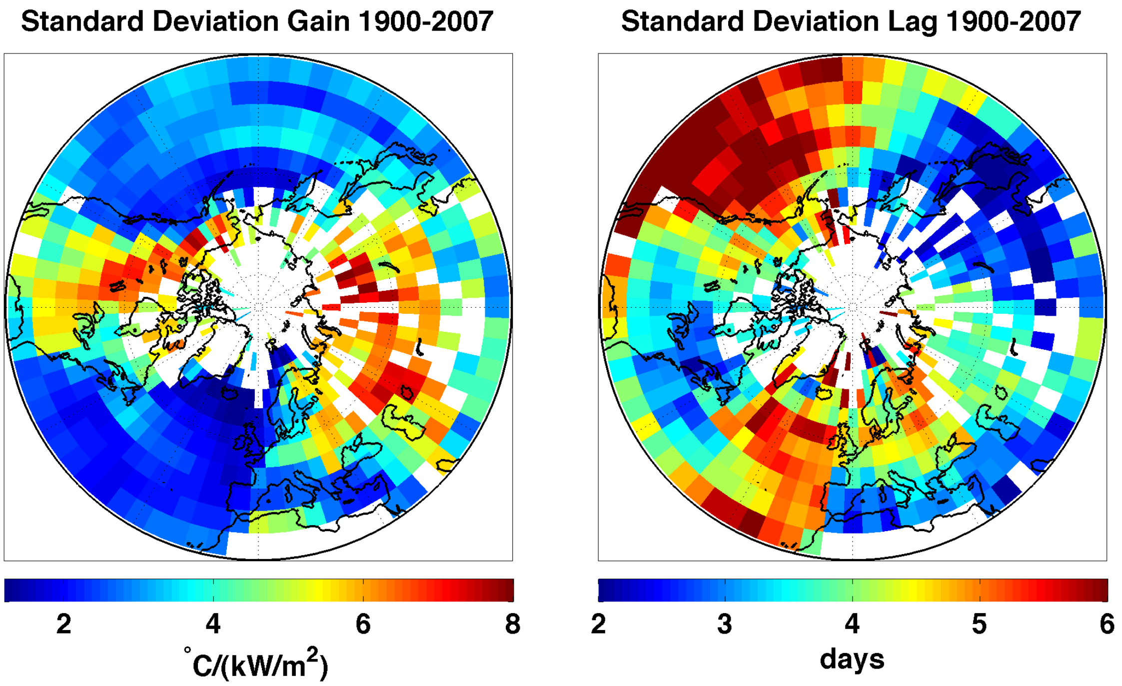

(a) Gain Variability

(b) Lag Variability

Figure 3.11. **Pointwise variability of λ and G. (Left Panel:)** Standard deviation of pointwise detrended time series of λ from 1900-2007. Grid boxes where less than 40 estimates were possible are left blank (white boxes). **(Right Panel:)** Same, but for G.

and the Northern Annular Mode (NAM) index (R=-0.50, p<0.001) (Table 3.2). The NAM also exhibits significant cross-correlation with G_{land} (R=-0.42, p=0.007). The North Atlantic Oscillation (NAO), a closely related index (*Wallace*, 2000), also exhibits a significant relationship with λ_{land} (R=-0.42, p=0.007). The Pacific/North American (PNA) index shows a significant relationship with $\mathsf{G}_{\text{ocean}}$ variability (R=0.30, p=0.04), and the Southern Oscillation Index (SOI) exhibits significant cross-correlation with λ_{ocean} (R=-0.32, p=0.02). No significant relationships are found between annual cycle parameters and the Pacific Decadal Oscillation (PDO) index or the Southern Annular Mode (SAM) index.

It is also of interest that λ_{land} and G_{land} are significantly correlated (R=0.43, p=0.009), as are λ_{ocean} and $\mathsf{G}_{\text{ocean}}$ (R=0.33, p=0.004), emphasising the intimate relationship between amplitude and phase.

All cross-correlations are done between 1950 and 2007, except for correlations with the SAM which begin in 1979. Significances are assessed using a Monte-Carlo approach, which accounts for the temporal autocorrelation of the time series. Phase of the climate index and annual cycle parameter are randomized and correlations are computed (100,000 iterations) to build up a distribution against which to test (2-tailed) significance.

Land and ocean spatial average time series are constructed by separately averaging those λ and G time series from the 152 land locations and the 227 ocean locations used in *Stine et al.* (2009) that have complete temporal coverage from 1950-2007.

Index values for the NAM, the NAO, the PNA pattern, and the SAM are taken from the National Oceanic and Atmospheric Administration's Climate Prediction Center (*Barnston and Livezey*, 1987; *Mo*, 2000). Index values for the PDO are taken from values derived by the University of Washington's Joint Institute for the study of the Atmosphere and Ocean (*Zhang et al.*, 1997). Values for the SOI are taken from the National Center for Atmospheric Research's Climate & Global Dynamics Climate Analysis Section (*Trenberth*, 1984).

Table 3.1. **Correlations between annual cycle parameters and standard climate indices 1950-2007:** P-values are generated by using a 2-tailed, Monte-Carlo approach. Relationships that are significant at more than 95% confidence are in bold. λ and G are defined by reference to solar insolation phase and amplitude which change with latitude, but not time (the definition used in Chapter 2).

	land lag (λ_{land})	ocean lag (λ_{ocean})	land (G_{land})	ocean gain ($\mathsf{G}_{\text{ocean}}$)
λ_{land}	-	R=0.04 (p=0.8)	**R=0.43 (p=0.009)**	R=0.00 (p=1)
λ_{ocean}	R=0.042 (p=0.8)	-	R=-0.11 (p=0.6)	**R=0.33 (p=0.004)**
G_{land}	**R=0.43 (p=0.009)**	R=-0.11 (p=0.6)	-	R=0.13 (p=0.3)
$\mathsf{G}_{\text{ocean}}$	R=0.00 (p=1)	**R=0.33 (p=0.004)**	R=0.13 (p=0.3)	-
land temp	R=-0.33 (p=0.12)	**R=0.45 (p=0.009)**	**R=-0.56 (p=0.002)**	**R=0.39 (p<0.001)**
ocean temp	R=-0.18 (p=0.6)	R=0.34 (p=0.09)	R=-0.24 (p=0.5)	**R=0.44 (p<0.001)**
time	**R=-0.47 (p=0.005)**	R=0.31 (p= 0.2)	**R=-0.46 (p=0.04)**	R=0.19 (p=0.2)
PDO	R=-0.2 (p=0.3)	R=0.12 (p=0.6)	R=-0.33 (p=0.1)	R=-0.02 (p=0.9)
PNA	R=-0.00 (p=1)	R=0.18 (p=0.2)	R=-0.16 (p=0.2)	**R=0.30 (p=0.04)**
NAO	**R=-0.42 (p=0.007)**	R=0.10 (p=0.6)	R=-0.31 (p=0.1)	R=-0.20 (p=0.1)
NAM	**R=-0.50 (p<0.001)**	R=0.12 (p=0.5)	**R=-0.42 (p=0.007)**	R=-0.28 (p=0.06)
SAM	R=-0.01 (p=1)	R=-0.02 (p=0.9)	R=0.03 (p=0.9)	R=0.11 (p=0.6)
SOI	R=-0.01 (p=1)	**R=-0.32 (p=0.02)**	R=0.13 (p=0.4)	R=-0.10 (p=0.5)

3.4 Implication for the Interpretation of 1954-2007 Phase and Amplitude trends

In Chapter 2 (*Stine et al.*, 2009) we established the presence of large-scale temporal trends in the phase lag and and amplitude gain of the annual cycle of surface temperature. There we tested the large-scale relationship between phase and the Northern Annular Mode (NAM) and found that we were not able to explain the entire late 20^{th} century phase excursion by trends in the NAM alone. In *Stine et al.* (2009) we defined λ and G by referencing them to an estimate of the amplitude and phase of solar insolation that was calculated based on the latitude (θ) of the observation alone.

$$A_{sun} = A_{sun}(\theta) \tag{3.7}$$
$$\phi_{sun} = \phi_{sun}(\theta) \tag{3.8}$$

However, as we have shown above, orbitally and calendrically induced variability in solar insolation on the Gregorian calendar on which we measure temperature are non-negligible, which effects our interpretation of phase trends.

3.4.1 Methods

Our approach here differs from that used in Chapter 2 in three ways.

1. We adopt a definition of λ and G referenced to the temporally varying phase and amplitude of solar insolation. That is, we define λ using Eqn. 3.5, but including the temporal variability in ϕ_{sun} such that:

$$\begin{aligned} \phi_{sun} &= \phi_{sun}(\theta, t) && (3.9) \\ &= \phi^{lat}_{sun}(\theta) + \phi^{orbit}_{sun}(\theta, t) + \phi^{greg}_{sun}(t) && (3.10) \end{aligned}$$

   where $\phi^{lat}_{sun}(\theta)$ is the solar phase as a function of latitude used in Chapter 2, $\phi^{orbit}_{sun}(\theta, t)$ represents a temporal correction due to orbital drift of the the phase of the annual cycle of insolation relative to the mean tropical year (Fig 3.4a), and $\phi^{greg}_{sun}(t)$ represents a temporal correction due to jitter and drift of the Gregorian calendar relative to the tropical year (Fig. 3.5).

   We likewise adopt a definition of G using Eqn. 3.4 such that:

$$A_{sun} = A_{sun}(\theta, t) \tag{3.11}$$

   where $A_{sun}(\theta, t)$ is calculated accounting for the temporal variability in the amplitude of the annual cycle in insolation due to (latitude dependent) temporal changes in the Earth's orbit (Figs. 3.4b and 3.4c).

2. In Chapter 2 we considered only the relationship between the Northern Annular Mode and the spatial average of land phase. However, the sense of dynamical modulation of phase may be quite different between one location and another. Here we will determine and account for the spatially varying dynamical modulation of λ and G in order to construct a theory for dynamic control of seasonality.

3. In Chapter 2 we considered extratropical observations from both hemispheres. Here we restrict ourselves to Northern Hemisphere extratropical stations because the dynamical modes of circulation that we are considering are defined based on their Northern Hemisphere influence.

3.4.2 Data

We consider gridded surface temperature data from the University of East Anglia's Climate Research Unit (CRU). When plotting spatial fields of λ and G trends and correlation patterns, (Figs. 3.12, 3.13a, 3.13c, 3.14a and 3.14c), we use the HadCRUT3 blended land-and-ocean $5^\circ \times 5^\circ$ gridded surface temperature anomalies (*Brohan et al.*, 2006), plus gridded climatology (*New et al.*, 1999). When considering land and ocean separately, we instead use the CRUTEM3 (for land) (*Jones et al.*, 1999) and the HadSST2 (for ocean) (*Rayner et al.*, 2003, 2006) data sets in order to cleanly separate land and ocean in those grid boxes that contain both surface cover types. Because a grid box whose surface coverage is only a few percent land is not as representative of land as a continental interior box, we restrict ourselves to using CRUTEM3 data in grid boxes that are more than 50% land (as determinted using the Clark US Navy Fleet Numerical Oceanographic Center Land/Ocean Mask (*Cuming and Hawkins*, 1981)). We likewise restrict ourselves to using HadSST grid boxes that are at least 50% ocean cover, as determined by the same metric.

For comparisons of λ and G variability against dynamical variability, we used the Arctic Oscillation time series constructed by NOAA's Climate Prediction Center to represent the NAM (*Zhou et al.*, 2001; *Miller et al.*, 2003) and we used the PNA estimate published by the University of Washington's Joint Institute for the Study of Atmospheres and Oceans (*Wallace and Gutzler*, 1981; *Zhang et al.*, 1997). We constructed annual time series of the NAM and PNA by averaging the the 12 monthly values of these time series for each year. We constructed a representation of the spatial pattern of the surface temperature loading pattern of each index (Figs. 3.13b,3.14b, 3.13d,3.14d) by regressing DJFM monthly time series of hemispheric NAM and PNA indices against local time series of DJFM NCEP surface temperature (*Kalnay et al.*, 1996). The time series of surface temperature at each grid point was normalized to unit variance before regression.

3.4.3 Dynamical Contribution to Trends in Seasonality

Northern Hemisphere 1954-2007 phase trends induced by both calendrically and orbital effects are both toward earlier seasons. Accounting for these trends in $\phi_{\text{sun}}(\theta, t)$ leads to a decrease in magnitude of the average Northern Hemisphere extratropical land phase trend from -1.77 to -1.3 days/(54 years) (P=0.001), and an increase in the magnitude of the average Northern Hemisphere extratropical ocean λ trend from 0.68 to 1.16 days/(54 years) (P=0.006). Note that the uncorrected trend distributions are different from those reported for the "dense" networks in *Stine et al.* (2009) because we are here considering only the Northern Hemisphere. Significance levels here are computed using Student's t-test, taking into account the number of spatial degrees of freedom of the field using the method described in *Stine et al.* (2009). This correction can also be seen in the visual appearance of the maps of land λ trends (compare Fig. 3.12b of this chapter to Fig. 1 of Chapter 2) which are shifted towards more positive λ trends after accounting for time variability in ϕ_{sun}. The largest visual change is seen in southern Eurasia, where a region which had weak trends towards earlier seasons (negative λ trends) becomes a region of weak positive λ trends after correction for orbital and calendrical effects are taken into account. Note that after accounting for orbital and calendrical effects the ocean λ trends are both stronger and more significant that the land λ trends.

Amplitude gain trends are both stronger and more significant than those reported in *Stine et al.* (2009), a result of limiting ourselves to the Northern Hemisphere in this study. The mean land gain trend is -2.83 $/(kW/m^2)$ per 54 years (P=0.01), a trend towards smaller amplitude seasons. The mean ocean gain trend is 0.62 $/(kW/m^2)$ per 54 years (P=0.005). The effect of accounting for the time variability of the amplitude of solar insolation forcing is small.

The contrast between the trends observed on land and the trends observed over the ocean is worth emphasizing. In both cases land and ocean trends are in the opposing directions. Land trends are toward smaller gain and earlier seasons, while ocean trends are towards larger gain and later seasons. One way to produce opposite sign trends on the land compared to on the ocean is to (seasonally) move heat from one surface cover type to the other. This suggests a deeper examination of the hypothesis that observed 1954-2007 λ and G trends are due to changes in the circulation of the Earth's atmosphere.

The large-scale circulation of the atmosphere is restricted by the constraints of geostrophy and potential vorticity conservation. Wintertime Northern Hemisphere extratropical circulation, in fact, is dominated by two modes of variability, identified by *Quadrelli and Wallace* (2004) as the first two empirical orthogonal functions (EOFs) of Northern Hemisphere sea-level pressure. The first mode corresponds to the Northern Annular Mode (*Thompson and Wallace*, 1998, 2000). *Quadrelli and Wallace* (2004) labeled the second mode PNA*, because it is similar to the classical Pacific-North-American Pattern (PNA) (*Wallace and Gutzler*, 1981). The classical PNA pattern is distinct from PNA*, but it is well represented as a linear combination of the NAM and PNA*. These two modes of circulation explain 37% of month-to-month variability in wintertime sea-level pressure with the NAM explaining about

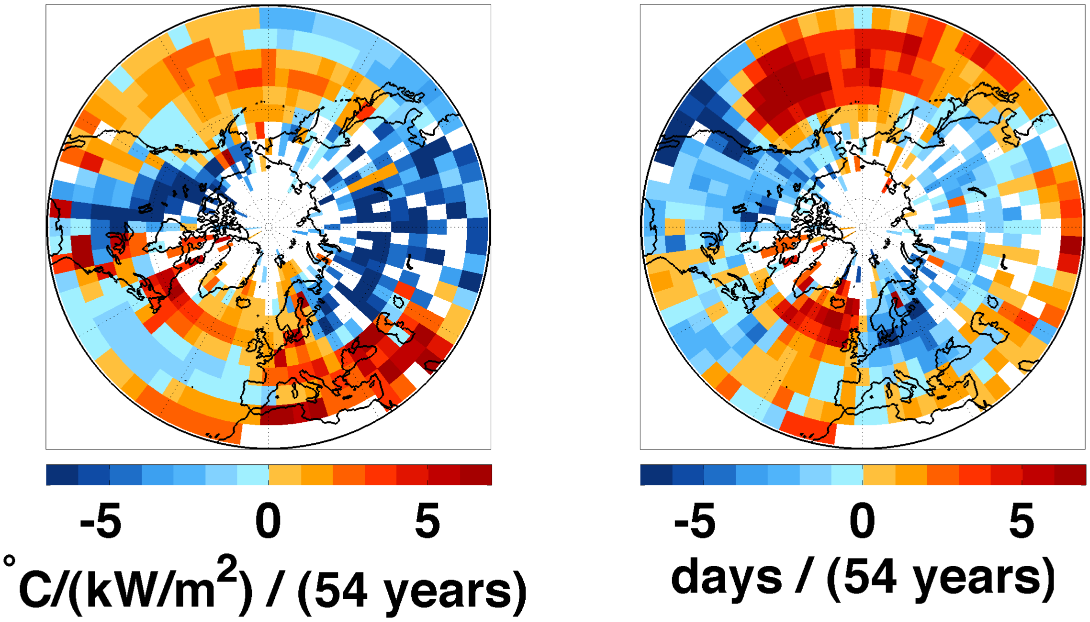

(a) Gain Trends

(b) Lag Trends

Figure 3.12. **Trends in seasonality, 1954-2007:** Linear trends in λ (left panel) and G (right panel) for 1954-2007. Trends are calculated using least-squares fits. Shown for grid boxes north of 25° N. No trend is calculated for those grid boxes where less than 40 yearly λ and G estimates were possible (white boxes).

twice the variance of the PNA. At lower frequencies, these two modes explain about half of the interannual wintertime sea-level pressure variability and virtually all of the large-scale coherent trends in wintertime sea-level variability. These, then, represent the natural modes of variability to test for dynamical control of λ and G. Because the PNA is a linear combination of the the NAM and PNA*, the same variability that is described by the combination of the NAM and PNA* can also be described by the NAM and PNA, and we choose to use the PNA index in this analysis because of its greater familiarity.

We examine the role of atmospheric circulation variability associated with the NAM and PNA in modulating the seasonality of surface temperature by correlating each of these dynamic indices separately against λ and G at each grid point of the HadCRU3 dataset. This reveals a map of spatial patterns depicting the influence of each of these modes of circulation on our seasonality parameters (Figs. 3.13 and Fig. 3.14; correlations shown are calculated using detrended time series to eliminate correlations based solely on common trends).

The striking thing to emerge from this comparison is the similarity of the loading pattern of the NAM on λ (left-hand columns of Fig. 3.13), to the pattern of their modulation of monthly wintertime temperatures (shown in the right hand columns of the same figure). When the NAM index is high, the Eastern United States, and Northern Eurasia experience earlier seasonality (more negative λ). These are the same regions where high NAM index values correspond to the strongest winter warming signal. Likewise, the two regions where high NAM index values bring the strongest winter cooling (the region extending across North Africa and the Middle East, and a region centered on the Labrador Sea extending into the North Atlantic) correspond to regions where the high NAM indices bring later seasonality (more positive λ). The sense of the correlation is that dynamical configurations that give rise to warmer winters correspond to years with earlier seasonality, and those that give rise to colder winters correspond to years with later seasonality. The same relationship between dynamically modulated wintertime temperature and seasonality timing is seen in the relationship of the PNA index and λ. When the PNA index is high, Western Canada, Alaska, and the extreme western coast of the United States experience earlier seasonality. These regions are also the locations where high index PNA values correspond to winter warmth. The two regions where high PNA index values indicate cold winter temperature anomalies (The Central North Pacific and the Eastern United States) are the regions where seasonal transitions are later (more negative λ) in high PNA index years. The region surrounding the Labrador Sea that is cold in high NAM years (Fig. 3.13a) has a much less prominent counterpart in the correlation map between λ and NAM index variability, though this may be largely due to the large amount of missing data in this region, which prevents the calculation of correlations (see Fig. 3.15 for missing correlation values mask). Significance is calculated based on the detrended time series by using the phase randomization procedure described in Chapter 2 to build a distribution under the null hypothesis of zero correlation. This approach tends to suppress false positive correlations by accounting for the autocovariance in the time series (*Schreiber and Schmitz*, 2000). Note that in the regions where NAM and PNA variability have their largest imprint on wintertime temperatures, the relationship between λ and these index values is highly significant (Fig. 3.15, left hand column). In particular, the relationship between the NAM index and λ is formally significant at >99.99% in Northern Europe, as is the relationship between the PNA and λ in Western Canada.

The pattern of correlations between G and the NAM and PNA indices (left-hand column of Fig. 3.14) also has a strong resemblance to the loading pattern of these indices on wintertime temperature (right-hand column of same figure). Regions where high NAM years indicate winter warmth are also locations where high NAM years indicate low G values (e.g. the Eastern United States, Northern Eurasia, and the Sargasso Sea). Conversely, regions where high NAM years indicate cold winters are also regions where high NAM years indicate high G values (including much of Quebec, and the Middle East). A similar relationship holds with the PNA. The region which is characterized by warm winters in high PNA years (extending from western Canada down the western coast of the United States and into the eastern edge of the Pacific Ocean) also experiences low-gain in high PNA index years. In the two regions where high PNA years indicate cold winters (the Eastern United States and the Central North Pacific), high PNA index years are high-gain years. The regions with strong dynamic modulation of wintertime temperatures also tend to be regions where the correlation between G and either NAM or PNA are highly significant (Fig. 3.15, right-hand column).

It is thus clear that the PNA and the NAM exert an important role in modulating the year-to-year variability in λ and G at many locations in the Northern Hemisphere extratropics. This raises the question of whether changes in these modes of atmospheric circulation are also responsible for the trends in λ and G. Both the NAM and PNA shifted towards more positive index values from 1954-2007 (Fig. 3.16), though in neither case is the trend statistically significantly different from zero (the 1954-2007 NAM index trend is 0.46 units/(54 years) (P=0.16), and the 1954-2007 PNA index trend is 0.31 units/(54 years) (P=0.17).

Are the trends in λ and G simply the trends that would be expected due to the fact that they are modulated by the NAM and PNA? We can test this by estimating the trends in λ that would be expected due to the trends in the NAM and PNA. At each point we regress local λ simultaneously against the hemispheric NAM and PNA indices. We remove the trend from the local λ and NAM and PNA indices before calculating the regression coefficient in order to decrease the chance of finding spurious relationships and to avoid biasing the correction towards variance reduction. We then multiply the regression coefficients (calculated from the detrended time series) by the NAM and PNA index trends in order to find the local λ trend predicted by the relationship with these two dynamic indices. This is the dynamical correction to the local λ trend. At each point we subtract this value to obtain the "corrected" λ trend. We apply an analogous procedure to obtain "corrected" G trends at each grid point.

We evaluate whether the observed λ and G trends are explained by changes in atmospheric circulation described by NAM and PNA variability by comparing the distribution of observed trends with the corresponding distribution of "corrected" trends, separating land and ocean (Fig. 3.17). We find that the λ_{land} trend can, in fact, be explained by atmospheric dynamics. The mean of the distribution of observed 1954-2007 λ_{land} trends is -1.3 days/54 years (P=0.001), a trend towards earlier seasonality. The dynamic correction decreases the mean λ_{land} trend by 63%. The residual distribution has a mean of -0.47 days/54

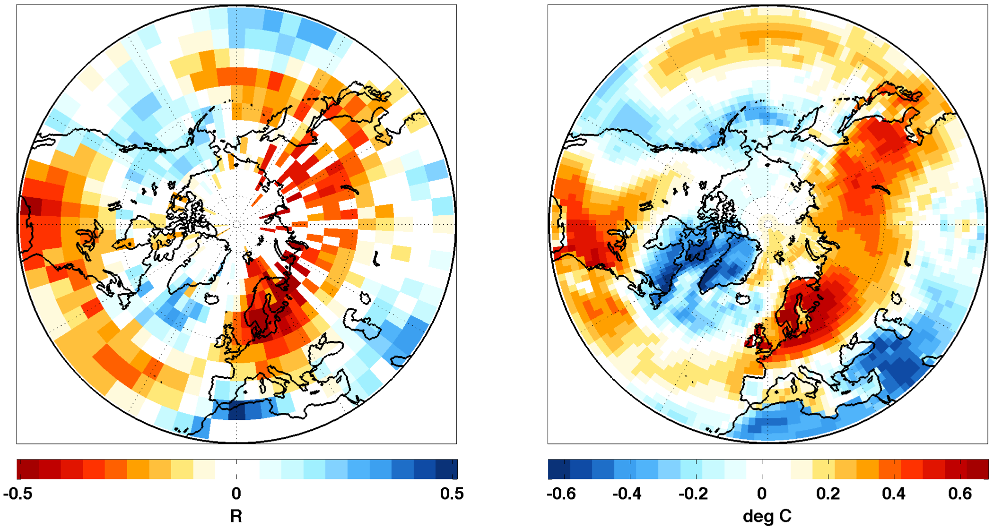

(a) Correlations between NAM and lag (λ) (b) NAM winter loading pattern

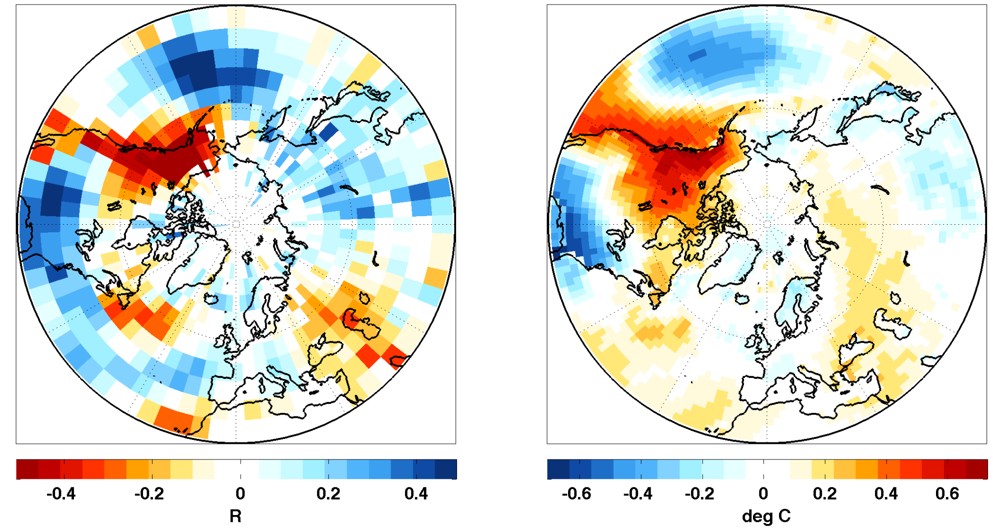

(c) Correlations between PNA and lag (λ) (d) PNA winter loading pattern

Figure 3.13. **Effect of wintertime dynamics on λ variability.** Spatial pattern of the imprint of NAM and PNA variability on λ is strikingly similar to their imprint on mean wintertime temperatures. **(Left Column):** Maps of correlation between pointwise variability in λ and the hemispheric indices of the NAM (upper left) and the PNA (lower left). Correlations calculated after removing trends from each time series, and expressed as Pearson's R correlation coefficient. **(Right Column):** Maps of winter loading pattern of the NAM (upper right) and PNA (lower right) on wintertime (DJFM) surface temperatures calculated by regressing wintertime monthly values of each hemispheric index onto pointwise NCEP reanalysis surface temperature time series (*Kalnay et al.*, 1996), each normalized to unit variance. Note strong similarity between the dynamical variability as expressed in λ (left) and in mean wintertime temperature (right).

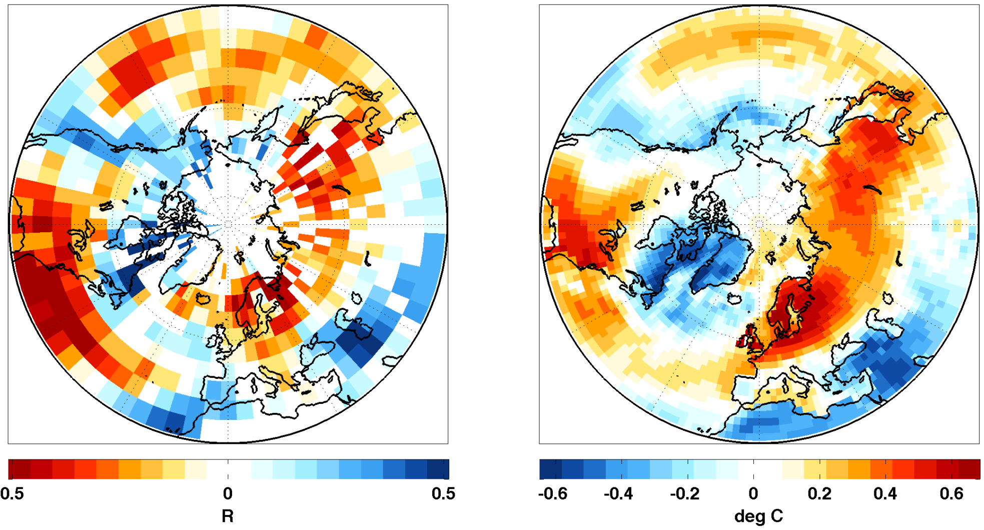

(a) Correlations between NAM and gain (G)

(b) NAM winter loading pattern

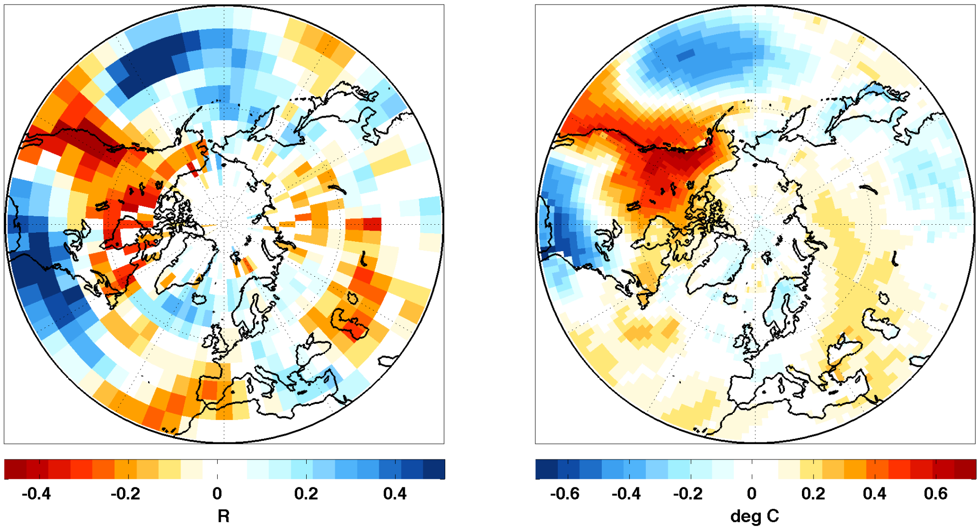

(c) Correlations between PNA and gain (G)

(d) PNA winter loading pattern

Figure 3.14. **Effect of wintertime dynamics on G variability.** Same as 3.13, but for G instead of λ.

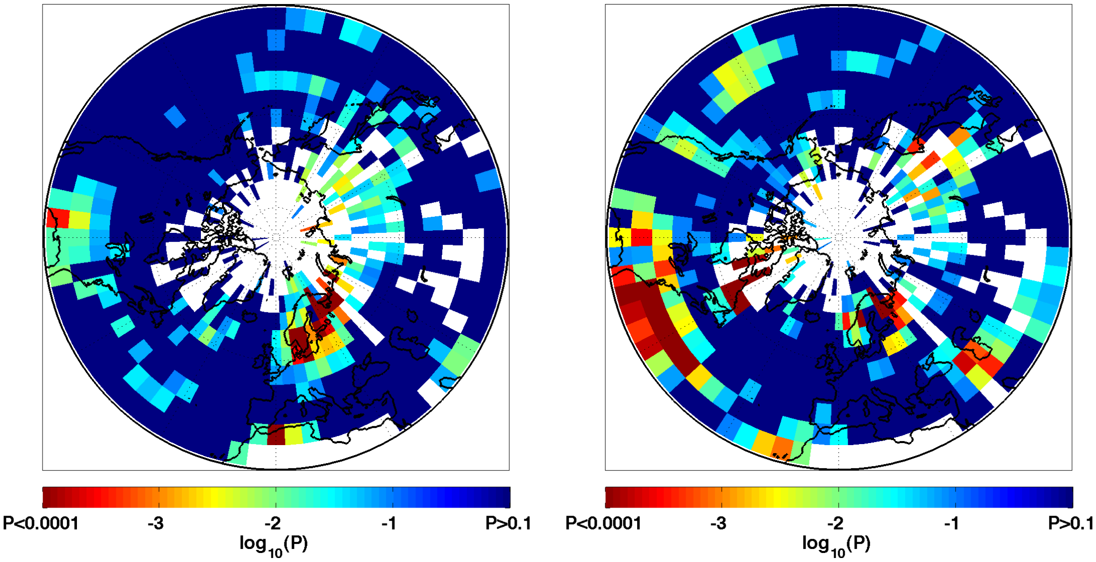

(a) NAM vs. λ correlation significance (b) NAM vs. G correlation significance

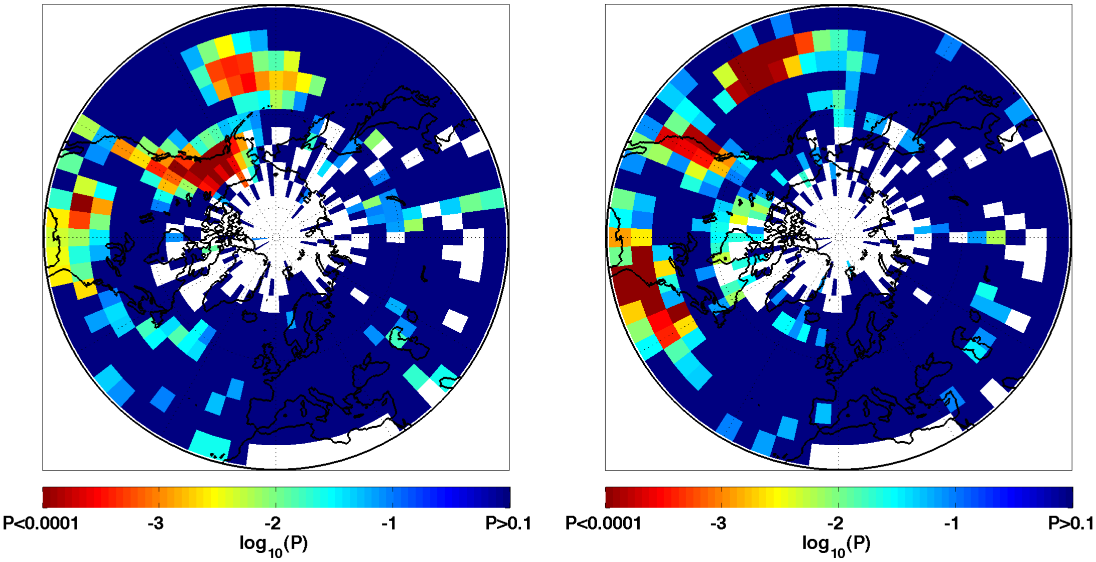

(c) PNA vs. λ correlation significance (d) PNA vs. G correlation significance

Figure 3.15. **Significance of relationship between wintertime dynamics and seasonality.** P-values of the correlations between wintertime dynamics (as represented by NAM and PNA indices) and seasonality (λ and G). These represent the significance of the correlation maps in Figs. 3.13 & 3.14. The color scale is logarithmic to emphasize how significant regional correlations are. All P-values > 0.1 are set to 1 in the color scale (dark blue) to allow clear visual separation between regions of high and low significance. P-values that are less than 0.001 were set to 0.001. P-values are calculated taking into account the full spectral structure of the time series, as described in text. White regions are those with insufficient data to calculate correlation.

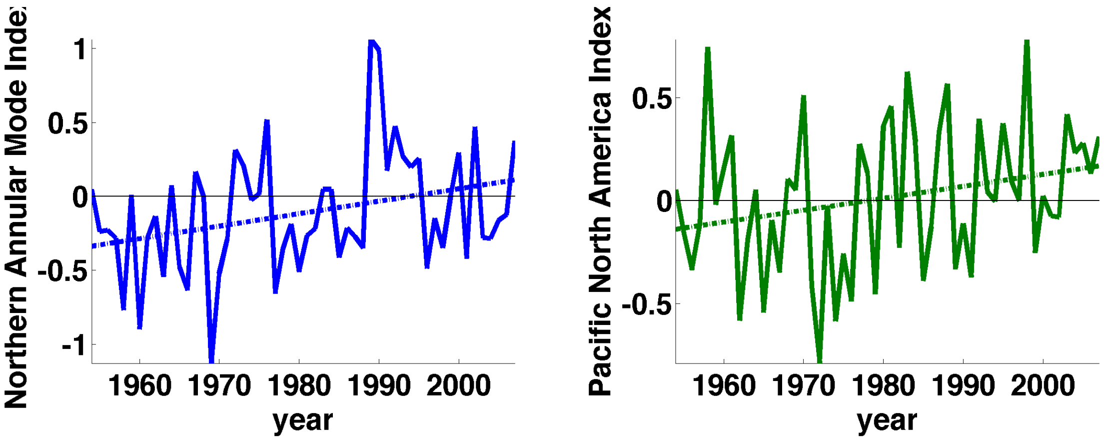

(a) Northern Annular Mode (NAM) index (b) Pacific-North America (PNA) index

Figure 3.16. **Dynamical indices.** Time Series of annual mean indices of the Northern Annular Mode (left panel) and the Pacific North-American index used in this analysis. Dashed lines give linear trend from 1954-2007.

years (P=0.2), which is not significantly non-zero. The dynamic correction also decreases the width of the distribution of pointwise trends (the variance of the distribution decreases by 13%), indicating that the detrended relationship between λ_{land} and the first two modes of atmospheric circulation predicts the observed trend in both regions with positive and negative phase lag trends. Removal of the dynamically-predicted gain trends decreases the mean distribution of 1954-2007 G_{land} trend by 37%, from the highly significant value of -2.83 $/(kWm^2)/(54years)$ (P=0.01) to the marginally significant -1.79 $/(kWm^2)/(54years)$ (P=0.06), and decreases the variance of the distribution by 21%. The ability of dynamical effects to explain trends over the ocean is more ambiguous. Applying the dynamical correction decreases the mean of the distribution of λ_{ocean} by 9% (from 1.16 to 1.05 days/(54 years)), but increases the significance of the this value because of the narrowing of the distribution (a 36% varience reduction). The dynamical correction to $\mathsf{G}_{\text{ocean}}$ has little effect on the mean of the distribution (it causes a slight increase in the magnitude of the trend), but it also increases the significance of the trend, primarily due to the narrowing of the distribution (a 16% decrease in variance).

3.4.4 Implications of Dynamical Control

The observed 1954-2007 trends in phase of the annual cycle of surface temperature on land are explained by the cumulative effects of orbital changes, aliases of the tropical year due to sampling of temperature on the Gregorian calendar and changes in atmospheric circulation described by the Northern Annular Mode and the Pacific North America Pattern. These effects also appear to explain the contemporaneous amplitude gain trends, though this is less

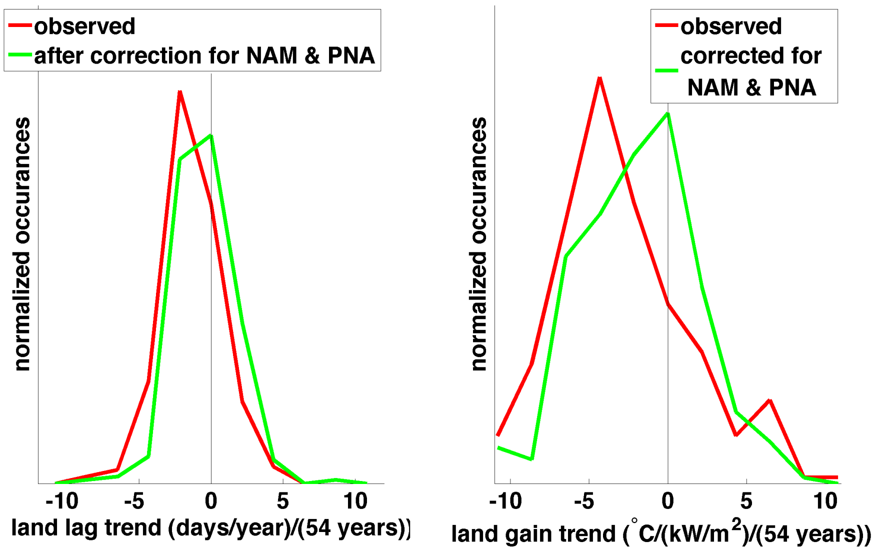

(a) distribution of λ_{land} trends (b) distribution of G_{land} trends

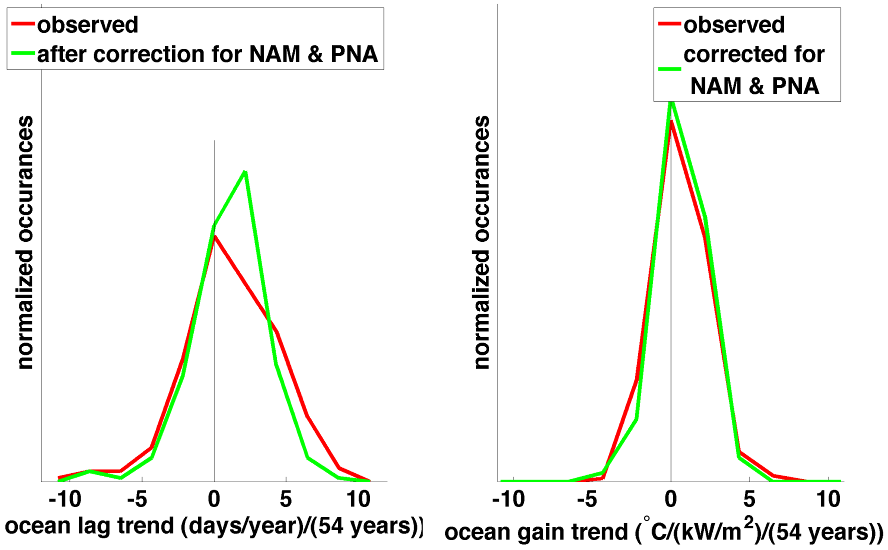

(c) distribution of λ_{ocean} trends (d) distribution of $\mathsf{G}_{\text{ocean}}$ trends

Figure 3.17. **Distribution of 1954-2007 trends in seasonality before and after correction atmospheric dynamics. (upper left:)** Histogram of 1954-2007 λ_{land} trends for Northern Hemisphere extratropical CRUTEM3 grid boxes. Red line is observed distribution. Green line is distribution after removing linear response to NAM and PNA trends. **(upper right):** same but for G_{land}(using CRUTEM3 dataset). **(lower left):** same but for λ_{ocean}(using HadSST2 dataset). **(lower right):** same, but for $\mathsf{G}_{\text{ocean}}$(using HadSST2 dataset).

Table 3.2. **Table of trends, means, variances, pvals, and effect of dynamical corrections:** Trends in the average lag (λ) and gain (G) separately over Northern Hemisphere land and ocean. **First row** is raw trends calculated relative to the Gregorian calendar. These differ from the values in Chapter 2 (*Stine et al.*, 2009), because in this chapter we consider only Northern Hemisphere locations in our spatial average. **Second row** is these same trends after correction for orbital and calendrical drift. **Third row** is the inferred trend in each variable due to dynamical effects. **Last row** is the the residual trend in each variable after correction for orbitally-, calendrically- and dynamically-induced trends.

	land lag (λ_{land})	ocean lag (λ_{ocean})	land gain (G_{land})	ocean gain ($\mathsf{G}_{\text{ocean}}$)
Trend on Gregorian calendar	-1.77 ($P<0.001$)	+0.68 ($P=0.1$)	-2.83 ($P=0.01$)	+0.62 ($P=0.005$)
Corrected for $\phi_{\text{sun}}(\theta, t)$ & $A_{\text{sun}}(\theta, t)$	-1.3 ($P=0.001$)	+1.16 ($P=0.006$)	-2.83 ($P=0.01$)	+0.62 ($P=0.005$)
Dynamical Trend	-0.82	+0.11	-1.04	-0.04
Corrected for orbit, calendar and dynamics	-0.47 ($P=0.17$)	+1.05 ($P=0.002$)	-1.79 ($P=0.06$)	0.65 ($P=0.001$)

unambiguous. Ocean trends, in contrast, appear more significant after taking into account natural sources of variability.

The modulation of amplitude gain by the dominant modes of wintertime circulation is perhaps not surprising. The amplitude of the annual cycle is controlled by the difference between summer and winter temperature. Modes of circulation that increase wintertime temperature directly decrease G, and vice-versa. It is therefore surprising that these dynamical modes of circulation explain the trends in λ_{land} so much better than they explain the trends in G_{land}. It is not, a priori, clear why any relationship should exist between annual mean NAM and PNA index variability and the land lag signature – no attempt was made to capture a signature associated with timing of seasonality in the derivation of the spatial loading pattern associated with these modes. The dynamical modes of atmospheric circulation (NAM and PNA*) are derived as the EOFs of the monthly mean sea-level pressure record – a procedure that produces the identical spatial pattern even if the order of timesteps is randomly shuffled before analysis (provided the same shuffling is done identically at each spatial location).

The sense of the relationship between dynamical variability and temperature seasonality is that dynamical changes which (locally) produce warmer winters produce earlier seasonal transitions, and those changes that produce colder winters produce later seasonal transitions.

However, a temperature perturbation that simply lowers winter temperature with no other effect on the annual cycle would have no effect on λ. Thus the relationship between dynamical winter temperature anomalies and λ_{land} seems to indicate either a consistent asymmetry in the expression of circulation anomalies associated with both the NAM and PNA about midwinter, or an asymmetry in how those circulation anomalies manifest themselves as temperature anomalies. This is a distinction that will be difficult to sort out, but we can make some inferences based simply on the strong correspondence between the correlation pattern of the λ and each of our dynamical indices and the spatial pattern of the NAM projection onto wintertime temperatures. We see a correspondence in these patterns at both high latitudes and low latitudes, and in both wet areas and dry areas. The mechanism by which circulation anomalies produce asymmetry in the temperature response is thus unlikely to be due purely to snow albedo effects which will only be active at high latitudes or soil moisture effects which will only exist on land and be very different in wet and arid regions.

Temperature anomalies associated with both the NAM and PNA arise, in large part, due to circulation anomalies which produce temperature anomalies by advecting air across the strong winter pole-to-equator temperature gradient. Thus seasonal variation in this gradient provide a potential source of asymmetry in the the temperature response to circulation.

An alternative hypothesis is that the seasonal asymmetry in temperature anomalies associated with locally warm or cold winters is due to seasonal asymmetries in circulation, which manifest themselves in both the interannual variability and the long-term trends.

The strong signal of atmospheric dynamical variability in the modulating land phase suggests that skillful forecasts of the timing of seasonal transitions are likely possible. Because of the importance of seasonal prediction for agriculture and industry, much work has been done on predictability of the Northern Annual Mode, with the aim of predicting wintertime temperatures, and some skill has been demonstrated (*Cohen et al.*, 2002; *Cohen and Entekhabi*, 1999; *Cohen et al.*, 2001). The results presented here suggest that we may be able to borrow this established skill in order to predict the timing of seasonal transitions, a problem with societal implications at least as important as prediction of wintertime temperature.

Chapter 4

Changes in the Function of the Terrestrial Biosphere as Manifest in the Annual Cycle of Atmospheric Carbon Dioxide

Changes in the terrestrial biosphere's large-scale carbon cycling have been diagnosed from temporal variability in the seasonal cycle of atmospheric CO_2. Trends in the annual amplitude (A), timing of annual carbon draw-down (t_{drop}), and timing of annual carbon rise (t_{rise}) have been used to argue for a more photosynthetically active terrestrial biosphere, earlier initiation of spring, and increased terrestrial respiration in autumn respectively. We examine the Mauna Loa (1958-2008) and Barrow (1971-2008) CO_2 records which represent the longest Northern Hemisphere low- and high-latitude records respectively, and find that *(1)* A trends at both locations are significant and anomalous when compared with a model of natural variability, *(2)* t_{rise} trends are significant and anomalous at Mauna Loa, but not at Barrow, *(3)* the magnitude of t_{drop} trends are consistent with natural variability at both Mauna Loa and Barrow. Examination of the larger network of CO_2 observations and a coupled General Circulation Model with a fully coupled carbon cycle model shows that A variability is spatially correlated across the Arctic, throughout the remote Northern Hemisphere mid-to-low latitudes, and through the Antarctic and the Southern Ocean. t_{rise}

and t_{drop} are correlated over more limited geographic regions. Amplitude variability is associated with temperature variability at high northern latitudes, and with drought in mid-to-low northern latitudes.

Figure 4.1. **Atmospheric carbon dioxide sampling at Summit Camp, Greenland:** Summit Camp is at the highest point on the Greenland ice sheet. The subtle contrast in color between the top quarter of image and the remainder of image is the horizon. Photo by Sonja Wolter.

4.1 Terrestrial Biosphere Variability Inferred from the Annual Cycle of Atmospheric CO_2

The annual rhythm of rise and fall of atmospheric CO_2 concentrations records the growth of the terrestrial biosphere in summer and its decay in the fall and winter (*Keeling*, 1960; *Fung et al.*, 1983). As temperatures increase, changes are expected in the terrestrial biosphere which will alter its carbon cycling (*Fung et al.*, 2005; *Friedlingstein et al.*, 2006; *Peñuelas and Filella*, 2001; *Cox et al.*, 2000; *Cao and Woodward*, 1998) and indeed, changes in the annual cycle of atmospheric CO_2 have been interpreted as a response to climate change (*Piao et al.*, 2008). Interpretation of observed annual-period variability in atmospheric CO_2

concentrations is complicated by the fact that we have no record of the annual cycle of atmospheric CO_2 that does not contain a human imprint. Observations of atmospheric carbon dioxide concentrations begin in the period when anthropogenic activity has already begun to exert a significant impact on the carbon cycle. The anthropogenic trend in atmospheric CO_2 concentrations is already clear in the first few years of Keeling's measurements of CO_2 in Antarctica and atop Mauna Loa (*Keeling*, 1960; *Pales and Keeling*, 1965). The human imprint on the carbon cycle at that point cannot have been limited to the insertion of fossil carbon into the atmosphere. If that were the only human influence on the carbon cycle in the 1960s, then the airborne fraction (the ratio of the observed rate of change of total atmospheric carbon to the rate of fossil carbon injection into the atmosphere) would be 1 (*Stuiver*, 1978). Instead, the atmospheric rate of CO_2 increase was (and continues to be) only about half the rate of fossil carbon injection by industrial activities. Thus, changes in the exchanges of carbon between atmosphere and either the ocean or the terrestrial biosphere were necessarily already underway. This creates difficulty in the interpretation of variability in CO_2 seasonality – a difficulty which was less of an issue in our analysis of surface temperature for which we possessed a much longer and denser observational network. We have only a handful of atmospheric CO_2 records, and we have no period that we can reasonably treat as an instance of natural variability.

Most of the long atmospheric CO_2 records are positioned away from local sources and sinks of carbon to the atmosphere in order to sample large-scale processes. Atmospheric mixing tends to smooth out the effect of surface fluxes over space, integrating the surface fluxes over large scales. Mauna Loa is particularly well placed to measure the average Northern Hemisphere signal. Mauna Loa CO_2 concentrations drop rapidly from May to September with the arrival of spring as new plant growth removes carbon from the atmosphere, and increase gradually through the cold season from September to May, as the carbon from dead plants and fallen leaves slowly decomposes and returns to the atmosphere. Strictly speaking, the atmospheric CO_2 record contains a record of land, ocean and fossil carbon fluxes. However, annual timescale variability is dominantly the result of terrestrial carbon variability. Atmospheric measurements of $^{13}CO_2$ (*Keeling*, 1961), and modelling studies (*Doney et al.*, 2006, and see Chapter 1) indicate that the dominate source of variability in the annual cycle of atmospheric carbon dioxide is terrestrial processes. Fossil carbon has a terrestrial ^{13}C signature and can therefore not be distinguished from terrestrial carbon by ^{13}C analysis. (Fossil carbon once was, after all, plant matter.) However, budget calculations indicate the fossil contribution to the annual cycle in remote well-mixed air is quite small when compared with the that due to annual carbon cycling of the terrestrial biosphere. Gross annual terrestrial photosynthetic fluxes are estimated to be of the order of $\sim$100 petagrams of carbon (Pg C) per year (*Leith*, 1975). The annual cycle in fossil fuel emission has been estimated to have an amplitude of $\sim$0.02 Pg C (*Blasing et al.*, 2005) for the United States, though atmospheric methods have inferred a much larger annual cycle (*Levin et al.*, 1995; *Randerson et al.*, 1997). If we assume that this relative magnitude is representative of the world, we infer a global annual cycle of 0.1 Pg C, which is likely to be an overestimate because the seasonality of emissions will vary spatially leading to some cancellation. This is three orders of magnitude smaller than the annual cycle in terrestrial biosphere fluxes.

A literature exists which explains changes in the structure of atmospheric CO_2 at Mauna Loa as arising from changes in the carbon cycling of the terrestrial biosphere. *Pearman and Hyson* (1981) found trends towards increased annual cycle amplitudes at Mauna Loa, Barrow, and Weathership P in the north Pacific, and estimated a 1958-1978 amplitude trend at Mauna Loa of +0.45%/year. *Keeling et al.* (1996) observed a 20% increase in the amplitude (~0.6%/year), and an advance toward earlier carbon draw-down of by 7 days at Mauna Loa from 1960-1993, which he interpreted as an indication of increased Northern Hemisphere productivity and a lengthening of the growing season. *Buermann et al.* (2007) identified a reversal of the trend toward increased amplitude at Mauna Loa beginning in the early 1990s which they attributed to severe Northern Hemisphere droughts from 1998-2003. *Piao et al.* (2008) identified widespread trends toward earlier autumn increases in atmospheric carbon dioxide concentrations (as measured by the time the local CO_2 record crosses its trend-line in autumn), which they attributed to temperature-modulated increases in autumn respiration. They gave the most attention to the trend at Barrow, Alaska, but the three locations with the strongest trends were all Hawaiian islands (Midway, Cape Kumukahi, and Mauna Loa).

Our goal in this chapter is to establish which metrics of variability in seasonality are representative of large-scale changes in the annual exchange of carbon between the atmosphere and the surface. We separately consider the three metrics for changes in the seasonality of atmospheric carbon dioxide (defined in section 4.2) that have been used to argue for large-scale changes in the terrestrial biosphere's carbon cycling, *viz.*: amplitude of the annual cycle (*Pearman and Hyson*, 1981; *Keeling et al.*, 1996; *Buermann et al.*, 2007), the timing of the upward trend-line crossing in autumn (*Piao et al.*, 2008), and the timing of the downward trend-line crossing in spring (*Keeling et al.*, 1996). Our focus is on two observational records of atmospheric carbon dioxide: the 1958-2008 Mauna Loa record and the 1971-2008 Point Barrow record which represent our longest monthly resolution records low- and high-latitude Northern Hemisphere records respectively. For each of these two records, we ask three questions: *(1)* Do significant trends exist in our seasonality metrics over all or part of the observational record? *(2)* Are the observed trends anomalous when compared with natural variability? and *(3)* Is the local variability in each seasonality metric indicative of large-scale variability? The first question is a simple statistical question. The question of the relationship of the observed trends to natural variability is more difficult because we have no record of the annual cycle of atmospheric CO_2 before substantial human influence on atmospheric CO_2 concentrations began. We therefore turn to a numerical model to estimate natural variability. These first two questions are addressed for Mauna Loa in section 4.3 and for Barrow in section 4.4. We apply a variety of approaches to evaluate the spatial representativeness of each seasonality metric. We begin by examining the climatological distribution of each metric, across the entire surface observational network, in order to identify the large-scale spatial context, noting some similarities and differences between the climatology in the surface network and climatological estimates of CO_2 seasonality made from satellite observations (Section 4.5.1). We then evaluate the spatial scale over which the temporal variability of each seasonality metric is representative (Section 4.5.2) using a model and observations. Finally, we ask what implications our results have for interpretation of observed changes in the seasonality of atmospheric CO_2 (Section 4.6).

4.2 Estimation of Phase and Amplitude

Observational discussions of the phase of the annual cycle of atmospheric carbon dioxide have separated discussion of the timing of seasonal transitions in the spring and fall (*Keeling et al.*, 1996; *Piao et al.*, 2008). The motivation for this separation is that the annual cycle of carbon dioxide at most locations is highly skewed, and the spring and fall transition timings are controlled by quite different processes.

Conceptually, estimates of timing of spring carbon draw-down and autumn carbon release are attempting to identify the time that the curve would cross zero if there were no trend. However, especially in the later record, the trend in atmospheric CO_2 dominates the variability. Thus removal of the trend is not a minor correction. This is in contrast to the temperature record, where removal of the trend has almost no effect on estimates of seasonality. Starting with the observation that the annual cycle has a saw-toothed structure which is well described by a frequency modulated sine wave, we model the atmospheric annual cycle in CO_2 as:

$$y = A\cos\left(2\pi ft - \phi + B\cos\left(2\pi ft - \phi - \psi\right)\right) + Ct + \mu \tag{4.1}$$

where,
A is the amplitude of the annual cycle, f is the frequency of the annual cycle (1/365.24 cycles per day), t is time, given in days,
ϕ represents the mean phase of the annual cycle
$B\ \cos\left(2\pi t - \phi - \psi\right)$ represents phase modulation of the annual cycle of magnitude B and with a phase offset of ψ relative to ϕ, and
$Ct + \mu$ represent the trend and the mean CO_2 concentration.

We estimate the spring and fall trend-line crossings (often referred to as zero-crossing time, despite the fact that concentrations never cross zero) as the times when the detrended and demeaned model fit ($A\cos\left(2\pi t - \phi + B\cos\left(2\pi t - \phi - \psi\right)\right)$) crosses zero. The time of the autumn upward trend-line crossing can be approximated as the upward trend-line crossing time of an unmodulated sine wave with phase ϕ (the first parenthetical on the right-hand side of Eqn. 4.2), plus a correction equivalent to the temporal offset due to phase modulation of the full model at the time of the upward trend-line crossing of the unmodulated model. The time of the autumn upward trend-line crossing is then given by:

$$2\pi ft_{\text{rise}} = \left(\phi - \frac{\pi}{2}\right) - B\cos\left(-\psi - \frac{\pi}{2}\right) \tag{4.2}$$

This result can be obtained by setting the argument of the first cosine term in Eqn. 4.1 equal to $-\frac{\pi}{2}$ (the angle at which cosine returns zero and has a positive first derivative), approximating the $2\pi ft$ term inside the second cosine term using the time of upward trend-line crossing of the unmodulated sine wave, *viz.* $\phi - \frac{\pi}{2}$. The phase of spring downward trend-line crossing is likewise approximated as the downward trend-line crossing time of an unmodulated sine wave with phase ϕ, plus the temporal offset due to phase modulation of the full model at the downward trend-line crossing time of the unmodulated sine wave. The time of spring downward trend-line crossing is then given by:

$$2\pi f t_{\text{drop}} = \left(\phi + \frac{\pi}{2}\right) - B\cos\left(-\psi + \frac{\pi}{2}\right) \tag{4.3}$$

For finite-length record pieces, estimates of the trend and of the variability about the trend are not independent in this non-linear model. For example, if we generate a time series by setting C and μ to zero, but $B \neq 0, \psi \neq 0$, then a least-squared linear trend analysis will give a non-zero trend, due to the asymmetry of the phase-modulation, despite the fact that we have produced the the record with the trend term set to zero. We deal with this by simultaneously estimating the trend and variability about the trend and by fitting the model to 5-year record pieces, which reduces the tendency to infer spurious trends. We use an iterative approach to fit the non-linear model given in Eqn. 4.1 to monthly observations of atmospheric CO_2 in five-year increments. In this approach we obtain a first estimate for C and μ using a least-squared linear trend estimate. We then alternate between holding the phase modulation terms constant (B, ψ) and fitting the phase, amplitude and trend terms (ϕ, A, C, μ), then holding the phase amplitude and trend terms fixed and allowing the phase modulation terms to vary to improve the model fit. In each step we adjust the fitting variables using the Nelder-Mean unconstrained nonlinear minimization scheme. We require 50 of the 60 monthly data points to be present or we make no attempt to fit the given 5-year segment. We associate the fit of each 5-year record period with the center year. This means that the first two years of data (and the last two years of data) will have no fit associated with them, even if we have CO_2 measurements from all 12 months. Due to data gaps in the first year of observations at Barrow we obtain no estimates of seasonality for the first three years, rather than just the first two years. Thus we obtain seasonality estimates for Mauna Loa only from 1960-2006, despite data coverage from 1958-2008, and we obtain estimates of Barrow seasonality only from 1974-2006. We consider only those stations where Eqn. 4.1 explains >60% of the variance of the average 5-year record segment. For the Antarctic/Southern Ocean, we relax this requirement to 50% to allow us to consider Cape Grim, Baring Head and Jubany, Antarctica. For the AIRS data, we likewise consider grid points where the model explains >50% of the variance.

We use monthly surface CO_2 observations from World Data Centre for Greenhouse Gases (WDCGG) contributed from more than 20 agencies from around the world (*WDCGG*, 2009), and the Scripps Institution of Oceanography CO_2 Program (*Keeling et al.*, 2001). Where more than one record exists for a single location, we choose the longest record for analysis, except in Fig. 4.8 where our goal is to compare different estimates from the same location. We also analyze the latitudinal gradient in seasonality using the Atmospheric Infrared Sounder (AIRS) experimental L3 CO_2 gridded data set (*Chahine et al.*, 2008).

We estimate the significance of trends using the phase randomization technique described in Chapter 2 (*Stine et al.*, 2009) that takes into account the full internal autocorrelation structure of a time series.

4.3 Changes in Seasonality at Mauna Loa

Evaluating the importance of observed changes in the annual cycle of atmospheric carbon dioxide involves asking two questions. First, is there a significant trend? It has been some time since some of these trends have been visited, and previously reported trends may have accelerated or have disappeared. Second, are these trends anomalous when compared with natural variability? We are not in possession of a record of pre-anthropogenic variability of atmospheric carbon dioxide with seasonal resolution, nor are we likely to ever possess one. Ice core CO_2 records give a record of natural variability at annual resolution at best. Instead we estimate natural variability using a general circulation model with a fully-coupled land, ocean, and atmospheric carbon cycle (*Doney et al.*, 2006). This model is based on the framework of the Community Climate System Model project (*Blackmon et al.*, 2001). We consider the 1000-year control simulation of *Doney et al.* (2006) as an estimate of the range of variability in the annual cycle of atmospheric CO_2 indicative of natural variability.

The Mauna Loa amplitude time series is dominated by a jump in the 1970s and early 1980s, after which the observed amplitude has varied about 3.2 ppmv (Fig. 4.2b). We observe the decrease in amplitude reported by *Buermann et al.* (2007) in the drought years centered on the year 2000, but our updated analysis finds that this dip in amplitude proceeded to recover in the late 2000s. This gives a highly significant trend of 0.566 ppmv per 47 years ($P<0.001$) – a 20% increase in amplitude over the course of the record. A direct comparison of this trend against model variability is complicated by the fact that the pole-to-equator gradient in climatological amplitude is weaker in the model than it is in the observations, which appears to be due to an underestimate of productivity in the model at high northern latitudes (*Doney et al.*, 2006). The simulated amplitude of the annual cycle at Mauna Loa is 40% smaller than the observed amplitude (1.9 vs 3.1 ppmv). To the extent that amplitude variability scales with mean amplitude (i.e. large amplitude stations have greater amplitude variability – a relationship we observe in the flask network), we expect the model to underestimate amplitude variability and to over-diagnose anomalous trends. We correct for this by rescaling the modelled Mauna Loa amplitude time series by the ratio of the observed climatological amplitude to the modelled climatological amplitude. This gives a 1000-year modelled time series of Mauna Loa amplitude with a mean of 3.1 ppmv and a standard deviation of 0.1 ppmv. The 1000-year model simulation can be broken up into 950 distinct 47-year periods, though this represents only 21 independent segments. The magnitude of the observed 1960-2006 Mauna Loa amplitude trend is 40% bigger than even the largest of the simulated trends. The model result thus indicates that the observed 1960-2006 Mauna Loa amplitude trend is inconsistent with natural variability (see Table 4.1).

Changes in the time of autumn upward trend-line crossing (here "rise-time") were first reported by *Piao et al.* (2008), who focused on changes at high latitudes. However, of all of the stations he considered, the three locations with the strongest trends were all Hawaiian islands (Midway, Cape Kumukahi, and Mauna Loa). Consistent with this result, we find strong trends toward earlier rise-day at Mauna Loa (Fig. 4.2c), with a magnitude of 12.1 days per 47 years ($P<0.01$), the strongest of any of the trends in timing. This is equivalent

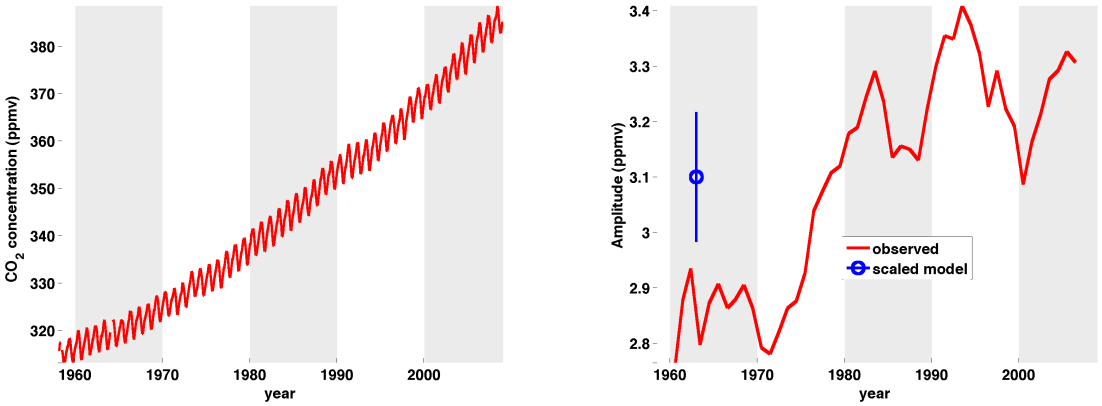

(a) Mauna Loa CO$_2$ time series

(b) Mauna Loa amplitude (A)

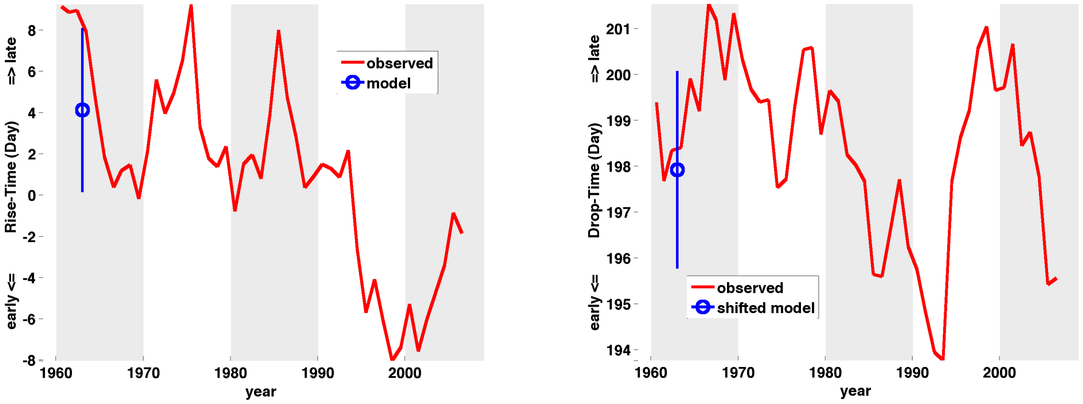

(c) Mauna Loa rise-day (t_{rise})

(d) Mauna Loa drop-day (t_{drop})

Figure 4.2. **Mauna Loa seasonality:** Temporal variability of seasonality at Mauna Loa from Scripps Institution of Oceanography (SIO) monthly averaged continuous observations. **(a)** Monthly observations from 1958-2008. Note periods of missing values at beginning of record. **(b)** Red line is amplitude (A) time series obtained by fitting Eqn. 4.1 to monthly data shown in (a). The blue circle represents the mean amplitude of the natural variability model. Because the model time series has been rescaled this is by definition equal to the observed long-term-mean amplitude. Blue line shows ± one standard deviation of CO$_2$ concentrations variability in the grid box corresponding to Mauna Loa from the model of *Doney et al.* (2006), after the time series has been rescaled to have the same long-term-mean amplitude as the observations. **(c)** same as (b), but for rise-time (t_{rise}). The model t_{rise} is similar to the observed pre-1990 t_{rise} in both its mean and its variance (blue line is *not* rescaled or shifted). Day zero represents January 15th. **(d)** same as (b), but for drop-time (t_{drop}). Mean model estimate t_{drop} is shifted up by 12 days so it is in same range as observation. The variance of the model variability has *not* been adjusted. Day 200 represents August 2nd.

to 0.26 days/year – much weaker than *Piao et al.'s* result of a 1980-2002 t_{rise} trend of 0.75 days/year which coincided with the largest transition in the record (Fig. 4.2c). This change is characterized by a shift in the mean around 1990. Before 1990 t_{rise} oscillates about January 19th, while after 1990 variability is about January 10th Unlike the amplitude case, no correction to the model time series is necessary in order to compare the observed trend to natural variability (as represented in the model). Both the long-term-average model simulated t_{rise}, and the modelled standard deviation of this quantity are consistent with the pre-1990 observations (Fig. 4.2c). We again compare the observed trend to the collection of simulated 47-year trends and find that only one of the 950 simulated ϕ_{rise} trends exceeds the observed trend. The model result is that the observed 1960-2006 Mauna Loa t_{rise} trend is of a magnitude which occurs naturally, but only once in 1000 years, and the observed trend is thus unlikely to be attributable to natural variability (P=0.001).

Shifts in the time of spring downward trend-line crossing (here "drop-time", t_{drop}) toward earlier seasonality by ~7 days were reported by *Keeling et al.* (1996) using data from 1958 to 1994, which were interpreted as an indication of lengthening of the growing season. By extending the record through 2006, we find that the excursion of drop-time noted by *Keeling et al.* (1996) completely recovered in the late 1990s and remained at values typical of the early record (i.e. t_{rise} times around August 5th) until 2004, when the timing of spring carbon draw-down again began to shift toward earlier in the season (Fig. 4.2d). This recovery of the Mauna Loa t_{drop} appears coincident in time with the dip in amplitudes noted by *Buermann et al.* (2007) and may be a manifestation of the large-scale Northern Hemisphere drought which was strongest in the early 2000s. When we consider the updated record we find that the trend is much weaker than reported by *Keeling et al.* (1996) (-2.4 days/(47 years)), and is not significant (P=0.3). We compare this trend to the collection of simulated 47-year drop-day trends in the 1000-year model simulation and find that 25% the modelled 47-year record periods contain trends of greater magnitude than the observed 47-year drop-day trend (see Table 4.1). The model indicates that t_{drop} trends of the magnitude observed are commonplace, and are consistent with natural variability.

A subtler question is whether the t_{drop} trend in the early part of the record (and reported by *Keeling et al.* (1996)) is indicative of the terrestrial carbon cycle behaving in a manner inconsistent with natural variability (as represented by the model). Here we need to be careful to avoid biasing our conclusion. A simple way to pose the question is to observe that there is a strong trend from 1966 (the maximum value of the time series) to 1993 (the minimum value of the time series), and to ask if this 28-year trend is anomalous when compared with our model of natural variability. We can test this by comparing the largest magnitude 28-year trend in the observed 47-year record to the distribution of maximum 28-year trends in each of the 47-year records in our model simulation. We find that the observed maximum 28-year trend is larger in magnitude than 93% of the 950 simulated maximum 28-year trends, which gives a marginally significant result (P=0.07). However, this approach is biased toward false positives (falsely identifying behavior as inconsistent with natural variability) because we decided to pick 28 years as our record-length of interest after looking at the data and noting the record length with the strongest trend. If we had, instead, observed a strong 40-year trend we would have instead used 40 years as our test period. To properly account for this bias of looking for trends over the record length in which we observe the strongest trends, we explicitly take into account the fact that we have focused on the time period with the strongest trend in the record. We build a distribution under the null hypothesis of natural variability by finding the strongest trend in each model 47-year record piece which spans at least 15 years. (Here we suppose that there is some minimum record length at which the trend would have gotten our attention; however, the qualitative result is not sensitive to reasonable choices of this threshold value.) We compare the maximum observed trend (of record length $\geq$ 15 years) to the null hypothesis distribution and find the observed maximum trend consistent with the null hypothesis, regardless of whether we compare trends of different record periods in units of days/(total record segment) or in days/year (P=0.6 in either case). The 7-day shift toward earlier t_{rise} in the Mauna Loa CO_2 record (from 1966 to 1993) thus appears consistent with natural variability as represented by the model, when considered in the context of the entire record.

Table 4.1. **Trends in annual cycle of CO_2 at Mauna Loa from 1960-2006.** Trends calculated from 5 record-year fits of frequency modulated model (Eqn. 4.1). P_{internal} are P-values for rejection of null hypothesis of no trend and are calculated by Monte-Carlo test against 10000 phase-randomized instances of time series. P_{model} are P-values for test of null hypothesis that trend is consistent with range of trends expected due to natural variability. We build test distribution for P_{model} by calculating 47-year trends of each value from output from 1000-year carbon cycle model integration (*Doney et al.*, 2006). Instances where the model does not produce a single trend of the magnitude of the observed trend are indicated with an asterisk(*). There are two amplitude tests because the modelled Mauna Loa amplitude is 60% of the observed amplitude. Thus, in addition to comparing the raw amplitude trends, we also compare the amplitudes when both are normalized to a mean value of one. The normalized amplitude test is the more appropriate test. Both are shown in order to demonstrate that the result is not dependent on the normalization.

Parameter	MLO Trend	P_{internal}	P_{model}
Rise Time	$-12.1\ \frac{\text{days}}{\text{47 years}}$	$P<0.01$	$P_{\mathrm{model}}=0.001$
Drop Time	$-2.41\ \frac{\text{days}}{\text{47 years}}$	$P=0.3$	$P_{\mathrm{model}}=0.3$
Amplitude	$0.566\ \frac{\text{ppmv}}{\text{47 years}}$	$P<0.001$	$P_{\mathrm{model}}<0.001$*
Normalized A	$18.3\ \frac{\text{percent}}{\text{47 years}}$	$P<0.001$	$P_{\mathrm{model}}<0.001$*

4.4 Changes in Seasonality at Barrow

Changes in seasonality have also been reported at high latitudes. *Keeling et al.* (1996) reported amplitude increases and trends toward earlier t_{drop} at Barrow, *Randerson et al.* (1999) attributed 1980-1997 changes in the structure of the annual cycle of atmospheric CO_2 at high latitudes to increases in early season net ecosystem uptake and *Piao et al.* (2008)

gave particular attention to rise-day trends at high northern latitudes (and to Barrow in particular). The NOAA CMDL Barrow flask CO_2 time series extends from 1971 to present and is the longest high-latitude Northern Hemisphere record we possess (*Tans et al.*, 1989). We will examine this record for the presence of significant and anomalous changes in seasonal structure. The annual cycle of atmospheric CO_2 variability at Barrow, Alaska is marked by more rapid seasonal transitions between high and low carbon values than Mauna Loa, due to the brief seasonal period of significant carbon uptake and of significant carbon release (compare Fig. 4.3a to Fig. 4.2a).

The observed trend in amplitude at Barrow is 1.26 ppmv/(33 years), (or 0.04 ppmv/year) a highly significant trend ($P<0.001$). This trend is also anomalous when compared with the distribution of 33-year model-simulated trends ($P<0.02$). Here again we have rescaled the model simulated amplitudes so that the mean is the same as that of the observations. This is a larger correction at high northern latitudes than at Mauna Loa – at Barrow the modelled amplitude is only 30% of the observed amplitude.

The amplitude of the annual cycle at Barrow has continued to increase since it was noted more than 10 years ago by *Keeling et al.* (1996), and we find a 16% amplitude increase from 1974-2006. This is compared to an 8% increase in the amplitude of the annual cycle at Mauna Loa over the same period. If we presume that at the beginning of the NOAA record the amplitude has already grown by 20% (as implied by *Keeling et al.'s* analysis of early, unreleased observations made at Barrow from 1961-1967 (*Kelley*, 1964a,b)), we infer that the amplitude at Barrow has grown by ∼39% from 1961 to 2006.

Barrow t_{rise} shifted earlier by 11.5 days from 1974-2006. However, this shift occurs entirely in the first half of the record, before 1990 (Fig. 4.3c). Though this represents a fairly large shift, it is not a significant trend when evaluated against the spectrum of variability in the record ($P=0.1$), nor is it anomalous when compared with variability predicted by the model variability ($P=0.13$; see Table 4.2). Because the record could be characterized by a trend in the first half and a constant value in the second half, we also test for the presence of an anomalous internal trend period using the method described in the analysis of the MLO t_{drop} record, and find no indication of anomalous internal trends ($P=0.7$ and $P=0.4$ for the days/year and days/segment methods respectively).

Barrow t_{drop} also shifted earlier from 1974-2006, however the trend has flattened since *Keeling et al.'s* observation (Fig. 4.3d). The 4.04 days/(33 year) trend toward earlier spring carbon draw-down is significant when evaluated against the spectrum of variance present in the time series itself ($P<0.01$), but 33-year trends of this magnitude are commonplace in the simulation, and we do not reject the hypothesis that the observed t_{drop} trend is consistent with natural variability ($P=0.4$). We likewise fail to detect anomalous internal trends.

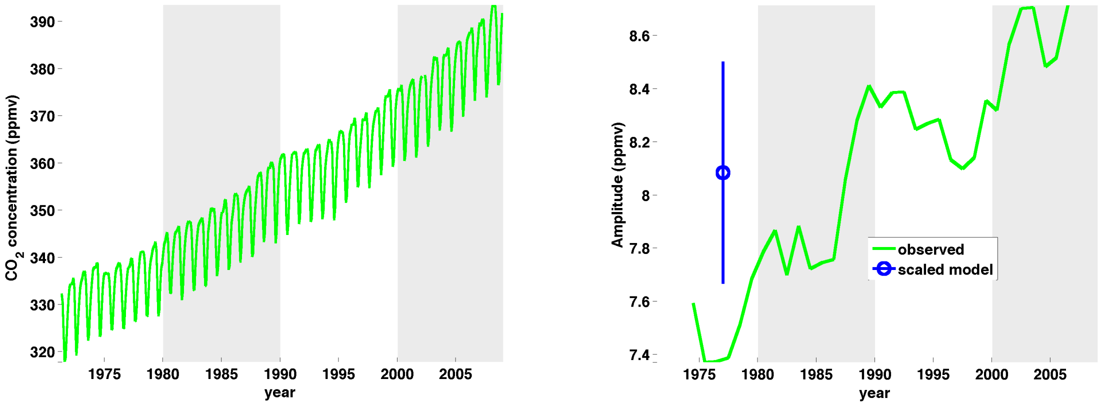

(a) Barrow CO_2 time series

(b) Barrow amplitude (A)

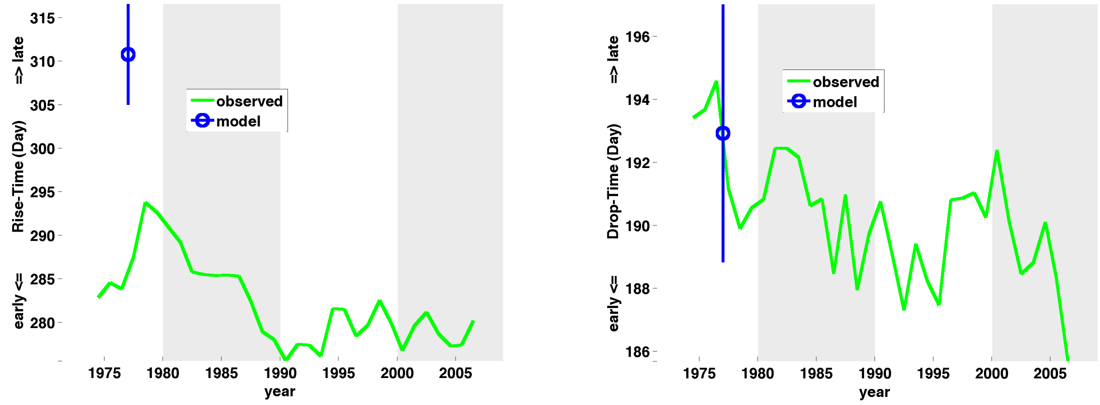

(c) Barrow rise-time (t_{rise})

(d) Barrow drop-time (t_{drop})

Figure 4.3. **Point Barrow seasonality:** same as Fig. 4.2, but for Point Barrow, Alaska using 1971-2008 data from the National Oceanographic and Atmospheric Administration's (NOAA) CO_2 flask sampling program. The blue line indicating model variability has *not* been shifted in either of the lower panels. Day 280 represents October 21^{st}. Day 190 represents July 23^{rd}.

Table 4.2. **Trends in annual cycle of CO_2 at Barrow from 1974-2006.** Same as Table 4.1, but for the 1974-2006 NOAA CMDL flask record from Barrow, Alaska.

Parameter	BRW Trend	P_{internal}	P_{model}
Rise Time	$-11.5\ \frac{\text{days}}{33\ \text{years}}$	P=0.1	P_{model}=0.12
Drop Time	$-4.04\ \frac{\text{days}}{33\ \text{years}}$	P<0.01	P_{model}=0.4
Amplitude	$1.26\ \frac{\text{ppmv}}{33\ \text{years}}$	P<0.001	P_{model}<0.001*
Normalized A	$15.6\ \frac{\text{percent}}{33\ \text{years}}$	P<0.001	P_{model}<0.02

4.5 Representativeness of Mauna Loa and Barrow Variability

The Mauna Loa and Barrow time series represent our longest Northern Hemisphere records at low and high latitudes respectively. How representative of the large-scale are they though?

We address this question by considering the more extensive network of shorter CO_2 records, and the simulated scales of variability in the model of *Doney et al.* (2006). We first consider the climatological distribution of CO_2 amplitude, t_{drop}, and t_{rise} using the surface flask and continuous CO_2 monitoring network and estimates of middle tropospheric CO_2 from the Atmospheric Infrared Sounder (AIRS) instrument aboard NASA's Aqua satellite (*Chahine et al.*, 2008). We then estimate the spatial scale of representativeness of the Mauna Loa and Barrow records using the General Circulation Model of *Doney et al.* (2006). Finally, we use the intermediate length surface records (>10 record years) to identify regions of coherent amplitude, t_{drop} and t_{rise} variability.

4.5.1 Climatological Context

We start by considering the variability of seasonality with latitude. Because of the strong latitudinal gradient in solar isolation, and the rapid mixing of air along a latitudinal circle, we expect a strong latitudinal signal in all three variables. We estimate the climatological pattern of A, t_{rise} and t_{drop} for those surface CO_2 observing stations where Eqn. 4.1 explains more than 60% of the record variance for 5-year record segments. In order to broaden the spatial context (the surface network covers only a small fraction of the globe), we also consider the latitudinal climatology of the $2° \times 2.5°$ gridded AIRS L3 CO_2 data. The AIRS instrument measures the spectrum of atmospheric emissions and estimates of atmospheric CO_2 made using AIRS reflect concentrations of CO_2 at the emission levels of photons in the CO_2 emission bands. In practice, AIRS CO_2 estimates are indicative of atmospheric CO_2 concentrations sampled over a broad region of the middle troposphere. The vertical height range at which the AIRS instrument is sensitive to CO_2 varies with time and depends on the temperature and the concentration of other atmospheric constituents, particularly water vapor. At times, the signal is contaminated by a sensitivity to stratospheric CO_2 which leads to large errors if the signal is interpreted as a measure of tropospheric CO_2 (*Chahine et al.*, 2008; *Maddy et al.*, 2008). We adopt a looser criteria for data inclusion for the AIRS results and allow locations where >30% of the record variaence is explained by Eqn. 4.1. The AIRS data should be considered an indirect measurement, less reliable than the flask and continuous sampler observations, and the plausibility of the AIRS data may be considered a test for the reliability of the AIRS data themselves.

The latitudinal distribution of A, t_{rise}, and t_{drop} in the surface network is instructive (Fig. 4.4). Amplitude increases with latitude in the Northern Hemisphere, with surface values close to 1 ppmv near the Equator and approaching 10 ppmv at mid-to-high latitudes (Fig. 4.4a). Maximum values and maximum variability occurs in the midlatitudes, though this may be in part due to the fact that we possess many long records in highly vegetated regions in the midlatitudes but only a few such records at high latitudes. Note that if we exclude the high-variance continental interior stations which are responding to local terrestrial influences, the spread in the distribution of amplitudes at any given latitude is much narrower and the equator-to-pole gradient in amplitude appears linear. The picture that emerges then is of a steady (close to linear) increase in amplitude with latitude at the marine boundary layer and at stations on the western edges of continents, with much larger climatological amplitude and amplitude variability at locations near regions of large seasonal carbon exchange. Amplitudes reach a minimum in the Southern Hemisphere tropics, where the variability ceases to look anything like Eqn. 4.1 (and the points are thus excluded from Fig. 4.4). There is a Southern Hemisphere relative maximum in amplitude between 40°S and 65°S , where amplitudes reach ∼0.6 ppmv, far smaller than in the Northern Hemisphere.

The AIRS middle tropospheric measurements show a similar latitudinal structure to that of the surface flask network (Fig. 4.4b). Northern Hemisphere amplitudes are uniformly smaller in the middle troposphere (by about a factor of 2 when compared to surface stations away from the continental interiors). Between 25°N and 45°N AIRS amplitudes are relatively uniform with latitude, perhaps indicative of relatively rapid mixing in the strong midlatitude middle troposphere winds. The AIRS data show a minimum amplitude in the Southern Hemisphere tropics, in the same region where the surface network shows a minimum, though the amplitudes are larger in the AIRS middle troposphere observations than at the surface. This increase of amplitude with height in the mid-to-low latitude Southern Hemisphere has been observed by *in situ* observations (*Pearman and Beardsmore*, 1984), and modelling studies have attributed it to the propagation of the Northern Hemisphere annual cycle signal into the Southern Hemisphere in the upper limb of the Hadley Cell (*Fung et al.*, 1987; *Pearman and Hyson*, 1980, 1986). AIRS Southern Hemisphere amplitudes increase south of 40°S , consistent with the surface network, but again the amplitudes here are larger than would be predicted from the surface record (AIRS middle tropospheric amplitudes are here about twice the surface amplitude).

A comparison of the latitudinal distribution of the timing of surface spring carbon drawdown (t_{drop}, Fig. 4.4c) with the timing of surface fall carbon release (t_{rise}, Fig. 4.4e) shows the asymmetry between the hemispherically abrupt onset of photosynthesis in spring and

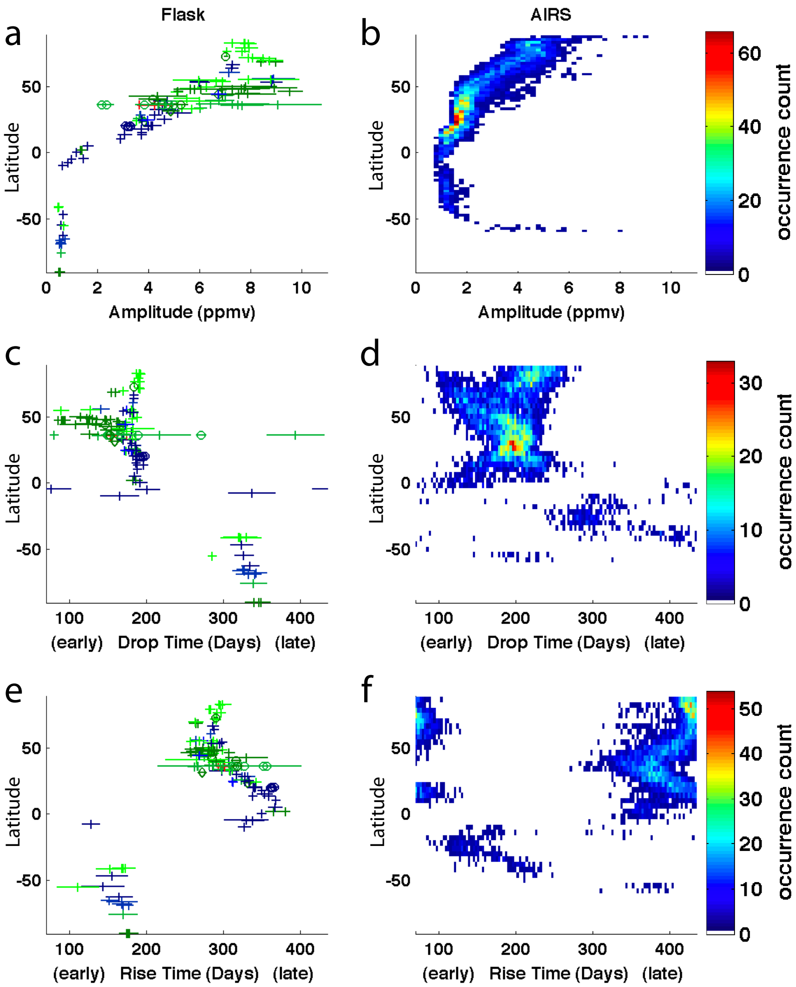

Figure 4.4. **CO_2 seasonality vs. latitude:** The latitudinal distribution of climatological amplitude, t_{drop}, and t_{rise} for the annual cycle of atmospheric Carbon Dioxide variability. **(a)** Amplitude vs. latitude for surface flask and continuous sampler CO_2 observations. The long-term-average amplitude is marked with a plus (+) symbol (boundary layer observations) or with a circle (o) symbol (high mountains). The two desert locations (Assekrem, Algeria & Sede Boker, Israel) are marked with a diamond (◇) symbol. The width of the horizontal line going through each marker indicates the temporal standard deviation of each record, which is better constrained for longer records than for shorter records. Continental interior stations are in dark green. Stations on the western edge of continents are light green. Stations in the ocean interior are in dark blue. Stations on the western edge of oceans are in light blue. Mediterranean stations are marked in red. Because the x-axis is truncated at 12 ppmv, the Hungarian station, an extreme outlier, is not shown. **(b)** 2D histogram of long-term-mean amplitude occurrence as a function of latitude in AIRS middle tropospheric CO_2 measurements. Color indicates occurrence count. **(c)** same as (a), but for t_{drop}. Note that time axis is circular and goes from day 70 (March 25^{th}) to day 435 (March 25^{th} of following year), rather than from day 0 (January 15^{th}) to day 366 (January 15^{th} of following year). **(d)** same as (b), but for t_{drop}. **(e)** same as (a), but for t_{rise}. **(f)** same as (b), but for t_{rise}.

the return of carbon in the fall. The Northern Hemisphere t_{drop} pattern traces the flow of the spring carbon pulse from the mid- and high-latitude forests to the remote observing stations measuring the background concentration. Carbon draw-down reaches its midway point (t_{drop}) as early as late April at European and North American interior stations that are observing the local removal of carbon from the atmosphere by the surrounding vegetation. There is considerable spread in the timing of t_{drop} in these continental interior stations which are confined to the midlatitudes and a handful of high-latitude stations in the our network. At oceanic stations, and at land stations on the western edges of continents that presumably sample marine air, spring draw-down occurs approximately 80 days after the first continental interior draw-down (though t_{drop} at most continental interior stations leads the large-scale background t_{drop} by much less than this). At these remote locations t_{drop} has only a weak latitudinal dependence, and appears to propagate from the midlatitudes into the tropics. The overall picture in the Northern Hemisphere is of a carbon removal pulse that starts in the continental interior at different times at different locations followed by a rapid hemispheric draw-down of carbon visible at all latitudes.

The hemispheric pattern of carbon release, as shown by the latitudinal distribution of t_{rise} gives a quite different impression (Fig. 4.4e). As with t_{drop}, the earliest t_{rise}s occur in the midlatitude continental interiors. However, unlike t_{drop}, t_{rise} shifts toward later as we move southwards out of the midlatitudes towards the Equator. There is also a suggestion of a delay in t_{rise} as we move northward from the northern mid latitudes towards the pole, but if any such trend truly exists, it is weak. AIRS t_{drop}, though more broadly scattered than surface values, show little clear dependence on latitude in the Northern Hemisphere (Fig. 4.4d). Average AIRS t_{drop} occurs $\sim$60 days after the surface boundary layer t_{drop} at high latitudes (Fig. 4.4d). AIRS t_{rise}, on the other hand, shows a much larger delay relative to the surface and shows a strong latitudinal gradient similar to the latitudinal gradient in t_{rise} seen in the surface network (Fig. 4.4f). The overall latitudinal picture of the CO_2 annual cycle that emerges from the surface and middle troposphere observations is then one of CO_2 variability driven by mid- to high-latitude continental interior signals, which propagate rapidly across latitudes in the spring and more slowly in the autumn.

Differences in the climatological values of A, t_{drop} and t_{rise} between land and ocean are the primary source of Northern Hemisphere zonal variability (Figs. 4.5, left-hand column). The highly vegetated regions of Northern Europe and eastern North America show particularly large amplitude relative to oceanic stations at the same latitude, while the arid western United States has amplitudes that are more moderately elevated compared to stations at the same latitude that sample marine air. The t_{drop} contrast between land and ocean is stark, while the t_{rise} contrasts between land and ocean is relatively small (Figs. 4.5c,e), which we conceptualize as the difference between the abrupt onset of spring photosynthesis and the slow release of carbon by respiration over a longer portion of the year. Spatial coverage of surface stations in the Southern Hemisphere is much more sparse than the Northern Hemisphere, and it is difficult to resolve the separate influence of the land and ocean in the climatological Southern Hemisphere distribution of seasonality (Figs. 4.5, right-hand column). The stations surrounding the Drake Passage have a larger amplitude than either the stations along the coast of East Antarctica to the south, or New Zealand and Tasmania to the north, which suggests an annual variability in this region driven by upwelling in the Drake Passage. Both t_{drop} and t_{rise} are much earlier in Ushuaia, on the north edge of the Drake Passage, than anywhere else in the Southern Hemisphere extratropics. At the other Southern Hemisphere stations, t_{rise} becomes later as you move either north or south from the Antarctic Circumpolar Current, while the gradient in t_{drop} is toward later carbon draw-down the closer you move toward the pole.

4.5.2 Representativeness of Temporal Variability

The climatological distribution of A, t_{drop} and t_{rise} which we see in the surface observational network contains a structure which can be explained in terms of a latitudinal gradient and a land-ocean contrast. However, there is no reason to suppose the pattern of temporal variability has a similar structure to the spatial variability. We use two approaches to evaluate the assess the spatial scales of variability of A, t_{drop} and t_{rise}. First, we use a General Circulation Model with fully coupled carbon model (*Doney et al.*, 2006) to assess the spatial representativeness of the temporal variability observed at Mauna Loa and Barrow. Second, we identify a number of regions for which we can detect common variability in the time series of surface observations.

Representativeness of Mauna Loa and Barrow in Numerical Model

We began our discussion by identifying significant and anomalous changes in seasonality in the long records at Mauna Loa and Barrow. Over what spatial scale is the variability shown in these records representative? To address this question, we extracted the time series of CO_2 variability at the model grid box corresponding to Mauna Loa and Barrow and calculated yearly values of A, t_{rise}, and t_{drop}. We then correlated these time series with time series of the same parameters for the bottom atmospheric layer at each latitude and longitude of the model (Fig. 4.6). The Barrow observing station is 11 meters above sea level and is thus in the same model level as the surface boxes it is correlated with. The Mauna Loa observation point, in contrast, is 3397 meters above sea level, and is thus removed in the vertical from the points it is correlated with. This weakens all of the correlations (show in the left-hand column of Fig. 4.6) relative to the correlation between each grid point and the surface grid box below Mauna Loa. In fact, the monthly rate of change of CO_2 concentrations at Mauna Loa is more strongly correlated with the monthly rate of change of CO_2 concentrations at the tropopause than at the surface throughout most of the Northern Hemisphere.

Mauna Loa A is correlated with surface ocean A throughout the Northern Hemisphere. This correlation is strongest in the Pacific and in the midlatitudes. We also see positive correlations over North Africa, the Middle East and Central Asia. Positive correlations be-

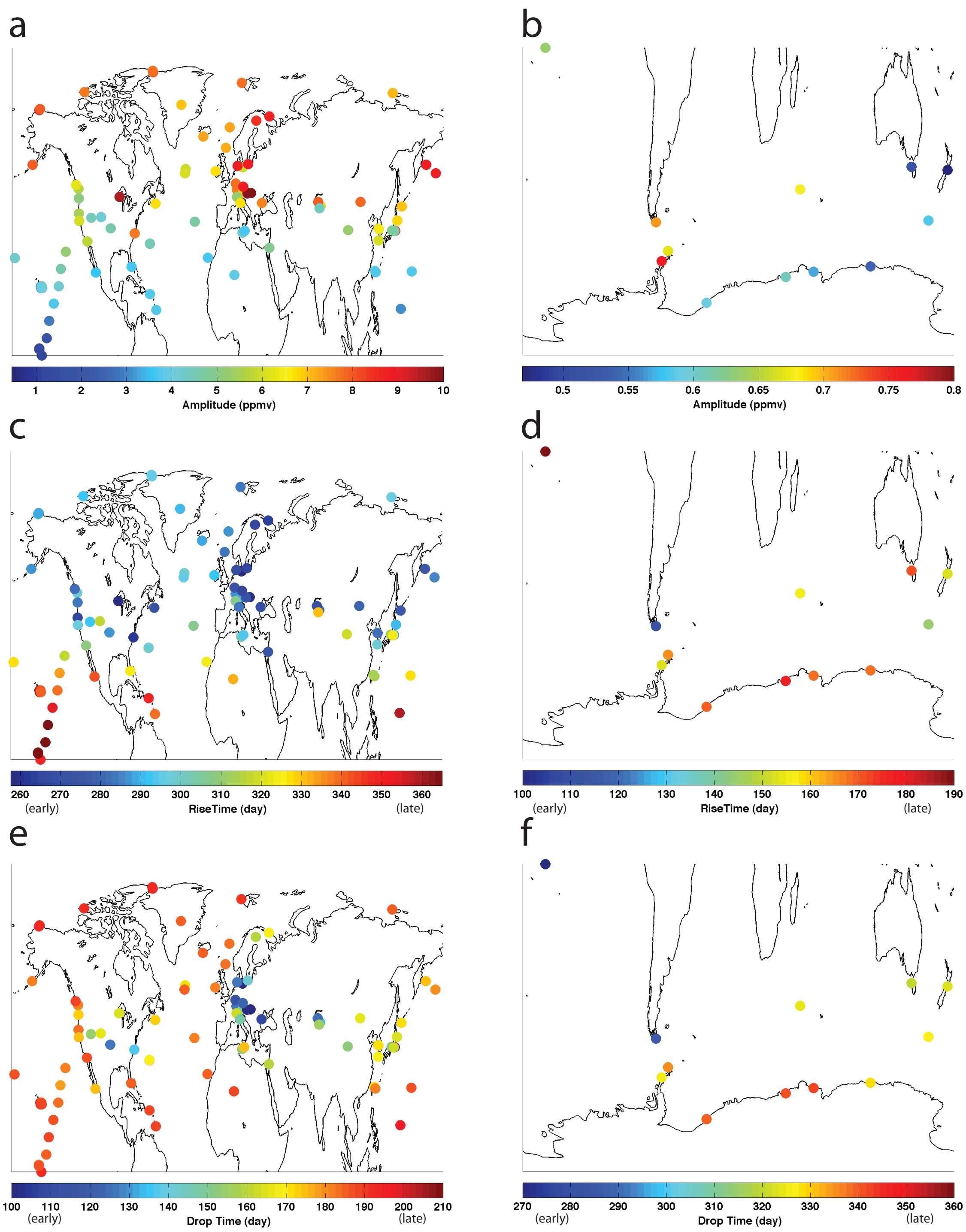

Figure 4.5. **Surface climatology:** Long-term-mean values of A, t_{rise} and t_{drop} for surface stations in map view. **(a)** Map of Northern Hemisphere A for each surface location. A is given by color. **(b)** same as (a), but for Southern Hemisphere. **(c) and (d)** same as (a) and (b), but for rise-day (t_{rise}). **(e) and (f)** same as (a) and (b), but for drop-day (t_{drop}). Dates are given in Julian days, offset so that day 0 represents January 15^{th}, day 100 represents April 24^{th}, day 200 represents August 2^{nd}, and day 300 represents November 10^{th}.

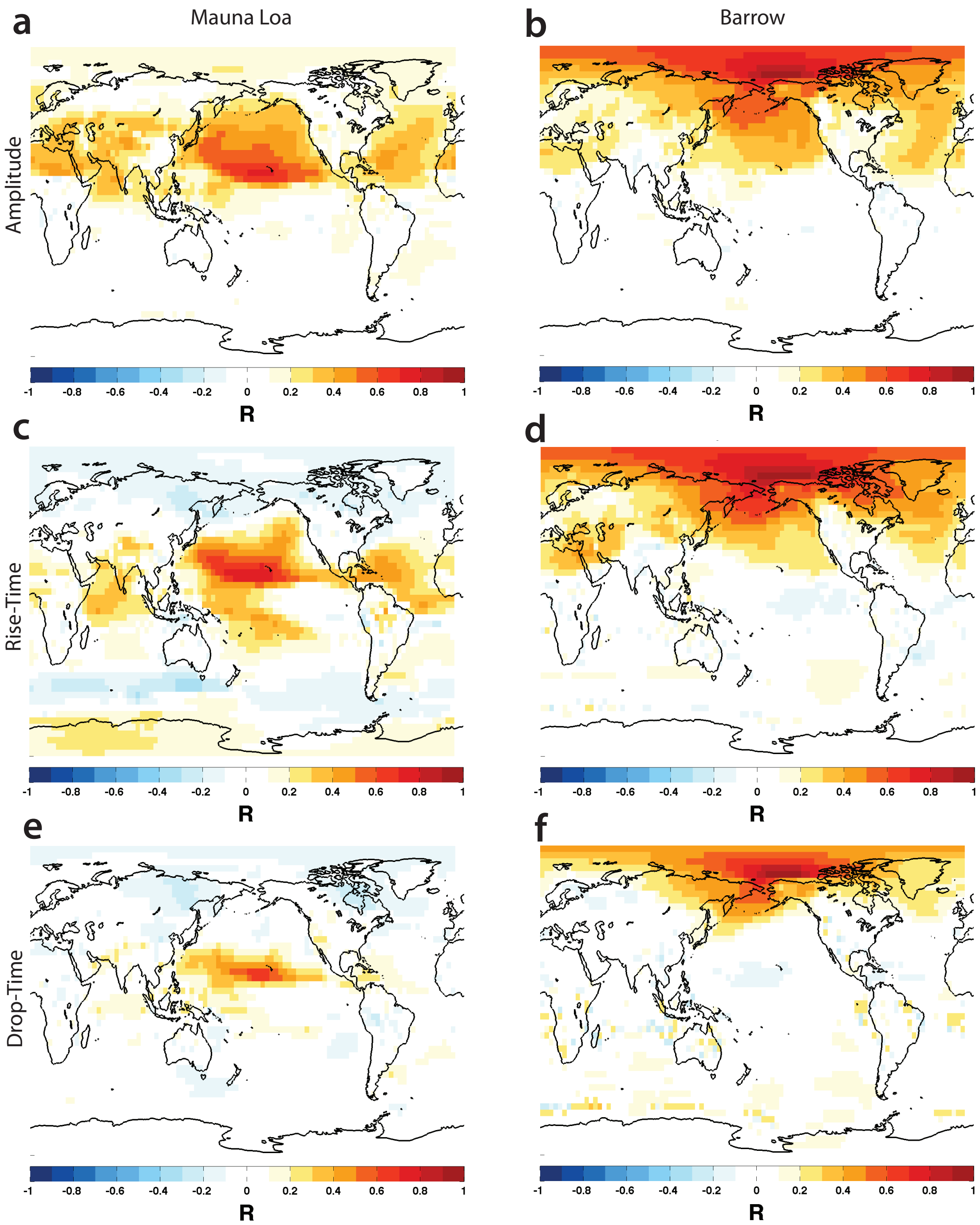

Figure 4.6. **Seasonality correlation maps:** Spatial maps of correlation of A, t_{rise} and t_{drop} in the 1000-year simulation (*Doney et al.*, 2006). **(a)** Correlation between time series of amplitude (A) at Mauna Loa with the A time series at each surface grid point. Mauna Loa time series taken from the grid box at the latitude, longitude and altitude of Mauna Loa in our model of natural atmospheric carbon variability. **(b)** same as (a), but for Point Barrow. **(c) and (d)** same as (a) and (b), but for rise-time (t_{rise}), rather tan A. **(e) and (f)** same as (a) and (b), but for drop-time (t_{drop}), rather than A.

tween Mauna Loa t_{rise} and the surface ocean are more confined to the tropics and northern midlatitudes. Dynamical effects are more clearly evident in the t_{rise} field – Mauna Loa t_{rise} is negative correlated with surface t_{rise} in the Arctic and in the Southern Ocean, and positive correlations extend from the western Pacific warm pool into the Southern Hemisphere. Looking at the surface layer alone, however, does not show the sense of communication between the ocean basins. The increase in CO_2 concentrations that causes the time series to cross its trend-line (controlling t_{rise}) occurs in October November and December (OND). The full three-dimensional field of correlations between Mauna Loa OND CO_2 concentrations changes (the growth rate) and OND growth rate at all other model grid boxes shows that variability at Mauna Loa is correlated with variability over the entire Northern Hemisphere tropopause (Fig. 4.7). This correlation field also shows that the tropopause CO_2 concentration signature propagates toward the surface in the regions of seasonally descending air – the East Pacific high, the Azores High, and North Africa and the Middle East (*Kalnay et al.*, 1996). These correlations extend to a region of descending air in the South Pacific as well (see Fig. 4.7). Mauna Loa t_{drop} is more locally confined and is the least spatially representative of the seasonality parameters. Surface t_{drop} variability is correlated with MLO t_{drop} variability over only a 15° latitude band in the North Pacific. If our goal is to diagnose hemispheric scale changes in terrestrial carbon cycling, then t_{drop} appears to be less informative than either t_{rise} or A.

By correlating modelled variability in seasonality at Barrow with variability at each surface grid-box we find that (similarly to Mauna Loa) A variability is representative of variability over a larger area than t_{rise}, which is representative of variability over a larger area that t_{drop} (Fig. 4.6, right-hand column). A shared variability in amplitude and t_{rise} appears to exist over much of the Arctic, which is correlated to variability over much of the North Atlantic and North Pacific.

Regions of Coherent variability

In the last section we used the 1000-year model simulation of *Doney et al.* (2006) to infer the spatial representativeness of the A, t_{rise}, and t_{drop} records at Mauna Loa and Barrow. Here we test these model predictions using the much sparser network of surface observations and identify other regions of coherent variability. Our goal here is to asses to what extent anomalous trends identified at Mauna Loa and Barrow can used to make inferences about the large-scale carbon cycle.

Hawaii

The variability on the big island of Hawaii alone is instructive (Fig. 4.8). We have two monitoring locations, one atop Mauna Loa, and one at sea level at Cape Kumukahi, but seven different time series. These consist of flask observation time series taken at Mauna Loa Observatory by three different organizations (the National Oceanic and Atmospheric Administration (NOAA), Scripps Institution of Oceanography (SIO), and Australia's Commonwealth Scientific and Industrial Research Organisation (CSIRO)), continuous observa-

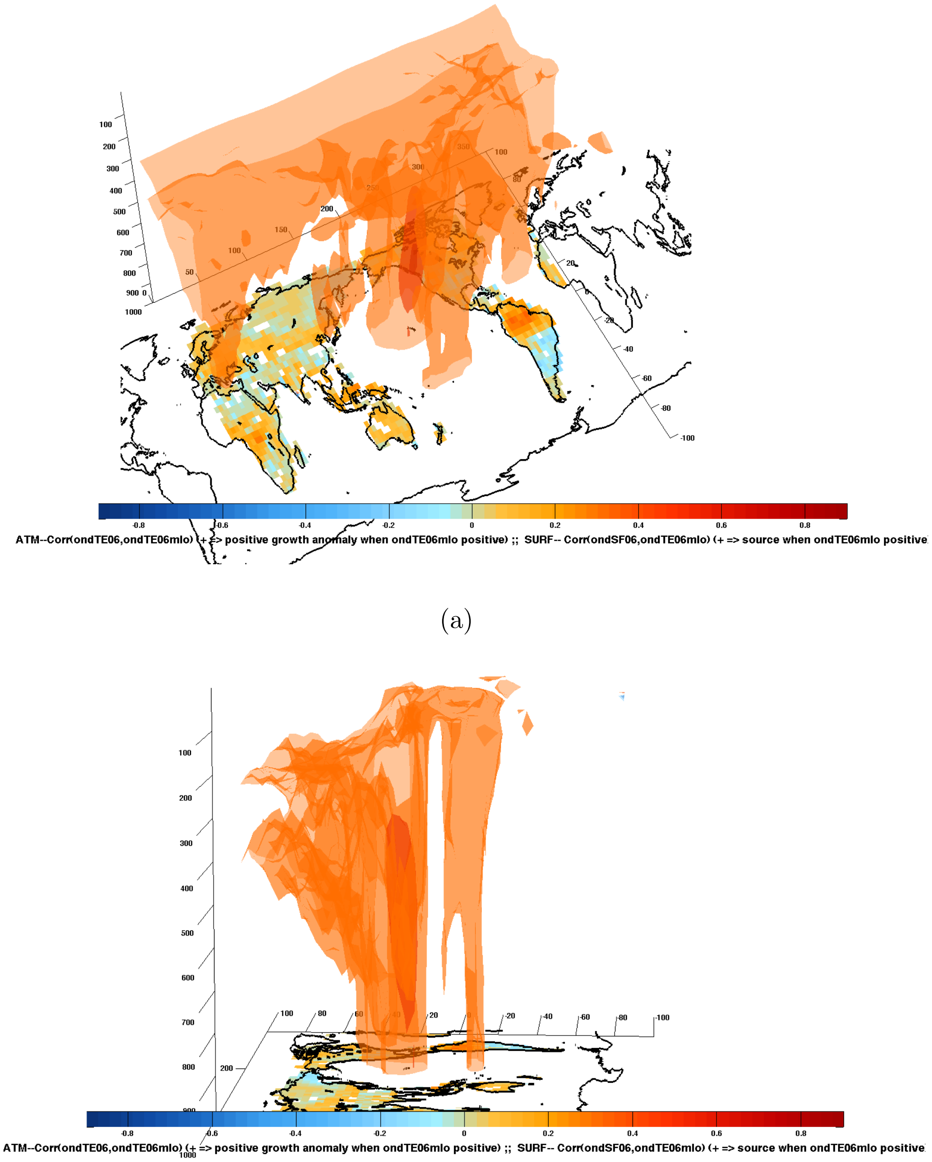

(a)

(b)

Figure 4.7. **Correlation with Mauna Loa OND CO_2 growth rate:** Isosurfaces of correlation between October, November, December (OND) CO_2 growth rates at Mauna Loa and OND CO_2 growth rates at all grid points in three dimensions. OND growth rates represent the growth rates when Mauna Loa CO_2 concentrations are increasing leading up to t_{rise}. The R=0.3, R=0.6 and R=0.9 isosurfaces are shown. **(a) and (b)** represent two different views of the same three-dimensional field. Mauna Loa OND growth rates are more strongly correlated with upper troposphere OND growth rates than with surface growth rates through most of Northern Hemisphere. The regions where the R=0.3 surface extends down from the upper troposphere to the surface are regions of seasonally downwelling air in the Pacific High, the Azores High, the Eastern Mediterranean, and the downwelling region in the tropical South Pacific.

tions from two organizations (NOAA and SIO), as well as two flask observation time series at Cape Kumukahi (from NOAA and SIO). A comparison of agreement and disagreement between these time series gives some indication of the robustness of the observations and of what level of variability we expect between different sampling locations in the absence of any true physical differences. Amplitude is 25% larger at sea level (Cape Kumukahi) than at Mauna Loa. This climatological offset between Mauna Loa and Cape Kumukahi appears to be a large-scale result, not the effect of local terrestrial fluxes from Hawaii itself influencing the surface climatology. This assertion is supported by the fact that we see essentially the same amplitude as Cape Kumukahi as the 20°N station of the shipboard East Pacific transect (located 1500 km east of Hawaii). Earlier analysis (Fig. 4.5) showed a strong latitudinal gradient in amplitude in this region and our inference is that the climatological amplitude at Cape Kumukahi is representative of the regional surface amplitude at 19.5°N. The vertical contrast thus appears to be a measurement of the attenuation of amplitude variability with height, also visible in the AIRS observations, in surface-based column CO_2 observations (*Yang et al.*, 2002) and in model simulations. Though different in detail, all four of the long Mauna Loa amplitude records give the same sense of variability – increases in amplitude from the late 1970s to the early 1990s and then a marked decrease centered on the year 2000 (associated with Northern Hemisphere drought) followed by a recovery. The variability in A at the bottom of the mountain (Cape Kumukahi) is, however, completely different in character. In fact the two time series at Cape Kumukahi are quite different from each other.

The Mauna Loa t_{rise} time series show general agreement with each other, though some of the transient excursions are larger in the flask time series than in the continuous time series. The transient shift towards earlier seasons from the late 1970s to the early 1980s is larger in both the NOAA and SIO flask time series than in the NOAA and SIO continuous time series. A relative maximum (later) t_{rise} in 1996 is large in the CSIRO flask record, but quite small in all four other Mauna Loa records. These differences between the continuously-sampled and flask-sampled Mauna Loa t_{rise} time series is troubling. One interpretation is that these differences are due to the inability of intermittent flask sampling to correctly capture seasonal transitions. If this were the case, it would call into question our ability to estimate seasonal transition timing at all sites from flask measurements. Note, however, that both these discrepancies are at the beginning of the Mauna Loa flask observations made by the respective agencies, and that the discrepancies between the flask time series and the continuous time series seem to disappear starting in the 1980s in both the NOAA and the SIO records. This is encouraging and suggests that the differences may be due to transients in the first years of each program when protocols were first being developed. We proceed, aware that some variability may be present in the record due to variability in sampling alone, and that this variability may be larger in NOAA and SIO records before ~1985, and in CSIRO records of time. Variability due to sampling protocols should introduce noise, but the nature of this noise should vary from location to location. Shared variability across space (which is what we seek to identify in the following sections) should therefore be interpreted in most cases as a common atmospheric signal, not a common noise signal.

All the records show a shift toward earlier t_{rise} from the late 1980s to the late 1990s, and then a recovery in the early 2000s, though the magnitude of the excursion was larger at the surface than atop Mauna Loa. The time history of t_{drop} varies substantially across the seven records, though the two Mauna Loa continuous records agree for most of the record (Fig. 4.8d). The shift from 1993 to 1995 towards later t_{drop} (by $\sim$6 days) followed by a return to $\sim$1993 levels from 1998 to 2005 is, however, seen in all records except for the CSIRO record (which is far shorter than the other records and is arguably not long enough to resolve this excursion).

The extent of the disagreement between the time variability of A, t_{rise}, and t_{drop} observed in the six records of atmospheric CO_2 on the big island of Hawaii is larger than we find at any other location. Perhaps this is in part due to Mauna Loa being used as a test site for the development of new observing systems. We point it out to emphasize the amount of variability that may exist in A, t_{rise}, and t_{drop} records independent of what the atmosphere itself is doing. At most locations we have only a single record and have no check on observer-dependent variability in the record.

Arctic

The collection of station records shown in Fig. 4.9 represents the collection of remote Arctic observing stations (as well as a number of subarctic stations) with long records that share a common signal. It represents a somewhat subjective collection, indicative of the spatial extent of the region which contains a similar CO_2 amplitude time variability as the Barrow record. Though the climatological amplitudes in each record vary, the temporal variability is shared. The record here which is least like the other records is Cold Bay, which at 55°N is spatially on the edge of this cluster. Despite the fact that each record covers a different time period, we see a trend toward larger amplitude in all the "Arctic" stations. This trend is interrupted by a dip in amplitude from $\sim$1996-1999, earlier than the dip in amplitude seen at Mauna Loa and throughout the lower-latitude Northern Hemisphere. The differences between stations in the t_{rise} and t_{drop} time series at these stations is more pronounced, and to help in visually identifying the similarities and differences between the time series we have shifted each record to a zero mean and rescaled each record to unit variance (Figs. 4.9c,4.9d). The t_{rise} records are clearly not all recording the same thing. Four of the five records that extend as far back as 1990 all indicate a shift around 1987 toward earlier t_{rise} (by $\sim$2 standard deviations), followed by a partial recovery around 1993. This is the t_{rise} shift which produces the trend found in the Barrow, Alaska record. The indication here is that this trend is representative of variability in t_{rise} in the Western Hemisphere high northern latitudes (as represented by Barrow, Alert, Cold Bay and Mould Bay). The only station that does not see this trend is Station M – spatially separated in the North Atlantic from the four stations that see this decrease in amplitude. After 1995 there appears to be some high-frequency variability that is episodically seen across many stations, but it is difficult to clearly identify a common signal. The presence of common variability in t_{drop} in the "Arctic" network is still more difficult to discern, though a shift toward later t_{drop} by $\sim$1.5 standard deviations around 1995 is seen in many records.

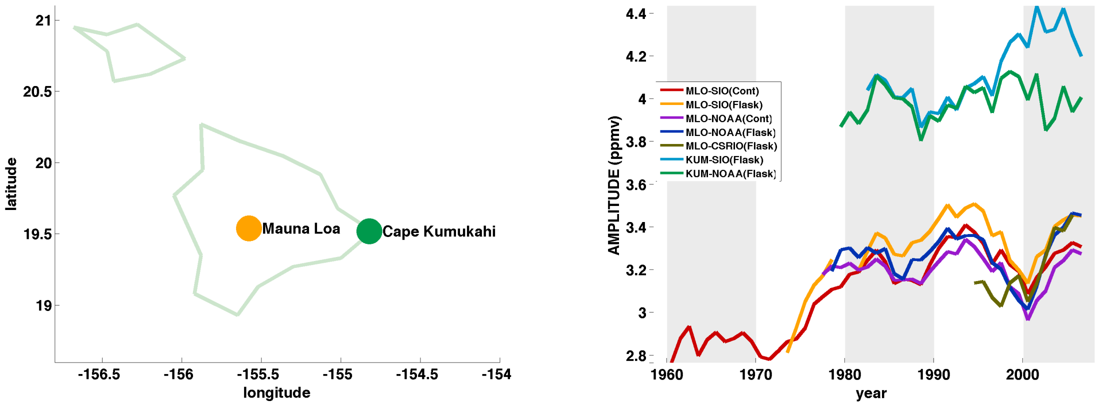

(a) Hawaii stations

(b) Hawaii amplitude

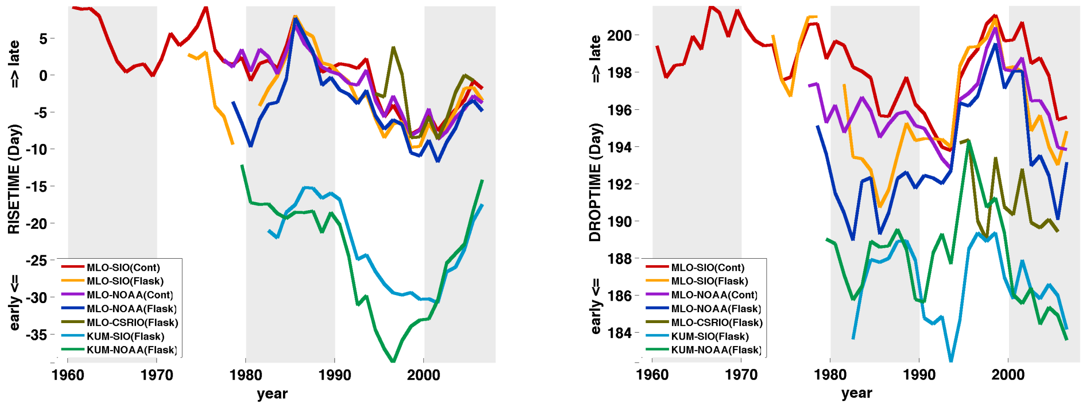

(c) Hawaii t_{rise}

(d) Hawaii t_{drop}

Figure 4.8. **Records from the Hawaiian Big Island:** Variability in seasonality from records from the big island of Hawaii. **(a)** Map of location of the Mauna Loa (MLO) and Cape Kumukahi (KUM) CO_2 observing locations on the big island of Hawaii. **(b)** Amplitude time series from five monthly CO_2 records from Mauna Loa Observatory (MLO) at 3397 meters and two records from Cape Kumukahi (KUM) at 3 meters elevation. Legend indicates organization that collected each data set and whether the time series is derived from flask measurements, or continuous observations. Every other decade is shaded in grey. **(c)** Same as (b), but for rise-time (t_{rise}). More positive numbers indicate later autumn carbon increases. Day zero represents January 15^{th}. **(d)** Same as (b), but for drop-time (t_{drop}). More positive numbers indicate later spring carbon draw-down. Day 200 represents August 2^{nd}.

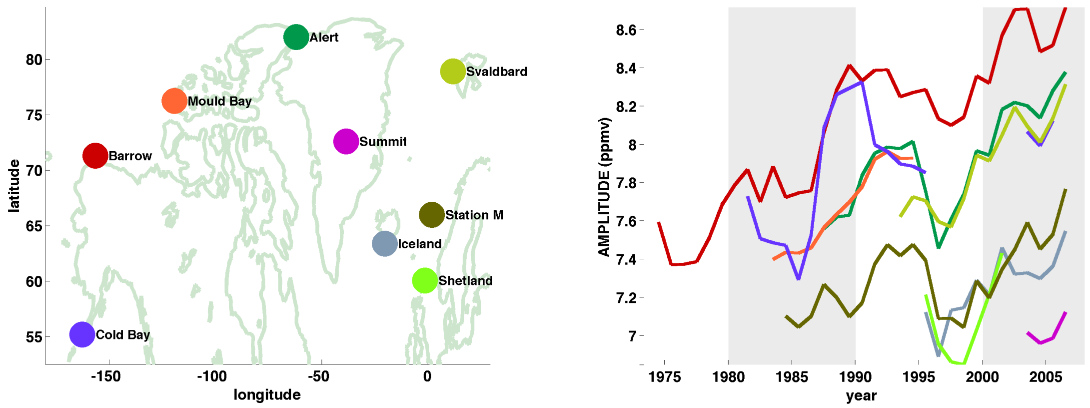

(a) Arctic stations

(b) Arctic amplitude

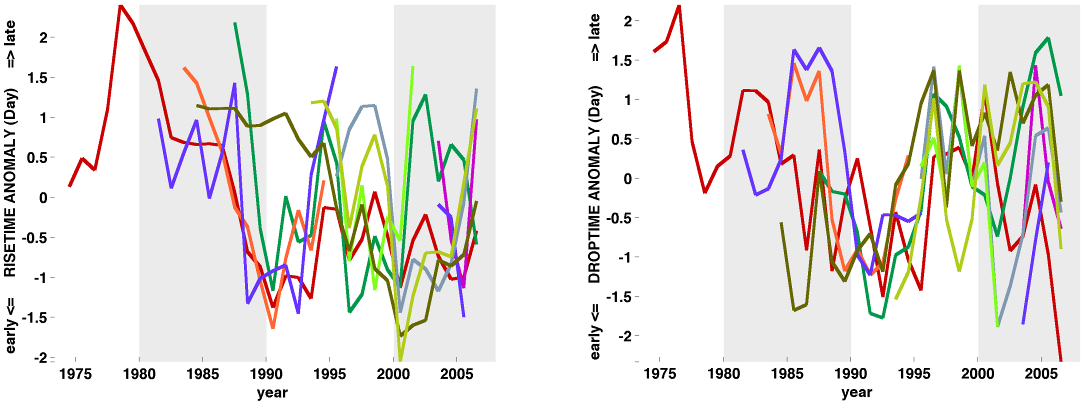

(c) Arctic t_{rise}

(d) Arctic t_{drop}

Figure 4.9. **Records from the "Arctic" collection:** Variability in seasonality for the collection of nine high northern latitude stations referred to as the "Arctic" stations in the main text. Note than unlike Figs. 4.8 and 4.11, this figures presents anomaly time series of t_{rise} and t_{drop}; this is because of the relatively large spread in the climatological mean values of these parameters over this network. **(a)** Map indicating location and name of the monitoring station in the "Arctic" collection. **(b)** Absolute amplitude time series for the "Arctic" network. The locations that the time series with a given color line is derived from is indicated by the location of the dot with the same color in subplot (a). Every other decade is shaded in grey. **(c)** Same as (b), but for rise-time (t_{rise}) *anomalies*. More positive numbers indicate later autumn carbon increases. Day zero represents the long-term-mean t_{rise} at each station. **(d)** Same as (b), but for drop-time (t_{drop}) *anomalies*. More positive numbers indicate later spring carbon draw-down. Day zero represents the long-term-mean t_{drop} at each station.

Northern Mid-to-Low Latitudes
The collection of station records shown in Fig. 4.10 represents a collection of stations in the Northern Hemisphere mid-to-low latitudes that contain an amplitude time-history common to the Northern Hemisphere mid-to-low latitudes (as opposed to that of the high latitudes). As with the high latitude stations, this represents a subjective choice of records that appear to contain a mid-to-low latitude "background" signal, as opposed to a signal influenced by local sources and sinks. The amplitude records have been normalized by their long-term-mean amplitude, and the t_{rise} and t_{drop} records have been shifted to zero mean and normalized to unit variance. The main point we want to illustrate here is that the transient decrease in amplitude centered on the year 2000 (noted by *Buermann et al.* (2007)) is a widespread pattern through the remote Northern Hemisphere middle and lower latitudes. t_{rise} and t_{drop} variability are less spatially coherent, consistent with model predictions that they vary on smaller spatial scales.

Antarctic
Finally we turn to the Southern Hemisphere record. The annual cycle of atmospheric CO_2 variability in the Southern Hemisphere is much smaller than in the Northern Hemisphere, and varies from year-to-year much more than in the Northern Hemisphere. We consider the longest records from the Southern Hemisphere extratropics (Fig. 4.11). With the exception of South Pole, these stations all border on the Southern Ocean. The high-latitude Southern Hemisphere records show a common history of amplitude variability. Southern amplitude decreased after 1981, recovered to a maximum around 1993, decreased again to a minimum in 1997-1998, increased again to a sharp peak that appears in all records in 2000, and then dropped again. There are transient features of t_{rise} and t_{drop} that appear to be coherent over more limited geographic regions, but the variability in these records of timing appears, like in the Northern Hemisphere, to be more locally confined.

4.6 Causes of Amplitude Change

We set out to understand what aspects of seasonal change in the long records were significant, anomalous, and representative of large-scale processes. Our results indicate that we should focus on the amplitude variability. Amplitude is the only one of the three seasonality metrics considered that contains significant, anomalous trends at both Mauna Loa and Barrow. Model results, and the observational network analysis, indicate that amplitude variability at most locations in the remote Northern Hemisphere boundary layer (far from large local terrestrial surface fluxes) is correlated with either amplitude variability at Mauna Loa, or with amplitude variability at Barrow. The challenge, then, is to understand the source of variability in terrestrial carbon fluxes that controls variability in the high-latitude Barrow time series, and in the low-latitude Mauna Loa time series.

The large-scale character of amplitude variability indicates that variability in atmospheric circulation is unlikely to be a major factor in modulating amplitude variability, and that this

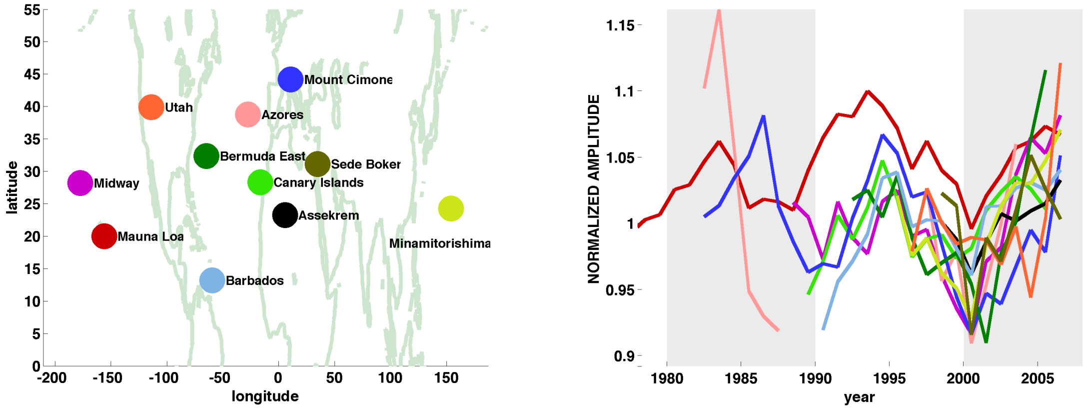

(a) Northern mid-to-low latitude stations (b) Northern mid-to-low latitude amplitudes

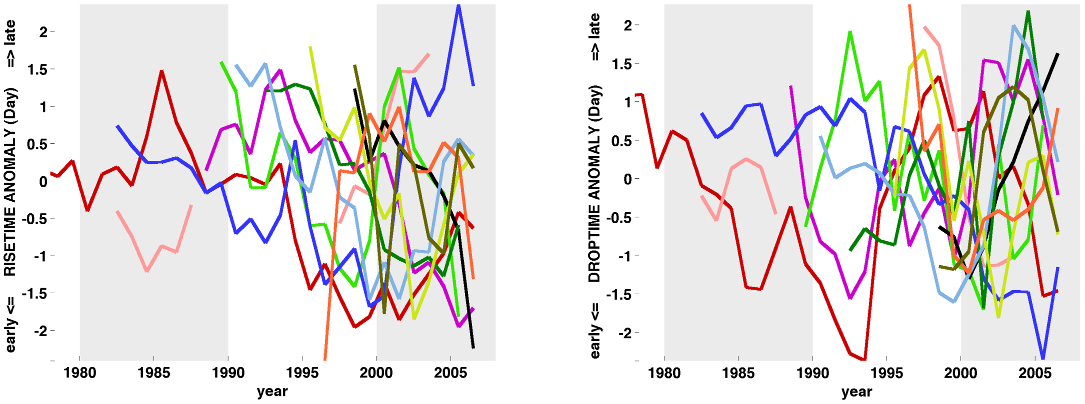

(c) Northern mid-to-low latitude t_{rise} (d) Northern mid-to-low latitude t_{drop}

Figure 4.10. **Records from the "Northern Mid-to-Low Latitude" collection:** Same as Fig. 4.9, but *(i)* for the collection of mid-to-low latitude Northern Hemisphere stations referred to as the "Northern Mid-to-Low Latitude" stations in the main text and *(ii)* panel (b) shows time series of normalized amplitude, rather than raw amplitude (in contrast to panel (b) of Figs. 4.8,4.9, and 4.11). This is to facilitate visual comparison of temporal variability between this collection of time series which has a large spread in climatological amplitude.

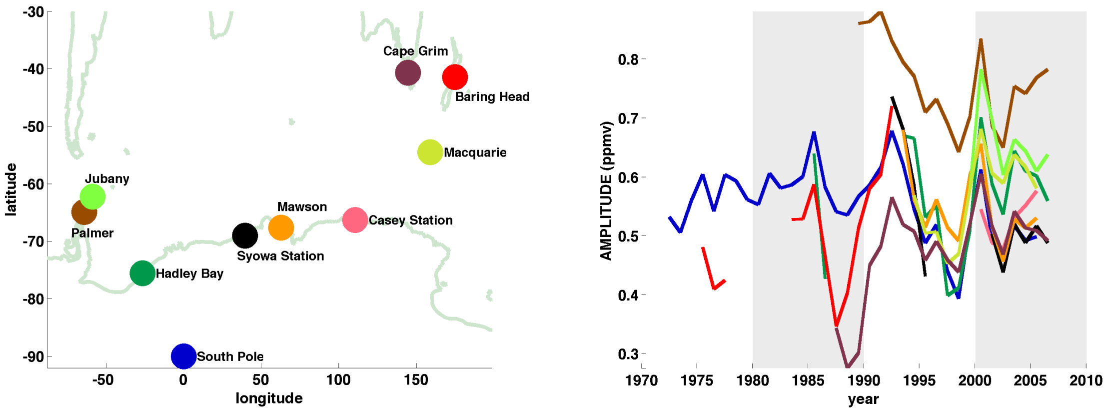

(a) Antarctic stations

(b) Antarctic amplitude

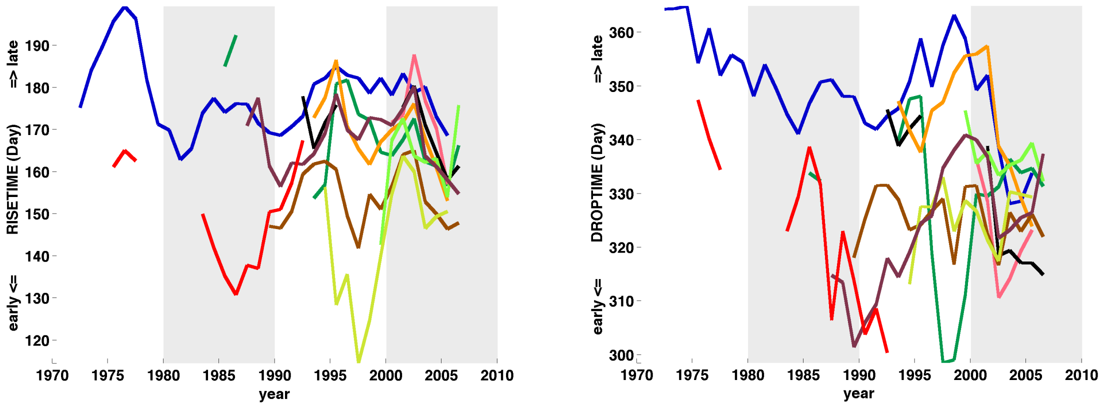

(c) Antarctic t_{drop}

(d) Antarctic t_{rise}

Figure 4.11. **Records from the "Antarctic" collection:** Same as Fig. 4.8, but for the collection of high-latitude Southern Hemisphere stations referred to as the "Antarctic" stations in the main text. Line colors in (b),(c) and (d) refer to stations with same color indicated in (a). Note that all panels show raw time series (not anomalies or normalized records). Day 150 represents June 13^{th}. Day 330 represents December 10^{th}.

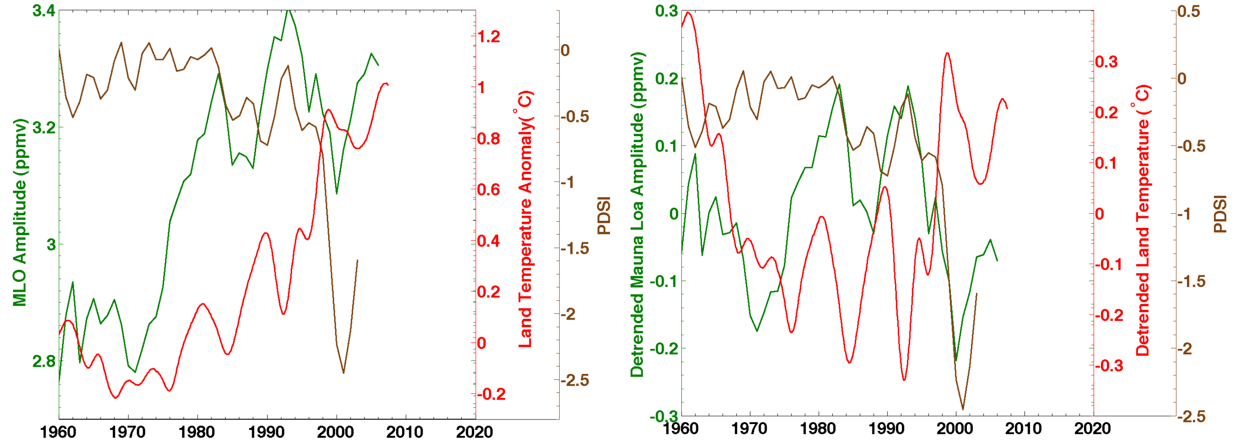

(a) MLO A, Land Temperature, and PDSI (b) MLO A, Land Temperature (detrended), PDSI

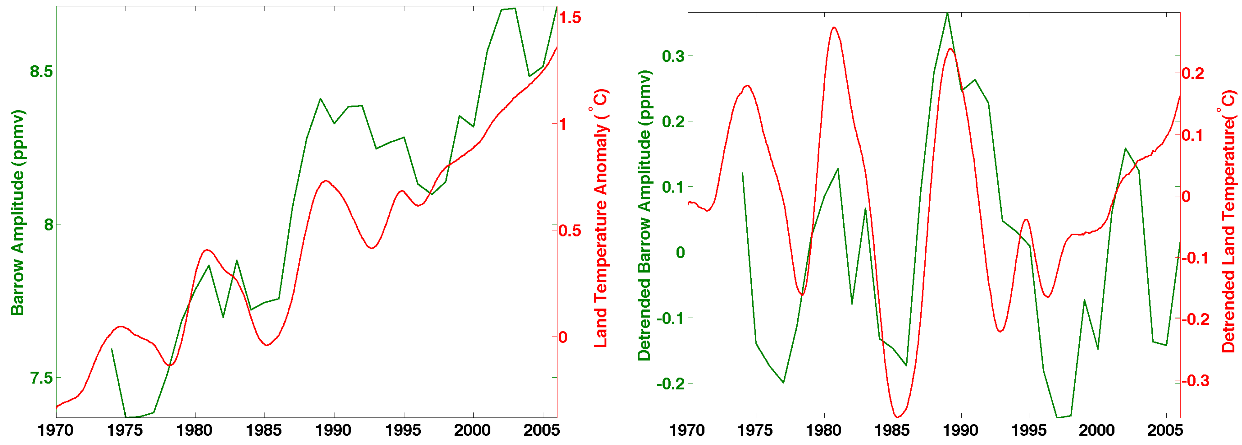

(c) BRW A and Land Temperature (d) BRW A and Land Temperature (detrended)

Figure 4.12. **CO_2 amplitude, land temperature and PDSI:** Detrended relationship between amplitude of annual cycle of atmospheric CO_2, land temperature averaged over latitude range and the Palmer Drought Severity Index (PDSI). **(a)** Mauna Loa amplitude time series (green), land temperature averaged from 20°N to 50°N (red), and PDSI averaged over the same region. **(b)** same as (a), but the amplitude and temperature time series have been detrended. **(c)** Barrow amplitude time series (green), land temperature averaged from 50°N to 90°N (red). **(d)** same as (a), but the time series have been detrended.

is instead an indication of variability of the well-mixed component of seasonal hemispheric CO_2 concentration. In particular, the transient decrease in amplitude centered on the year 2000 is seen in both the Atlantic and the Pacific (as well as the Indian Ocean, not shown) and at a variety of latitudes, and is thus unlikely to be a product of circulation changes.

The recorded increase in amplitude at both Mauna Loa and Barrow are coincident with a period of large-scale warming. Photosynthesis is temperature limited in many regions (*Nemani et al.*, 2003);. However, photosynthesis may also be stimulated by CO_2 fertilization (*Long et al.*, 2004), anthropogenic nitrogen fertilization (*Reay et al.*, 2008), or increases in global precipitation (*Weltzin et al.*, 2003; *Zhang et al.*, 2007), and so the correspondence in time of the trend towards increased amplitude and increased global temperatures is not sufficient to conclude that the observed amplitude increase is a simple response to warming. *Keeling et al.* (1996) concluded that the magnitude of the observed amplitude increase is larger than can be explained by the direct sensitivity of photosynthesis to temperature (based on the temperature sensitivity of photosynthesis given by *Larcher*, 1984) and hypothesized that the trend in amplitude is a result of increases in the length of the growing season, motivated largely by the trend towards earlier t_{drop} they saw at Mauna Loa. Our conclusion that the trend in t_{drop} at Mauna Loa has recovered, is neither significant nor anomalous, and is not representative of large-scale variability removes some of the motivation for this inference. While the ultimate origin of the increase in annual Northern Hemisphere carbon cycling may be different from the cause of the inter-annual variability, we focus on the inter-annual variability in the following as a way of understanding the relationship between climate and annual carbon cycling.

Buermann et al. (2007) made a convincing case that Mauna Loa amplitude variability can not be understood as a simple response to increased temperatures. Though both Mauna Loa amplitude and land temperatures have increased since 1960, their time variability are quite different (see Fig. 4.12). *Buermann et al.* (2007) focused on a sharp decrease in Mauna Loa amplitude from 1991-2004 and show that this is coincident with a the large-scale Northern Hemisphere "super-drought" (*Hoerling and Kumar*, 2003; *Lotsch et al.*, 2005). The physical interpretation is that while increased temperatures may be important to the long-term increase in the amplitude of the annual cycle in CO_2 at mid-to-low latitudes, moisture also plays an important role, particularly in the extreme case of drought. The relationship between moisture variability and Mauna Loa amplitude is also not a simple one. In fact, in our analysis, Mauna Loa amplitude variability is significantly correlated with neither 20°N-50°N average land temperatures (R=-0.02, P=0.9, detrended correlation), nor with the Palmer Drought Severity Index (PDSI) over the same latitudes (R=-0.02, P=0.6). However, there is no reason to expect a large biological system to be dominated by a single mechanism over the entire record, or to expect this limitation to be linear. The coincidence of the largest decrease in amplitude and the largest midlatitude drought on record, as well as the obvious physical relationship between drought and photosynthesis, make a compelling case for the importance of droughts in modulating midlatitude CO_2 amplitude. This argument is further supported by the fact that the Mauna Loa amplitude has since recovered, consistent with the termination of the drought (see Fig. 4.12a).

The observed amplitude trend at Barrow is stronger (in both a relative and an absolute sense) than the trend at Mauna Loa, indicating large changes in the carbon cycle at high latitude. The relationship between high-latitude land temperature and Barrow amplitude is much stronger than the relationship at lower latitudes, and we find a marginal significant correlation between the detrended time series (R=0.4, P=0.08; see Fig. 4.12d). High latitude annual carbon fluxes appear to be modulated by temperature. The relationship between the detrended time series of Barrow amplitude and land temperature (averaged over land northward of 50°N) allow us to test the extent to which the trend in Barrow amplitude can be explained by the trend in high-latitude land temperature. We regress the detrended Barrow amplitude on detrended high-latitude land temperature, and use this regression coefficient and the full high-latitude land temperature time series (*not* detrended) to predict the trend in amplitude due to temperature alone. The observed amplitude trend at Barrow is 0.04 ppmv/year and the modelled trend due to temperature is 0.02 ppmv/year. We conclude that half of the trend toward increased in CO_2 amplitude at Barrow is associated with increased temperature over land north of 50°N. Note that there are reasons that the long-term relationship between temperature and amplitude may be different from the short-term relationship. Our analysis only captures processes that respond quickly to temperature. To the extent that annual productivity has an autoregressive character (due, for example, to investment by plants in growth to support future productivity (*Bonan*, 2002)), this approach will underestimate the the long-term sensitivity of amplitude to climate and the fraction of the long-term trend in high-latitude amplitude that can be explained by high-latitude warming. Increased temperatures may mobilize nutrients at high latitudes (*Chapin III et al.*, 1995), which may continue to be available in following years (but see *Mack et al.*, 2004, for ambiguity of effect of nutrient input on net carbon flux). In contrast, to the extent that biological systems acclimate to changes in climate (*Oechel et al.*, 2000), estimating the relationship between temperature and amplitude based on the inter-annual relationship may overestimate the component of the long-term trend associated with warming.

4.7 Concluding Remarks

Observational constraints firmly establish that the land surface has taken up vast amounts of carbon over the anthropogenic era. The observed rate of atmospheric CO_2 rise has been only half the rate at which we are injecting carbon into the atmosphere, and this "airborne fraction" has remained quite constant over the decades (when averaged over the timescale of ENSO cycles; *Denman et al.* (2007)). Atmospheric carbon isotope (*Fung et al.*, 1997; *Joos and Bruno*, 1998; *Francey et al.*, 1995) and oxygen measurements (*Keeling and Shertz*, 1992; *Bender et al.*, 1998; *Battle et al.*, 2000) indicate that about a quarter of anthropogenic carbon is taken up by the terrestrial biosphere, with another quarter taken up by the ocean[1]. Because emissions are increasing, this would imply the land sink is also increasing. Identifying where this carbon is being taken up is one of the fundamental questions driving research on the terrestrial carbon cycle. Note that this firm global constraint that net land carbon uptake is positive and likely increasing stands at odds with the sense of much of the ecological literature that suggest, based on many local studies, a biosphere that is increasingly releasing carbon in response to climate change, especially at high latitudes (*Piao et al.*, 2008; *Goulden et al.*, 1998; *Dixon et al.*, 1994; *Oechel et al.*, 1993, 2000). As of this writing, the relationship between changes in amplitude and changes in net annual flux is not clear. Changes in the amplitude of the annual cycle do not fundamentally require a net sink or a net source. This can be understood in the simplest case by considering a system in which annual photosynthesis and respiration are in balance. If we simply double the photosynthesis and the respiration at all times, the amplitude of the annual cycle of carbon fluxes will increase, but there will be no change in net flux.

The observed amplitude variability does not tell us what the net surface flux is, but it does inform our interpretation of the processes that modulate surface fluxes on multiple timescales. A visual comparison of the detrended Mauna Loa CO_2 amplitude time series and the Northern Hemisphere temperature and PDSI time series (Fig. 4.12b) shows a strong similarity between the two records after 1983, the time that large sustained mid-to-low latitude droughts begin. Our interpretation then is that annual midlatitude Northern Hemisphere terrestrial carbon fluxes transitioned to a strongly moisture-limited state in the mid-1980s. The amplitude of the annual cycle of atmospheric carbon dioxide is a diagnostic for changes in the carbon fluxes associated with fast-turnover carbon pools. But other lines of evidence indicate that a transition to moisture limitation may also be occurring in slower-turnover carbon pools. Tree rings give a direct record of carbon storage as woody biomass by individual trees at annual timescales. Many trees record a transition away from carbon storage modulated by temperature during the mid-to-late 20^{th} century (*Briffa*, 1998; *Briffa et al.*, 1998; *D'Arrigo et al.*, 2008). The cause of this observed "divergence" between tree-ring growth and temperature is unknown, but some trees start exhibiting a positive correlation

---

[1] Note that the above budget is based on fossil and cement manufacturing emissions alone. Estimates of carbon release from deforestation vary widely, but atmospheric observations constrain the *net* terrestrial carbon flux. Thus any carbon released from the terrestrial biosphere by deforestation, natural or anthropogenic, is taken back up elsewhere in the terrestrial biosphere *in addition* to the uptake of one quarter of fossil emissions.

with precipitation at about the same time they diverge from the temperature record (*Jacoby and D'Arrigo*, 1995). This suggests a transition to a more moisture-limited biosphere is effecting carbon fluxes at multiple timescales.

Underlying much current research done to estimate surface-air carbon fluxes is a desire to understand how climate change effects the amount of carbon sequestered from the atmosphere by natural systems. Fluxes associated with rapid turnover carbon pools are much larger than the fluxes associated with slow turnover pools, making it quite difficult to make direct inferences about slow-turnover carbon pools. We are often left to assume that carbon input into fast-turnover pools scales with carbon input into slow-turnover pools, thought detailed studies call into question this assumption (*Chapin III et al.*, 1995). We propose that the transition to drought modulation of the terrestrial carbon cycle indicates an avenue to test the relationship between climate-limitation of carbon storage and exchange between different carbon pools. We intend to pursue this work by an examination of climate modulation of carbon storage in slow-turnover carbon pools as represented by the tree-ring record, seeking similarities and differences between the climate modulation seen in the tree-ring record, and climate modulation of the fast-turnover pools seen in the annual variations of atmospheric carbon dioxide.

Bibliography

Andres, R., G. Marland, I. Fung, and E. Matthews, A 1° x 1° distribution of carbon dioxide emissions from fossil fuel consumption and cement manufacture, 1950-1990, *Global Biogeochemical Cycles*, *10*, 419–429, 1996.

Balling, R., P. Michaels, and P. Knappenberger, Analysis of winter and summer warming rates in gridded temperature time series, *Climate Research*, *9*(3), 175–181, 1998.

Barnston, A., and R. Livezey, Classification, seasonality and persistence of low-frequency atmospheric circulation patterns, *Monthly Weather Review*, *115*(6), 1083–1126, 1987.

Battle, M., M. Bender, P. Tans, J. White, J. Ellis, T. Conway, and R. Francey, Global carbon sinks and their variability inferred from atmospheric O_2 and δ^{13}C, *Science*, *287*(5462), 2467–2470, 2000.

Bender, M., M. Battle, and R. Keeling, The O_2 balance of the atmosphere: A tool for studying the fate of fossil-fuel CO_2, *Annual Review of Energy and the Environment*, *23*, 207–223, 1998.

Berger, A., Long-term variations of daily insolation and Quaternary climatic changes, *Journal of the Atmospheric Sciences*, *35*(12), 2362–2367, 1978.

Berger, A., Insolation values for the climate of the last 10 million years, *Quaternary Science Reviews*, *10*, 297–317, 1991.

Blackmon, M., et al., The Community Climate System Model, *Bulletin of the American Meteorological Society*, *82*(11), 2357–2376, 2001.

Blasing, T., C. Broniak, and G. Marland, The annual cycle of fossil-fuel carbon dioxide emissions in the United States, *Tellus B*, *57*(2), 107–115, 2005.

Boden, T., G. Marland, and R. Andres, Global, regional, and national fossil-fuel CO_2 emissions, , Carbon Dioxide Information Analysis Center, Oak Ridge National Laboratory, U.S. Department of Energy, Oak Ridge, Tenn., U.S.A, doi:10.3334/CDIAC/00001, 2009.

Bonan, G., *Ecological climatology: concepts and applications*, Cambridge University Press, Cambridge, UK, 2002.

Bretherton, C., M. Widmann, V. Dymnikov, J. Wallace, and I. Blade, The effective number of spatial degrees of freedom of a time-varying field, *Journal of Climate*, *12*(7), 1990–2009, 1999.

Briffa, K., Trees tell of past climates: but are they speaking less clearly today?, *Philosophical Transactions of the Royal Society B: Biological Sciences*, *353*(1365), 65, 1998.

Briffa, K., F. Schweingruber, P. Jones, T. Osborn, S. Shiyatov, and E. Vaganov, Reduced sensitivity of recent tree-growth to temperature at high northern latitudes, *Nature*, *391*(6668), 678–682, 1998.

Brohan, P., J. Kennedy, I. Harris, S. Tett, and P. Jones, Uncertainty estimates in regional and global observed temperature changes: A new data set from 1850, *Journal of Geophysical Research-Atmospheres*, *111*, doi:10.1029/2005JD006,548, doi:ARTND12106, 2006.

Buermann, W., B. R. Lintner, C. D. Koven, A. Angert, J. E. Pinzon, C. J. Tucker, and I. Y. Fung, The changing carbon cycle at Mauna Loa Observatory, *Proceedings of the National Academy of Sciences of the United States of America*, *104*, 4249–4254, doi:DOI10.1073/pnas.0611224104, 2007.

Cao, M., and F. Woodward, Dynamic responses of terrestrial ecosystem carbon cycling to global climate change, *Nature*, *393*(6682), 249–252, 1998.

Chahine, M., L. Chen, P. Dimotakis, X. Jiang, Q. Li, E. Olsen, T. Pagano, J. Randerson, and Y. Yung, Satellite remote sounding of mid-tropospheric CO_2, *Geophys. Res. Lett*, *35*, 2008.

Chapin III, F., G. Shaver, A. Giblin, K. Nadelhoffer, and J. Laundre, Responses of arctic tundra to experimental and observed changes in climate, *Ecology*, *76*(3), 694–711, 1995.

CLIMAP Project Members, The surface of the ice-age Earth, *Science*, *191*, 1131–1137, 1976.

CLIMAP Project Members, Seasonal reconstruction of the Earth's surface at the last glacial maximum, *Geol. Soc. Amer.*, p. 17, 1981.

CLIMAP Project Members, The last interglacial ocean, *Quaternary Research*, *21*, 123–224, 1984.

Cohen, J., and D. Entekhabi, Eurasian snow cover variability and Northern Hemisphere climate predictability, *Geophysical Research Letters*, *26*(3), 345–348, 1999.

Cohen, J., K. Saito, and D. Entekhabi, The role of the Siberian high in Northern Hemisphere climate variability, *Geophysical Research Letters*, *28*(2), 299–302, 2001.

Cohen, J., D. Salstein, and K. Saito, A dynamical framework to understand and predict the major Northern Hemisphere mode, *Geophysical Research Letters*, *29*(10), doi:ARTN1412, 2002.

Cohen, J., A. Frei, and R. Rosen, The role of boundary conditions in AMIP-2 simulations of the NAO, *Journal of Climate*, *18*(7), 973–981, 2005.

Cox, P., R. Betts, C. Jones, S. Spall, and I. Totterdell, Acceleration of global warming due to carbon-cycle feedbacks in a coupled climate model, *Nature*, *408*(6809), 184–187, 2000.

Crutzen, P., and W. Steffen, How long have we been in the Anthropocene era?, *Climatic Change*, *61*(3), 251–257, 2003.

Cuming, M. J., and B. A. Hawkins, TERDAT: The FNOC System for Terrain Data Extraction and Processing. Technical Report Mil Project M-254 (second edition)., , Prepared for USN/FNOC and published by Meteorology International Inc., 1981.

Dai, A., K. Trenberth, and T. Qian, A global dataset of Palmer Drought Severity Index for 1870–2002: Relationship with soil moisture and effects of surface warming, *Journal of Hydrometeorology*, *5*, 1117–1130, 2004.

D'Arrigo, R., R. Wilson, B. Liepert, and P. Cherubini, On the 'divergence problem' in northern forests: A review of the tree-ring evidence and possible causes, *Global and Planetary Change*, *60*(3-4), 289–305, doi:10.1016/j.gloplacha.2007.03.004, 2008.

Denman, K. L., et al., *Climate Change 2007: The Physical Science Basis. Contribution of Working Group I to the Fourth Assessment Report of the Intergovernmental Panel on Climate Change*, chap. 7. Couplings Between Changes in the Climate System and Biogeochemistry, Cambridge University Press, Cambridge, United Kingdom and New York, NY, USA, 2007.

Dixon, R., S. Brown, R. Houghton, A. Solomon, M. Trexler, and J. Wisniewski, Carbon pools and flux of global forest ecosystems, *Science*, *263*(5144), 185–189, 1994.

Doney, S. C., K. Lindsay, I. Fung, and J. John, Natural variability in a stable, 1000-yr global coupled climate-carbon cycle simulation, *Journal of Climate*, *19*, 3033–3054, 2006.

Eliseev, A., I. Mokhov, and M. Guseva, Sensitivity of amplitude–phase characteristics of the surface air temperature annual cycle to variations in annual mean temperature, *Izvestiya, Atmospheric and Oceanic Physics,*, *42*(3), 300–312, 2006.

Forster, P., and V. Ramaswamy, *Climate Change 2007: The Physical Science Basis. Contribution of Working Group I to the Fourth Assessment Report of the Intergovernmental Panel on Climate Change*, chap. 2. Changes in Atmospheric Constituents and in Radiative Forcing, 129-234 ed., Cambridge University Press, Cambridge, United Kingdom and New York, NY, USA, 2007.

Francey, R., P. Tans, C. Allison, CE, I. Enting, J. White, and M. Trolier, Changes in oceanic and terrestrial carbon uptake since 1982, *Nature*, *373*(6512), 326–330, 1995.

Friedlingstein, P., et al., Climate-carbon cycle feedback analysis: Results from the C^{4}MIP model intercomparison, *Journal of Climate*, *19*(14), 3337–3353, 2006.

Fung, I., K. Prentice, E. Matthews, J. Lernder, and G. Russell, Three-dimensional tracer model study of atmospheric CO_2: Response to seasonal exchanges with the terrestrial biosphere, *Journal of Geophysical Research-Oceans and Atmospheres*, *88*(NC2), 1281–1294, 1983.

Fung, I., C. Tucker, and K. Prentice, Application of advanced very high resolution radiometer vegetation index to study atmosphere-biosphere exchange of CO_2, *Journal of Geophysical Research*, *92*(D3), 2999–3015, 1987.

Fung, I., S. Doney, K. Lindsay, and J. John, Evolution of carbon sinks in a changing climate, *Proceedings of the National Academy of Sciences of the United States of America*, *102*, 11,201–11,206, doi:DOI10.1073/pnas.0504949102, 2005.

Fung, I., et al., Carbon 13 exchanges between the atmosphere and biosphere, *Global Biogeochemical Cycles*, *11*, 507–533, 1997.

Gates, L., AMIP: The Atmospheric Model Intercomparison Project, *Bulletin of the American Meteorological Society*, *73*(12), 1962–1970, 1992.

Goody, R. M., *Principles of atmospheric physics and chemistry*, Oxford University Press, New York, 1995.

Goulden, M., et al., Sensitivity of boreal forest carbon balance to soil thaw, *Science*, *279*(5348), 214, 1998.

Hoerling, M., and A. Kumar, The perfect ocean for drought, *Science*, *299*(5607), 691, 2003.

Hsu, C., and J. Wallace, Global distribution of annual and semiannual cycles in precipitation, *Monthly Weather Review*, *104*, 1093–1101, 1976.

Huybers, P., Early Pleistocene glacial cycles and the integrated summer insolation forcing, *Science*, *313*, 508–511, doi:DOI10.1126/science.1125249, 2006.

Huybers, P., and I. Eisenman, Integrated Summer Insolation Calculations., *Data Contribution Series #2006-079*, IGBP PAGES/World Data Center for Paleoclimatology, NOAA/NCDC Paleoclimatology Program, Boulder CO, USA., 2006.

Huybers, P., and E. Tziperman, Integrated summer insolation forcing and 40,000-year glacial cycles: The perspective from an ice-sheet/energy-balance model, *Paleoceanography*, *23*, doi:10.1029/2007PA001463, 2008.

Huybers, P., and C. Wunsch, Obliquity pacing of the late Pleistocene glacial terminations, *Nature*, *434*, 491–494, doi:10.1038/nature03401, 2005.

Jacoby, G., and R. D'Arrigo, Tree ring width and density evidence of climatic and potential forest change in Alaska, *Global Biogeochemical Cycles*, *9*(2), 227–234, 1995.

Jain, S., U. Lall, and M. Mann, Seasonality and interannual variations of Northern Hemisphere temperature: Equator-to-pole gradient and ocean-land contrast, *Journal of Climate*, *12*(4), 1086–1100, 1999.

Johns, T., R. Carnell, J. Crossley, J. Gregory, J. Mitchell, C. Senior, S. Tett, and R. Wood, The second Hadley Centre coupled ocean-atmosphere GCM: Model description, spinup and validation, *Climate Dynamics*, *13*(2), 103–134, 1997.

Jones, P., T. Osborn, and K. Briffa, Estimating sampling errors in large-scale temperature averages, *Journal of Climate*, *10*, 2548–2568, 1997.

Jones, P. D., M. New, D. E. Parker, S. Martin, and I. G. Rigor, Surface Air Temperature and its Changes Over the Past 150 Years, *Reviews of Geophysics*, *37*(2), 173–199, 1999.

Joos, F., and M. Bruno, Long-term variability of the terrestrial and oceanic carbon sinks and the budgets of the carbon isotopes ^{13}C and ^{14}C, *Global Biogeochemical Cycles*, *12*(2), 277–295, 1998.

Kalnay, E., et al., The NCEP/NCAR 40-year reanalysis project, *Bulletin of the American Meteorological Society*, *77*(3), 437–471, 1996.

Kara, A., P. Rochford, and H. Hurlburt, Mixed layer depth variability over the global ocean, *Journal of Geophysical Research-Oceans*, *108*(C3), doi:10.1029/2000JC000,736, 2003.

Karl, T., P. Jones, R. Knight, O. White, W. Mende, J. Beer, and D. Thomson, Testing for bias in the climate record, *Science*, *271*, 1879–1880, 1996.

Keeling, C., The concentration and isotopic abundances of carbon dioxide in the atmosphere, *Tellus*, *12*(2), 200–203, 1960.

Keeling, C., The concentration and isotopic abundances of carbon dioxide in rural and marine air, *Geochimica Et Cosmochimica Acta*, *24*, 277–298, 1961.

Keeling, C., J. Chin, and T. Whorf, Increased activity of northern vegetation inferred from atmospheric CO_2 measurements, *Nature*, *382*, 146–149, 1996.

Keeling, C., S. Piper, R. Bacastow, M. Wahlen, T. Whorf, M. Heimann, and H. Meijer, Exchanges of atmospheric CO_2 and $^{13}CO_2$ with the terrestrial biosphere and oceans from 1978 to 2000. I. Global aspects, *SIO Reference Series No. 01-06*, Scripps Institution of Oceanography, San Diego, 2001.

Keeling, R., and S. Shertz, Seasonal and interannual variations in atmospheric oxygen and implications for the global carbon cycle, *Nature*, *358*(6389), 723–727, 1992.

Kelley, J., John J., An analysis of carbon dioxide in the Arctic atmosphere at Point Barrow, Alaska, 1961 - 1962 - 1963, *Technical Report, Office of Naval Research Contract 477(24) (NR 307-252))*, Department of Atmospheric Sciences, University of Washington., 1964a.

Kelley, J., John J., An analysis of carbon dioxide in the Arctic atmosphere at Barrow, Alaska during 1961 - 1962 - 1963: Report No. 2., *Technical report, Office of Naval Research Contract 477(24) (NR 307-252))*, Department of Atmospheric Sciences, University of Washington., 1964b.

Kendrew, W., *Climate of the Continents*, 5th edition ed., Oxford University Press, 1961.

Larcher, W., *Ökologie der Pflanzen (Translated into English as "Physiological Plant Ecology")*, Verlag Eugen Ulmer, Stuttgart, 1984.

Leith, H., *Primary productivity of the biosphere*, *Ecological Studies*, vol. 14, chap. Primary production of the major vegetation units of the world, pp. 203–215, Springer Verlag, New York and Berlin, 1975.

Levin, I., R. Graul, and N. Trivett, Long-term observations of atmospheric CO_2 and carbon isotopes at continental sites in Germany, *Tellus*, *47*(1/2), 23–34, 1995.

Li, H., A. Robock, and M. Wild, Evaluation of Intergovernmental Panel on Climate Change Fourth Assessment soil moisture simulations for the second half of the twentieth century, *Journal of Geophysical Research-Atmospheres*, *112*(D6), doi:10.1029/2006JD007,455, 2007.

Liepert, B., Observed reductions of surface solar radiation at sites in the United States and worldwide from 1961 to 1990, *Geophysical Research Letters*, *29*(10), doi:10.1029/2002GL014,910, 2002.

Lohmann, U., and J. Feichter, Global indirect aerosol effects: a review, *Atmos. Chem. Phys.*, *5*, 715–737, 2005.

Long, S., E. Ainsworth, A. Rogers, and D. Ort, Rising atmospheric carbon dioxide: Plants FACE the future, *Annual Review of Plant Biology*, *55*, 591–628, doi:10.1146/annurev.arplant.55.031903.141610, 2004.

Lotsch, A., M. Friedl, B. Anderson, and C. Tucker, Response of terrestrial ecosystems to recent Northern Hemispheric drought, *Geophysical Research Letters*, *32*(6), L06,705, 2005.

Mack, M., E. Schuur, M. Bret-Harte, G. Shaver, and F. Chapin, Ecosystem carbon storage in arctic tundra reduced by long-term nutrient fertilization, *Nature*, *431*(7007), 440–443, 2004.

Madden, R., D. Shea, G. Branstator, J. Tribbia, and R. Weber, The effects of imperfect spatial and temporal sampling on estimates of the global mean temperature: experiments with model data, *Journal of Climate*, *6*(6), 1057–1066, 1993.

Maddy, E., C. Barnet, M. Goldberg, C. Sweeney, and X. Liu, CO_2 retrievals from the Atmospheric Infrared Sounder: Methodology and validation, *J. Geophys. Res*, *113*, 2008.

Magnuson, J., et al., Historical trends in lake and river ice cover in the Northern Hemisphere, *Science*, *289*(5485), 1743–1746, 2000.

Manabe, S., R. Stouffer, M. Spellman, and K. Byran, Transient response of a coupled ocean atmosphere model to gradual changes of atmospheric CO_2 1. Annual mean response, *Journal of Climate*, *4*(8), 785–818, 1991.

Manley, G., The mean temperature of central England, 1698-1952, *Quarterly Journal of the Royal Meteorological Society*, *79*(340), 242–261, 1953.

Manley, G., J. Glasspoole, D. Schove, E. Gold, C. Brooks, E. Hawke, and G. Manley, The mean temperature of central England, 1698-1952 - discussion, *Quarterly Journal of the Royal Meteorological Society*, *79*(342), 558–567, 1953.

Mann, M., and J. Park, Greenhouse warming and changes in the seasonal cycle of temperature: Model versus observations, *Geophysical Research Letters*, *23*(10), 1111–1114, 1996.

Meehl, G., C. Covey, B. McAvaney, M. Latif, and R. Stouffer, Overview of the Coupled Model Intercomparison Project, *Bulletin of the American Meteorological Society*, *86*(1), 89–93, doi:10.1175/BAMS-86-1-89, 2005.

Meehl, G., et al., *Climate Change 2007: The Physical Science Basis. Contribution of Working Group I to the Fourth Assessment Report of the Intergovernmental Panel on Climate Change*, chap. 10. Global Climate Projections, pp. 747–845, Cambridge University Press, Cambridge, United Kingdom and New York, NY, USA, 2007a.

Meehl, G. A., C. Covey, T. Delworth, M. Latif, B. McAvaney, J. F. B. Mitchell, R. J. Stouffer, and K. E. Taylor, The WCRP CMIP3 multimodel dataset - A new era in climate change research, *Bulletin of the American Meteorological Society*, *88*(9), 1383–1394, doi: DOI10.1175/BAMS-88-9-1383, 2007b.

Miller, A., S. Zhou, and S. Yang, Relationship of the Arctic and Antarctic Oscillations to the outgoing longwave radiation, *Journal of Climate*, *16*(10), 1583–1592, 2003.

Mo, C., Relationships between low-frequency variability in the Southern Hemisphere and sea surface temperature anomalies, *Journal of Climate*, *13*(20), 3599–3610, 2000.

Myneni, R., C. Keeling, C. Tucker, G. Asrar, and R. Nemani, Increased plant growth in the northern high latitudes from 1981 to 1991, *Nature*, *386*(6626), 698–702, 1997.

Nemani, R., C. Keeling, H. Hashimoto, W. Jolly, S. Piper, C. Tucker, R. Myneni, and S. Running, Climate-driven increases in global terrestrial net primary production from 1982 to 1999, *Science*, *300*(5625), 1560–1563, 2003.

New, M., M. Hulme, and P. Jones, Representing twentieth-century space-time climate variability. Part I: Development of a 1961-90 mean monthly terrestrial climatology, *Journal of Climate*, *12*, 829–856, 1999.

Oechel, W., S. Hastings, G. Vourlitis, M. Jenkins, G. Riechers, and N. Grulke, Recent change of Arctic tundra ecosystems from a net carbon dioxide sink to a source, *Nature*, *361*, 520–523, 1993.

Oechel, W., G. Vourlitis, S. Hastings, R. Zulueta, L. Hinzman, and D. Kane, Acclimation of ecosystem CO_2 exchange in the Alaskan Arctic in response to decadal climate warming, *Nature*, *406*(6799), 978–981, 2000.

Oglesby, R., and B. Saltzman, Equilibrium climate statistics of a general circulation model as a function of atmospheric carbon dioxide. Part 1: Geographic distributions of primary variabiles, *Journal of Climate*, *5*(1), 66–92, 1992.

Pales, J., and C. Keeling, The concentration of atmospheric carbon dioxide in Hawaii, *J. Geophys. Res*, *70*(24), 6053–6076, 1965.

Parker, D., T. Legg, and C. Folland, A new daily Central England temperature series, 1772-1991, *International Journal of Climatology*, *12*(4), 317–342, 1992.

Parker, D., P. Jones, C. Folland, and A. Bevan, Interdecadal changes of surface temperature since the late nineteenth century, *Journal of Geophysical Research-Atmospheres*, *99*(D7), 14,373–14,399, 1994.

Pearman, G., and D. Beardsmore, Atmospheric carbon dioxide measurements in the Australian region: 10 years of aircraft data, *Tellus 36B, 1*, *24*, 1984.

Pearman, G., and P. Hyson, Activities of the global biosphere as reflected in atmospheric CO_2 records, *Journal of Geophysical Research-Oceans*, *85*(C8), 1980.

Pearman, G., and P. Hyson, The annual variation of atmospheric CO_2 concentration observed in the Northern Hemisphere, *Journal of Geophysical Research*, *86*(C10), 1981.

Pearman, G., and P. Hyson, Global transport and inter-reservoir exchange of carbon dioxide with particular reference to stable isotopic distributions, *Journal of Atmospheric Chemistry*, *4*(1), 81–124, 1986.

Peñuelas, J., and I. Filella, Responses to a warming world, *Science*, *294*(5543), 793–795, 2001.

Piao, S., et al., Net carbon dioxide losses of northern ecosystems in response to autumn warming, *Nature*, *451*, 49–53, 2008.

Prentice, I., et al., *Climate Change 2001: The Scientific Basis. Contribution of Working Group I to the Third Assessment Report of the Intergovernmental Panel on Climate Change*, chap. 3. The Carbon Cycle and Atmospheric Carbon Dioxide, 183-237 ed., Cambridge University Press, Cambridge, United Kingdom and New York, NY, USA., 2001.

Prescott, J., and J. Collins, The lag of temperature behind solar radiation, *Quarterly Journal of the Royal Meteorological Society*, *77*, 121–126, 1951.

Quadrelli, R., and J. Wallace, A simplified linear framework for interpreting patterns of Northern Hemisphere wintertime climate variability, *Journal of Climate*, *17*, 3728–3744, 2004.

Randall, D., et al., *Climate Change 2007: The Physical Science Basis. Contribution of Working Group I to the Fourth Assessment Report of the Intergovernmental Panel on Climate Change*, chap. 8. Climate Models and Their Evaluation, pp. 589–662, Cambridge University Press, Cambridge, United Kingdom and New York, NY, USA, 2007.

Randerson, J., M. Thompson, T. Conway, I. Fung, and C. Field, The contribution of terrestrial sources and sinks to trends in the seasonal cycle of atmospheric carbon dioxide, *Global Biogeochemical Cycles*, *11*(4), 1997.

Randerson, J., C. Field, I. Fung, and P. Tans, Increases in early season ecosystem uptake explain recent changes in the seasonal cycle of atmospheric CO_2 at high northern latitudes, *Geophysical Research Letters*, *26*(17), 1999.

Rayner, N., D. Parker, E. Horton, C. Folland, L. Alexander, D. Rowell, E. Kent, and A. Kaplan, Global analyses of sea surface temperature, sea ice, and night marine air temperature since the late nineteenth century, *Journal of Geophysical Research-Atmospheres*, *108*, doi: ARTN4407, 2003.

Rayner, N., P. Brohan, D. Parker, C. Folland, J. Kennedy, M. Vanicek, T. Anselland, and S. Tett, Improved analyses of changes and uncertainties in sea surface temperature measured in situ since the mid-nineteenth century: The HadSST2 dataset, *Journal of Climate*, *19*, 446–469, 2006.

Reay, D. S., F. Dentener, P. Smith, J. Grace, and R. A. Feely, Global nitrogen deposition and carbon sinks, *Nature Geosci*, *1*(7), 430–437, 2008.

Robock, A., K. Vinnikov, G. Srinivasan, J. Entin, S. Hollinger, N. Speranskaya, S. Liu, and A. Namkhai, The Global Soil Moisture Data Bank, *Bulletin of the American Meteorological Society*, *81*(6), 1281–1299, 2000.

Saito, K., and J. Cohen, The potential role of snow cover in forcing interannual variability of the major Northern Hemisphere mode, *Geophysical Research Letters*, *30*(6), doi:10.1029/2002GL016,341, doi:ARTN1302, 2003.

Schreiber, T., and A. Schmitz, Surrogate time series, *Physica D*, *142*, 346–382, 2000.

Schwartz, M., R. Ahas, and A. Aasa, Onset of spring starting earlier across the Northern Hemisphere, *Global Change Biology*, *12*(2), 343–351, doi:10.1111/j.1365-2486.2005.01097.x, 2006.

Shell, K., and R. Somerville, A generalized energy balance climate model with parameterized dynamics and diabatic heating, *Journal of Climate*, *18*(11), 1753–1772, 2005.

Sparks, T., and A. Menzel, Observed changes in seasons: An overview, *International Journal of Climatology*, *22*(14), 1715–1725, doi:10.1002/joc.821, 2002.

Stanhill, G., and S. Cohen, Global dimming: A review of the evidence for a widespread and significant reduction in global radiation with discussion of its probable causes and possible agricultural consequences, *Agricultural and Forest Meteorology*, *107*(4), 255–278, 2001.

Stine, A., P. Huybers, and I. Fung, Changes in the phase of the annual cycle of surface temperature, *Nature*, *457*(7228), 435–440, 2009.

Stuiver, M., Atmospheric carbon dioxide and carbon reservoir changes, *Science*, *199*(4326), 253, 1978.

Tans, P., K. Thoning, W. Elliott, and T. Conway, Background atmospheric CO_2 patterns from weekly flask samples at Barrow, Alaska: optimal signal recovery and error estimates, *NOAA Tech. Memo ERL ARL-173*, NOAA Environ. Res. Lab., 1989.

Thompson, D., and J. Wallace, The Arctic Oscillation signature in the wintertime geopotential height and temperature fields, *Geophysical Research Letters*, *25*(9), 1297–1300, 1998.

Thompson, D., and J. Wallace, Annular modes in the extratropical circulation. Part I: Month-to-month variability, *Journal of Climate*, *13*(5), 1000–1016, 2000.

Thompson, R., Complex demodulation and the estimation of the changing continentality of Europe's climate, *International Journal of Climatology*, *15*, 175–185, 1994.

Thomson, D., The seasons, global temperature, and precession, *Science*, *268*, 59–68, 1995.

Trenberth, K., Signal versus noise in the Southern Oscillation, *Monthly Weather Review*, *112*(2), 326–332, 1984.

Trenberth, K., et al., *Climate Change 2007: The Physical Science Basis. Contribution of Working Group I to the Fourth Assessment Report of the Intergovernmental Panel on Climate Change*, chap. 3. Observations: Surface and Atmospheric Climate Change, pp. 235–336, Cambridge University Press, Cambridge, United Kingdom and New York, NY, USA, 2007.

van Loon, H., *Meteorology of the Southern Hemisphere*, chap. Temperature in the Southern Hemisphere, pp. 25–58, no. 35 in Meteorlogical Monographs, American Meteorological Society, Boston, Mass., 1972.

Vinnikov, K., and I. Yeserkepova, Soil soisture: Emperical data and model results, *Journal of Climate*, *4*(1), 66–79, 1991.

Wallace, C., and T. Osborn, Recent and future modulation of the annual cycle, *Climate Research*, *22*, 1–11, 2002.

Wallace, J., North Atlantic Oscillation/Annular Mode: Two paradigms - one phenomenon, *Quarterly Journal of the Royal Meteorological Society*, *126*(564), 791–805, 2000.

Wallace, J., and D. Gutzler, Teleconnections in the geopotential height field during the Northern Hemisphere winter, *Monthly Weather Review*, *109*(4), 784–812, 1981.

Wallace, J., Y. Zhang, and J. Renwick, Dynamic contribution to hemispheric mean temperature trends, *Science*, *270*(5237), 780–783, 1995.

Wallace, J., Y. Zhang, and L. Bajuk, Interpretation of interdecadal trends in Northern Hemisphere surface air temperature, *Journal of Climate*, *9*(2), 249–259, 1996.

Ward, R., The classification of climates: I, *Bulletin of the American Geographical Society*, *38*(7), 401–412, 1906.

WDCGG, Revision of the WDCGG Data Submission and Dissemination Guide, *WMO/TD-No.1507*, World Meteorological Organization, 2009.

Weltzin, J., et al., Assessing the response of terrestrial ecosystems to potential changes in precipitation, *Bioscience*, *53*(10), 941–952, 2003.

White, G., and J. Wallace, Global distribution of annual and semiannual cycles in surface temperature, *Monthly Weather Review*, *106*, 901–906, 1978.

Wigley, T., and P. Jones, Detecting CO_2-induced climate change, *Nature*, *292*(5820), 205–208, 1981.

Wild, M., et al., From dimming to brightening: Decadal changes in solar radiation at Earth's surface, *Science*, *308*(5723), 847–850, doi:10.1126/science.1103215, 2005.

Wunsch, C., The interpretation of short climate records, with comments on the North Atlantic and Southern Oscillations, *Bulletin of the American Meteorological Society*, *80*, 245–255, 1999.

Yang, Z., G. Toon, J. Margolis, and P. Wennberg, Atmospheric CO_2 retrieved from ground-based near IR solar spectra, *Geophysical Research Letters*, *29*(9), 53–1, 2002.

Yeh, T.-C., R. T. Wetherald, and S. Manabe, The effect of soil moisture on the short-term climate and hydrology change—A numerical experiment, *Monthly Weather Review*, *112*(3), 474–490, 1984.

Zhang, X., F. Zwiers, G. Hegerl, F. Lambert, N. Gillett, S. Solomon, P. Stott, and T. Nozawa, Detection of human influence on twentieth-century precipitation trends, *Nature*, *448*(7152), 461, 2007.

Zhang, Y., J. Wallace, and D. Battisti, ENSO-like Interdecadal Variability: 1900–93, *Journal of Climate*, *10*(5), 1004–1020, 1997.

Zhou, S., A. Miller, J. Wang, and J. Angell, Trends of NAO and AO and their associations with stratospheric processes, *Geophysical Research Letters*, *28*(21), 2001.